NUREG/CR-4667, Vol. 29
ANL-00/23

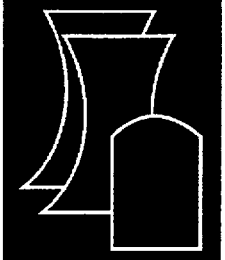

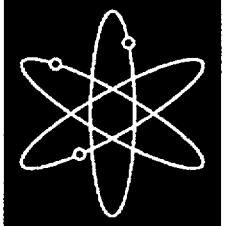

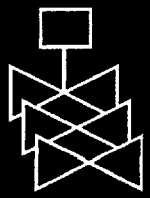

Environmentally Assisted Cracking in Light Water Reactors

Semiannual Report
July 1999 - December 1999

Argonne National Laboratory

U.S. Nuclear Regulatory Commission
Office of Nuclear Regulatory Research
Washington, DC 20555-0001

AVAILABILITY OF REFERENCE MATERIALS IN NRC PUBLICATIONS

NRC Reference Material

As of November 1999, you may electronically access NUREG-series publications and other NRC records at NRC's Public Electronic Reading Room at www.nrc.gov/NRC/ADAMS/index.html.
Publicly released records include, to name a few, NUREG-series publications; *Federal Register* notices; applicant, licensee, and vendor documents and correspondence; NRC correspondence and internal memoranda; bulletins and information notices; inspection and investigative reports; licensee event reports; and Commission papers and their attachments.

NRC publications in the NUREG series, NRC regulations, and *Title 10, Energy*, in the Code of *Federal Regulations* may also be purchased from one of these two sources.

1. The Superintendent of Documents
   U.S. Government Printing Office
   P. O. Box 37082
   Washington, DC 20402–9328
   www.access.gpo.gov/su_docs
   202–512–1800
2. The National Technical Information Service
   Springfield, VA 22161–0002
   www.ntis.gov
   1–800–533–6847 or, locally, 703–805–6000

A single copy of each NRC draft report for comment is available free, to the extent of supply, upon written request as follows:

Address: Office of the Chief Information Officer,
Reproduction and Distribution
Services Section
U.S. Nuclear Regulatory Commission
Washington, DC 20555-0001
E-mail: DISTRIBUTION@nrc.gov
Facsimile: 301–415–2289

Some publications in the NUREG series that are posted at NRC's Web site address www.nrc.gov/NRC/NUREGS/indexnum.html are updated periodically and may differ from the last printed version. Although references to material found on a Web site bear the date the material was accessed, the material available on the date cited may subsequently be removed from the site.

Non-NRC Reference Material

Documents available from public and special technical libraries include all open literature items, such as books, journal articles, and transactions, *Federal Register* notices, Federal and State legislation, and congressional reports. Such documents as theses, dissertations, foreign reports and translations, and non-NRC conference proceedings may be purchased from their sponsoring organization.

Copies of industry codes and standards used in a substantive manner in the NRC regulatory process are maintained at—

The NRC Technical Library
Two White Flint North
11545 Rockville Pike
Rockville, MD 20852–2738

These standards are available in the library for reference use by the public. Codes and standards are usually copyrighted and may be purchased from the originating organization or, if they are American National Standards, from—

American National Standards Institute
11 West 42nd Street
New York, NY 10036–8002
www.ansi.org
212–642–4900

The NUREG series comprises (1) technical and administrative reports and books prepared by the staff (NUREG–XXXX) or agency contractors (NUREG/CR–XXXX), (2) proceedings of conferences (NUREG/CP–XXXX), (3) reports resulting from international agreements (NUREG/IA–XXXX), (4) brochures (NUREG/BR–XXXX), and (5) compilations of legal decisions and orders of the Commission and Atomic and Safety Licensing Boards and of Directors' decisions under Section 2.206 of NRC's regulations (NUREG–0750).

NUREG/CR-4667, Vol. 29

Environmentally Assisted Cracking in Light Water Reactors

Semiannual Report
July 1999 - December 1999

Manuscript Completed: September 2000
Date Published: November 2000

Prepared by
O. K. Chopra, H. M. Chung, E. E. Gruber
W. E. Ruther, W. J. Shack, J. L. Smith
W. K. Soppert, R.V. Strain

Argonne National Laboratory
9700 South Cass Avenue
Argonne, IL 60439

M. B. McNeil, NRC Project Manager

Prepared for
Division of Engineering Technology
Office of Nuclear Regulatory Research
U.S. Nuclear Regulatory Commission
Washington, DC 20555-0001
NRC Job Code W6610

Previous Documents in Series

Environmentally Assisted Cracking in Light Water Reactors Semiannual Report
April—September 1985, NUREG/CR–4667 Vol. I, ANL–86–31 (June 1986).
October 1985—March 1986, NUREG/CR–4667 Vol. II, ANL–86–37 (September 1987).
April—September 1986, NUREG/CR–4667 Vol. III, ANL–87–37 (September 1987).
October 1986—March 1987, NUREG/CR–4667 Vol. IV, ANL–87–41 (December 1987).
April—September 1987, NUREG/CR–4667 Vol. V, ANL–88–32 (June 1988).
October 1987—March 1988, NUREG/CR–4667 Vol. 6, ANL–89/10 (August 1989).
April—September 1988, NUREG/CR–4667 Vol. 7, ANL–89/40 (March 1990).
October 1988—March 1989, NUREG/CR–4667 Vol. 8, ANL–90/4 (June 1990).
April—September 1989, NUREG/CR–4667 Vol. 9, ANL–90/48 (March 1991).
October 1989—March 1990, NUREG/CR–4667 Vol. 10, ANL–91/5 (March 1991).
April—September 1990, NUREG/CR–4667 Vol. 11, ANL–91/9 (May 1991).
October 1990—March 1991, NUREG/CR–4667 Vol. 12, ANL–91/24 (August 1991).
April—September 1991, NUREG/CR–4667 Vol. 13, ANL–92/6 (March 1992).
October 1991—March 1992, NUREG/CR–4667 Vol. 14, ANL–92/30 (August 1992).
April—September 1992, NUREG/CR–4667 Vol. 15, ANL–93/2 (June 1993).
October 1992—March 1993, NUREG/CR–4667 Vol. 16, ANL–93/27 (September 1993).
April—September 1993, NUREG/CR–4667 Vol. 17, ANL–94/26 (June 1994).
October 1993—March 1994, NUREG/CR–4667 Vol. 18, ANL–95/2 (March 1995).
April—September 1994, NUREG/CR–4667 Vol. 19, ANL–95/25 (September 1995).
October 1994—March 1995, NUREG/CR–4667 Vol. 20, ANL–95/41 (January 1996).
April—December 1995, NUREG/CR–4667 Vol. 21, ANL–96/1 (July 1996).
January 1996—June 1996, NUREG/CR–4667 Vol. 22, ANL–97/9 (June 1997).
July 1996—December 1996, NUREG/CR–4667 Vol. 23, ANL–97/10 (October 1997).
January 1997—June 1997, NUREG/CR–4667 Vol. 24, ANL–98/6 (April 1998).
July 1997—December 1997, NUREG/CR–4667 Vol. 25, ANL–98/18 (September 1998).
January 1998—June 1998, NUREG/CR–4667 Vol. 26, ANL–98/30 (December 1998).
July 1998—December 1998, NUREG/CR–4667 Vol. 27, ANL–99/11 (October 1999).
January 1999—June 1999, NUREG/CR–4667 Vol. 28, ANL–00/7 (July 2000).

Environmentally Assisted Cracking in Light Water Reactors Semiannual Report July 1999–December 1999

by

O. K. Chopra, H. M. Chung, E. E. Gruber, W. E. Ruther,
W. J. Shack, J. L. Smith, W. K. Soppet, and R. V. Strain

Abstract

This report summarizes work performed by Argonne National Laboratory on fatigue and environmentally assisted cracking (EAC) in light water reactors (LWRs) from July 1999 to December 1999. Topics that have been investigated include (a) environmental effects on fatigue S–N behavior of primary pressure boundary materials, (b) irradiation–assisted stress corrosion cracking (IASCC) of austenitic stainless steels (SSs), (c) EAC of Alloys 600 and 690, and (d) assessment of industry crack-growth models. The fatigue strain-vs.–life data that are available on the effects of various material, loading, and environmental parameters on the fatigue lives of carbon and low–alloy steels and austenitic SSs are summarized. Effects of reactor coolant environment on the mechanism of fatigue crack initiation are discussed. Two methods for incorporating the effects of LWR coolant environments into the ASME Code fatigue evaluations are presented. Slow-strain-rate tensile tests and posttest fractographic analyses were conducted on several model SS alloys irradiated to $\approx 0.9 \times 10^{21}$ n·cm^{-2} (E > 1 MeV) in He at 289°C in the Halden reactor. The results have been used to determine the influence of alloying and impurity elements on the susceptibility of these steels to IASCC. Fracture toughness J–R curve tests were also conducted on two heats of Type 304 SS that were irradiated to ≈ 0.3 and 0.9×10^{21} n·cm^{-2} in the Halden reactor. Crack–growth–rate tests have been conducted on compact–tension specimens of Alloy 690 under cyclic loading to evaluate the enhancement of crack growth rates of these alloys in LWR environments. The existing fatigue crack growth data on Alloys 600 and 690 have been analyzed to establish the effects of temperature, load ratio, frequency, and stress intensity range ΔK on crack growth rates in air. Predictions of the PLEDGE code for environmentally assisted cracking in stainless steels have been compared with experimental data collected by the BWRVIP, developed at ANL, provided by P. L. Andresen of GE, used to develop the original USNRC disposition curve, and gathered from other sources in the literature. The results indicate that PLEDGE code provides conservative predictions of crack growth rates in unirradiated sensitized materials provided that an appropriate value is chosen for the parameter used to characterize the sensitization denoted by EPR.

NUREG/CR-4667, Volume 29, has been reproduced from the best available copy.

Contents

Executive Summary xiii

Acknowledgments xvi

1 Introduction 1

2 Environmental Effects on Fatigue Strain-versus-Life Behavior of Primary Pressure Boundary Materials 3

2.1 Introduction 3

2.2 Mechanism of Fatigue Crack Initiation 5

2.3 Fatigue S–N Data in LWR Environments 7

2.3.1 Carbon and Low-Alloy Steels 7

2.3.2 Austenitic Stainless Steels 8

2.4 Incorporating Environmental Effects into ASME Fatigue Evaluations 10

2.4.1 Design Fatigue Curves 10

2.4.2 Fatigue Life Correction Factor 14

3 Irradiation-Assisted Stress Corrosion Cracking of Austenitic SS 17

3.1 Introduction 17

3.2 Slow-Strain-Rate-Tensile Test of Model Austenitic Stainless Steels Irradiated in the Halden Reactor 18

3.2.1 Test Matrix, Specimen Fabrication, and Irradiation 18

3.2.2 Slow-Strain-Rate Tensile Test and Fractographic Analysis of Medium-Fluence Specimens 20

3.3 Fracture Toughness J-R Test of Austenitic Stainless Steels Irradiated in the Halden Reactor 30

3.3.1 Introduction 30

3.3.2 Experimental 30

3.3.3 Results 34

4 Environmentally Assisted Cracking of Alloys 600 and 690 in Simulated LWR Water 39

4.1 Fatigue Crack Growth Rates in Air 39

4.1.1 Alloy 600 39

4.1.2 Alloy 690 44

5 Assessment of Industry Crack-Growth Models 47

5.1 Introduction 47

5.2 Overall Comparisons with Experimental Data 49

5.3 Comparison of Specific Dependencies on EPR, Conductivity, and ECP 54

6 Summary of Results 65

6.1 Environmental Effects on Fatigue S–N Behavior of Primary Pressure Boundary Materials 65

6.2 Irradiation–Assisted Stress Corrosion Cracking of Austenitic Stainless Steels 65

6.3 Fracture Toughness J–R Test of Austenitic Stainless Steels Irradiated in the Halden Reactor 66

6.4 Environmentally Assisted Cracking of Low–Carbon Alloys 600 and 690 in Simulated LWR Water 66

6.5 Assessment of Industry Crack-Growth Models 67

References 69

Figures

1. S–N data for carbon steels and austenitic stainless steels in water 4
2. Schematic illustration of growth of short cracks in smooth specimens as a function of fatigue life fraction and crack velocity as a function of crack length 6
3. Dependence of fatigue lives of carbon steels and low–alloy steels on strain rate 8
4. Effects of conductivity of water and soak period on fatigue lives of Type 304 SS in high–DO water 9
5. Design fatigue curve developed from statistical model for carbon steels, low–alloy steels and austenitic stainless steels in air at room temperature 12
6. Design fatigue curves developed from statistical model for carbon and low–alloy steels under service conditions where one or more critical threshold values are not satisfied 13
7. Design fatigue curves developed from statistical model for carbon and low–alloy steels under service conditions where one or more critical threshold values are not satisfied 14
8. Design fatigue curves developed from statistical models for Types 304 and 316 SS in water with <0.05 and ≥0.05 ppm DO 15
9. Comparison of experimental data adjusted for environmental effects with best–fit fatigue S–N curve in room–temperature air 16
10. Effects of fluence and test environment on load elongation behavior of Type 304 SS commercial heat C19 24
11. Effects of fluence on yield strength measured in 289°C water containing ≈8 ppm DO. 25
12. Effects of fluence on maximum strength measured in 289°C water containing ≈8 ppm DO. 25
13. Effects of fluence on uniform elongation measured in 289°C water containing ≈8 ppm DO. 26
14. Effects of fluence on total elongation measured in 289°C water containing ≈8 ppm DO. 26
15. Effects of fluence on percent TGSCC measured in 289°C water containing ≈8 ppm DO. 27
16. Effects of fluence on percent IGSCC measured in 289°C water containing ≈8 ppm DO. 27
17. Effects of fluence on percent TGSCC + IGSCC measured in 289°C water containing ≈8 ppm DO 28

18. Effect of Si concentration on yield strength of Types 304 and 304L alloys measured in 289°C water before and after irradiation. 29

19. Effect of Si on susceptibility to IGSCC of laboratory alloys of Types 304 and 304L SS measured after irradiation to ≈0.9 x 10^{21} n·cm^{-2} 29

20. Fracture toughness J_{IC} as a function of neutron exposure for austenitic Types 304 and 316 SS 31

21. Configuration of compact-tension specimen for this study 31

22. Examples of load-vs.-loadline displacement curves for irradiated specimens of Heats C19 and L20 of Type 304 SS tested at 288°C 32

23. Fracture toughness J–R curves determined by DC potential drop and unloading compliance methods for Heat L20 irradiated to 0.3 x 10^{21} n·cm^{-2} (0.45 dpa) at 288°C 33

24. Fracture toughness J–R curves determined by DC potential drop and unloading compliance methods for Heat C19 irradiated to 0.3 x 10^{21} n·cm^{-2} (0.45 dpa) at 288°C 33

25. Fracture toughness J–R curve obtained by DC potential method for nonirradiated specimens L2–C and L2–E of Heat L2 of Type 304 SS at 288°C 34

26. Fracture toughness J–R curve obtained by DC potential method for nonirradiated specimen of Heat L20 of Type 304 SS at 288°C 34

27. Fracture toughness J–R curve obtained by DC potential method for nonirradiated specimen of Heat C16 of Type 304 SS at 288°C 35

28. Fracture toughness J–R curve obtained by DC potential method for nonirradiated specimen of Heat C19 of Type 304 SS at 288°C 35

29. Fracture toughness J–R curves for Type 304 stainless steels at 288°C 35

30. Fracture toughness J–R curve at 288°C for Heat L2 irradiated to 0.9 x 10^{21} n·cm^{-2} (E > 1 Me) (1.35 dpa) at 288°C 36

31. Fracture toughness J–R curves at 288°C for Heat L20 irradiated to 0.3 and 0.9 x 10^{21} n·cm^{-2} (E > 1 Me) (0.45 and 1.35 dpa) at 288°C 36

32. Fracture toughness J–R curve at 288°C for Heat C16 irradiated to 0.9 x 10^{21} n·cm^{-2} (E > 1 Me) (0.45 dpa) at 288°C 36

33. Fracture toughness J–R curve at 288°C for Heat C19 irradiated to 0.3 and 0.9 x 10^{21} n·cm^{-2} (E > 1 Me) (0.45 and 1.35 dpa) at 288°C 37

34. Photomicrographs of fracture surfaces of nonirradiated specimens of Heats L2, L20, and C19 tested at 288°C, and MnS inclusions in Heat L2 38

35. Fracture toughness J_{IC} as a function of neutron exposure for austenitic Types 304 and 316 SS 38

36. Effect of temperature on fatigue crack growth rate of Alloy 600 in air 41

37. Effect of rise time on fatigue crack growth rate of Alloy 600 in air 41

38. Variation of constant C for Alloy 600 with temperature 42

39. Residual error for CGRs of Alloy 600 in air as a function of load ratio, rise time, stress intensity range ΔK, K_{max}, temperature, and crack growth rate 43

40. Predicted vs. experimental values of fatigue crack growth rate of Alloy 600 in air at room temperature and temperatures between 35 and 427°C 44

41. Variation of constant C for Alloy 690 with temperature 45

42. Predicted vs. experimental values of fatigue crack growth rate of Alloy 690 in air at temperatures between 35 and 380°C 45

43. Comparison of PLEDGE model predictions with Andresen data set; Comparison of PLEDGE model predictions with ANL IGSCC data set; Comparison of PLEDGE model predictions with BWRVIP data set 51

44. Comparison of PLEDGE model predictions with ANL TG data set 51

45. Comparison of PLEDGE model predictions with ANL high–DO data, data from Kawakubo et al. and data used to develop NRC Disposition curve; Comparison of BWRVIP 95 model predictions modified to account for cyclic loading with same data 52

46. Comparison of PLEDGE, BWRVIP, and modified PLEDGE model predictions with cyclic CGR data from literature; Data for sensitized SS in 0.2 ppm DO; Data for nonsensitized SS in 0.2 ppm DO; Data for sensitized SS in 8 ppm DO 52

47. Comparison of PLEDGE model predictions with screened BWRVIP data set; Comparison of PLEDGE model predictions with ANL IGSCC data set with no adjustment to reported EPR values 54

48. Variation of errors in PLEDGE predictions with conductivity for Andresen, ANL IGSCC, BWRVIP, and ANL TGSCC data sets 55

49. Variation of errors in PLEDGE predictions with ECP for Andresen, ANL IGSCC, BWRVIP, and ANL TGSCC data sets 57

50. Variation of errors in PLEDGE predictions with EPR for ANL IGSCC and BWRVI data sets 58

51. Variation of errors in PLEDGE predictions with EPR for the Andresen, ANL IGSCC, BWRVIP, and ANL TGSCC data sets 59

52. Effect of sensitization on CGR observed in cyclic load tests of Kawakubo et al.; PLEDGE prediction of change in CGR due to change in sensitization 60

53. Effect of sensitization on CGR observed in cyclic load tests used for NRC disposition curve; PLEDGE prediction of change in CGR due to change in sensitization. 61

54. Predicted effect of variation in conductivity on CGR for R=0.95 loading 62

55. Predicted effect of variation in ECP on CGR for R=0.95 loading 62

56. Predicted effect of variation in ECP on CGR for R=1 loading. 62

Tables

1. Fatigue test results for Type 304 austenitic SS at 288°C 9

2. Elemental composition of 27 commercial and laboratory model austenitic stainless steel alloys irradiated in the Halden Reactor 19

3. Summary of discharge fluence of model austenitic stainless steel alloys irradiated in Halden Reactor 20

4. Results of SSRT tests and SEM fractography for nonirradiated control specimens of model austenitic stainless steel alloys 21

5. Compositional characteristics of nonirradiated control specimens of model austenitic stainless steel alloys correlated with results of SSRT tests and SEM fractography 21

6. Results of SSRT test and SEM fractography for model austenitic stainless steels irradiated in He at 289°C to fluence of $\approx 0.3 \times 10^{21}$ n·cm^{-2} 22

7. Compositional characteristics of model austenitic stainless steels irradiated to fluence of $\approx 0.3 \times 10^{21}$ n·cm^{-2} correlated with results of SSRT tests and SEM fractography 22

8. Results of SSRT tests and SEM fractography for model austenitic stainless steels irradiated in He at 289°C to fluence of $\approx 0.9 \times 10^{21}$ n·cm^{-2} 23

9. Compositional characteristics of model austenitic stainless steels irradiated to fluence of $\approx 0.9 \times 10^{21}$ n·cm^{-2} correlated with results of SSRT tests and SEM fractography 24

10. Composition of model Type 304 SS alloys irradiated in the Halden reactor 31

11. Composition of Alloy 600 heats used for fatigue crack growth studies in air 40

12. Heat treatment conditions and tensile properties of Alloy 600 heats used for fatigue crack growth studies in air 40

13. Composition of Alloy 690 heats used for fatigue crack growth studies in air 44

14. Heat treatment conditions and tensile properties of Alloy 690 heats used for fatigue crack growth studies in air 44

15. Mean error difference between PLEDGE predictions of CGR and experimental measurements for the four data sets 52

16. Mean error difference between PLEDGE predictions of CGR and experimental measurements for screened BWRVIP data set and ANL IGSCC data set using reported EPR values 53

17. Effect of conductivity on mean error difference between PLEDGE predictions of CGR and experimental measurements for the four data sets 55

18. Effect of EPR on mean difference between PLEDGE predictions of CGR and experimental measurements for screened BWRVIP data sets..... 60

19. Effect of ECP on mean difference between PLEDGE predictions of CGR and experimental measurements for low-conductivity data in Andresen and ANL TG data sets..... 60

Executive Summary

The ASME Boiler and Pressure Vessel Code provides rules for the construction of nuclear power plant components. Figure I-9.0 of Appendix I to Section III of the Code specifies fatigue design curves for structural materials. Although effects of light water reactor (LWR) coolant environments are not explicitly addressed by the design curves, test data suggest that the Code fatigue curves may not be adequate in coolant environments. The two methods have been proposed for incorporating the effects of LWR coolant environments into the ASME Code fatigue evaluations: (a) develop new design fatigue curves for LWR applications, and (b) use a fatigue life correction factor to account for environmental effects. Both methods of evaluating fatigue lives are based on the statistical models for estimating fatigue lives of carbon and low-alloy steels and austenitic SSs in LWR environments. Although estimates of fatigue lives based on the two methods may differ because of differences between the ASME mean curves used to develop the current design curves and the best-fit curves to the existing data used to develop the environmentally adjusted curves, either of these methods provides an acceptable approach to account for environmental effects. The mechanisms of fatigue crack initiation in carbon and low-alloy steels and austenitic SSs in LWR environments are discussed.

Hot-cell tests were conducted to determine the susceptibility to irradiation-assisted stress corrosion cracking of model austenitic stainless steels that were irradiated in the Halden Boiling Heavy Water Reactor in simulation of irradiation-induced degradation of boiling water reactor (BWR) core internal components. Slow-strain-rate tensile tests in simulated BWR-like water were conducted on 23 model austenitic stainless steel alloys that were irradiated at 288°C in helium in the Halden reactor to a fluence of $\approx 0.9 \times 10^{21}$ n·cm^{-2} (E > 1 MeV). Fractographic analysis by scanning electron microscopy was conducted to determine the susceptibility to irradiation-assisted stress corrosion cracking as manifested by the degree of intergranular and transgranular fracture surface morphology. These results were compared with similar test results obtained for 16 alloys that were irradiated to a fluence of $\approx 0.3 \times 10^{21}$ n·cm^{-2} (E > 1 MeV).

At $\approx 0.3 \times 10^{21}$ n·cm^{-2} (E > 1 MeV), many alloys were susceptible to transgranular stress corrosion cracking, but only one alloy of Type 316L stainless steel that contains a very low concentration of Si (0.024 wt.% Si) was susceptible to intergranular stress corrosion cracking. Alloy-to-alloy variations in susceptibility to transgranular stress corrosion cracking were significant at $\approx 0.3 \times 10^{21}$ n·cm^{-2}. As fluence was increased from $\approx 0.3 \times 10^{21}$ n·cm^{-2} to $\approx 0.9 \times 10^{21}$ n·cm^{-2}, intergranular fracture surfaces emerged in many alloys, usually in the middle of and surrounded by transgranular fracture surfaces. This indicates that for many alloys, high susceptibility to transgranular stress corrosion cracking is a precursor to susceptibility to intergranular stress corrosion cracking (IGSCC) at a higher fluence. Alloy-to-alloy variations in susceptibility to transgranular and intergranular stress corrosion cracking were significant at $\approx 0.9 \times 10^{21}$ n·cm^{-2}. Susceptibility to transgranular and intergranular stress corrosion cracking was influenced by more than one alloying and impurity element in a complex manner.

Yield strength of unirradiated model alloys, measured in BWR-like water at 289°C, was nearly constant at ≈200 MPa and was more or less independent of Si concentration. However, as the alloys were irradiated to $\approx 0.3 \times 10^{21}$ n·cm^{-2} and $\approx 0.9 \times 10^{21}$ n·cm^{-2}, the increase in yield strength was significantly lower in alloys that contain >0.9 wt.% Si than in alloys that contain <0.8 wt.% Si. This observation indicates that the nature of irradiation-induced hardening

centers and the degree of irradiation hardening is significantly influenced by the Si content of the alloy. A similar influence was not observed for C and N. Among laboratory heats of Types 304 and 304L stainless steel, alloys that contain <0.67 wt.% Si exhibited significant susceptibility to intergranular stress corrosion cracking, whereas heats with 0.8-1.5 wt.% Si exhibited negligible susceptibility to intergranular stress corrosion cracking. However, an alloy with ≈1.9 wt.% Si exhibited some degree of susceptibility to intergranular stress corrosion cracking. These observations indicate that an Si content between ≈0.8 and ≈1.5 wt.% is beneficial in delaying the onset of, or suppressing, susceptibility to irradiation-assisted stress corrosion cracking.

Fracture toughness J–R curve tests have been conducted on four heats of Type 304 stainless steel that were irradiated to fluence levels of ≈0.3 and 0.9 x 10^{21} n·cm^{-2} (E > 1 MeV) (≈0.45 and 1.35 dpa) at ≈288°C in a helium environment in the Halden boiling heavy water reactor. The tests were performed on 1/4–T compact tension specimens in air at 288°C; crack extensions were determined by both DC potential and elastic unloading compliance techniques. Neutron irradiation at 288°C to 0.9 x 10^{21} n·cm^{-2} (E > 1 MeV) (1.35 dpa) decreased the fracture toughness of all of the steels. For these materials, minor differences in the chemical composition of the steels, e.g., differences in nickel content or silicon content, have little or no effect on the fracture toughness of irradiated steels. The commercial heats exhibited fracture toughness that is superior to the fracture toughness of laboratory heats. For steels irradiated to 0.9 x 10^{21} n·cm^{-2} (E > 1 MeV) (1.35 dpa), the J_{IC} values are ≈300 kJ/m^2 for the commercial heats and ≈38 kJ/m^2 for laboratory heats. The data from commercial heats fall within the scatter band for the data obtained at higher temperatures.

The resistance of Alloys 600 and 690 to EAC in simulated LWR coolant environments is being evaluated. Fatigue CGR tests are being conducted in air and LWR coolant environments on CT specimens of several heats of Alloys 600 and 690 in annealed and in annealed and thermally treated conditions. During the current reporting period, the existing fatigue crack growth data on Alloys 600 and 690 have been analyzed to establish the effects of temperature, load ratio, frequency, and stress intensity range ΔK on crack growth rates in air. Correlations have been developed for estimating the CGRs of Alloys 600 and 690 as a function of stress intensity range ΔK, load ratio R, and temperature. The results indicate that the CGRs of Alloys 600 and 690 in air are relatively insensitive to changes in frequency.

Comparison with the available experimental data shows that the PLEDGE code provides conservative predictions of crack growth rates in unirradiated sensitized materials if an appropriate value is chosen for the parameter used to characterize the sensitization denoted by electropotentiokinetic reactivation (EPR). For applications to unirradiated weldments, a value of EPR = 15 C/cm^2 appears appropriate and yields a moderate degree of conservatism. With this value for EPR, PLEDGE should give somewhat conservative predictions for IGSCC under constant and cyclic loads and provide a conservative estimate for environmentally assisted fatigue, i.e., transgranular crack growth, under cyclic loading. The choice of EPR = 15 C/cm^2 ought to provide sufficient conservatism in application to weldments that the predictions can also be applied to irradiated components with fluence < 5 x 10^{20} n/cm^2. For environmentally assisted fatigue in unsensitized materials, the choice of EPR = 0 C/cm^2 may not give conservative estimates in the low-conductivity water chemistries characteristic of current BWR operation. Some additional margin appears appropriate. This could be provided again by assuming EPR = 15 C/cm^2, but while other approaches (e.g., an appropriate multiplier) could be used, they would have to be justified by comparison with appropriate data.

PLEDGE appears to overestimate the deleterious effect of impurity additions, and its predictions become more conservative for conductivities > 0.2 μS/cm. It also appears to overestimate the deleterious effect of sensitization as characterized by EPR, at least for EPR values > 20 C/cm^2. Because current BWRs generally operate with conductivities much lower than 0.2 μS/cm^2 and most weldments will have sensitization levels < 15 C/cm^2, these shortcomings of the model are of limited importance. However, it is important to recognize that comparing PLEDGE predictions with data for high conductivities or high EPR could give a misleading picture of the degree of conservatism in PLEDGE predictions. Appropriate estimates of the mean error, i.e., the mean value of the ratio of the predicted crack growth rate to the observed crack growth rate, for PLEDGE predictions are provided by the results for low-conductivity data given in Table 17 of this report.

Acknowledgments

The authors thank T. M. Galvin, J. Tezak, R. W. Clark, and D. R. Perkins for their contributions to the experimental effort. This work is sponsored by the Office of Nuclear Regulatory Research, U.S. Nuclear Regulatory Commission, under Job Code W6610; Program Manager: Dr. M. B. McNeil.

1 Introduction

The U.S. Nuclear Regulatory Commission (NRC) and its predecessor, the U.S. Atomic Energy Commission, have conducted research programs that address the aging of reactor components. The results of the research have been used to evaluate and establish regulatory guidelines to ensure acceptable levels of reliability for light water reactor (LWR) components. The products of this program have been technical reports, methodologies for evaluating licensee submittals, and other inputs to the regulatory process. Results have led to the resolution of regulatory issues, as well as to the development, validation, and improvement of regulations and regulatory guides. The present research on the effects of simulated reactor coolant environments on cracking of reactor components was initiated to resolve the remaining critical technical issues related to cracking phenomena in LWR components. Initially, this project addressed cracking of boiling water reactor (BWR) pipes. Subsequently, in response to requests from the NRC Division of Nuclear Reactor Regulation (NRR) for assistance in dealing with developing cracking problems in aging reactors, the focus shifted to other problems in environmentally assisted cracking (EAC) of LWR components.

The overall objective of this program is to provide data and physical models to be used by the NRC staff in assessing environmentally assisted degradation of primary pressure boundary components in LWRs. The research is divided into five tasks:

(a) *Environmental effects on fatigue, crack growth, and stress corrosion cracking*
Fatigue and EAC of piping, pressure vessels, and core components in LWRs are important concerns during plant operation and extended reactor lifetimes. The degradation processes in U.S. reactors include fatigue, intergranular stress corrosion cracking (IGSCC), and propagation of fatigue or stress corrosion cracks that initiate in the weld-sensitized heat-affected zones of stainless steel (SS) components. Occurrences of mechanical–vibration– and thermal-fluctuation-induced fatigue failures in LWR plants have also been documented. The objective of this task is to improve fatigue design curves and assess the additivity of fatigue damage in piping and vessel steels under load histories that are typical of LWR components. Results of this work will be used to assess industry fatigue evaluations that are related to license renewal.

(b) *Component vulnerability to irradiation-assisted stress corrosion cracking*
Irradiation–assisted stress corrosion cracking (IASCC) of in–core components in both BWRs and pressurized water reactors (PWRs) is becoming a more common problem as reactors age. The general pattern of the observed failures indicates that as nuclear plants age and neutron fluence increases, many apparently nonsensitized austenitic materials become susceptible to intergranular failure by IASCC. Some of these failures have been reported for components that are subjected to relatively low or negligible stress levels, e.g., control–blade sheaths and handles and instrument dry tubes of BWRs. Although most failed components can be replaced, it would be very difficult or impractical to replace some safety–significant structural components, such as the BWR top guide, core plate, and shroud. The objective of this task is to provide data and models that are needed to assess industry analyses of the likelihood of degradation and failure of

core internal components that are due to IASCC, and to evaluate licensee submissions related to inspection and remediation.

(c) *Cracking of nickel alloy components of LWR primary systems*
Internal components of reactor vessels are made of Ni-based alloys, e.g., Alloys 600, X750, and 182, which are susceptible to IGSCC. The causes and mechanisms of this cracking are not adequately understood, and the uncertainty is increased when licensee submissions are evaluated for factors such as damage accumulation and inspection intervals. The objective of this task is to provide technical data on the effects of cracks in Ni–alloy components on the residual life, inspection, and repair of the component. The results will be used to support NRR staff assessments of industry crack–growth models, and potential detection and mitigation measures.

(d) *Analysis of postweld heat treatment processes and validation of flaw acceptance criteria*
The objective of this task is to evaluate the effect of postweld heat treatment on long–term resistance to environmental cracking by assessing sensitization and other microstructural changes. This evaluation will provide the NRC with insights for use in reviewing licensee submittals.

(e) *Assessment of industry crack-growth models*
This task has two objectives. The first is to perform an independent evaluation of industry models that are used to establish inspection intervals and repair criteria. The second objective is to perform more detailed analyses of flaw acceptance criteria.

2 Environmental Effects on Fatigue Strain-versus-Life (S–N) Behavior of Primary Pressure Boundary Materials (O. K. Chopra and W. J. Shack)

Experience with operating nuclear power plants worldwide reveals that many failures can be attributed to fatigue; examples include piping components, nozzles, valves, and pumps.[1–3] In most cases, these failures have been associated with thermal loading that is due to thermal stratification or thermal striping, or with mechanical loading that is due to vibratory loading. Significant thermal loadings due to flow stratification were not included in the original design basis analysis. The effects of these loadings may also have been aggravated by corrosion effects that are due to exposure to high–temperature aqueous environments. Fatigue cracks have been observed in pressurizer surge lines in PWRs (NRC Bulletin No. 88–11), and in feedwater lines connected to nozzles of pressure vessels in BWRs and steam generators in PWRs (NRC IE Bulletin, 79–13; NRC Information Notice 93–20). These cracks have been attributed to corrosion fatigue (NRC IE Bulletin, 79–13) or strain–induced corrosion cracking[4] caused by cyclic loading that is due to thermal stratification during start–up (hot standby) and shut–down periods.

2.1 Introduction

Cyclic loadings on a structural component occur because of changes in mechanical and thermal loadings as the system goes from one load set (e.g., pressure, temperature, moment, and force loading) to any other load set. For each load set, an individual fatigue usage factor is determined by the ratio of the number of cycles anticipated during the lifetime of the component to the allowable cycles. Figures I–9.1 through I–9.6 of Appendix I to Section III of the ASME Boiler and Pressure Vessel Code specify design fatigue curves that define the allowable number of cycles as a function of applied stress amplitude. The cumulative usage factor (CUF) is the sum of the individual usage factors, and the ASME Code Section III requires that the CUF at each location must not exceed 1.

The ASME Code fatigue design curves, given in Appendix I of Section III, are based on strain–controlled tests of small polished specimens at room temperature in air. The fatigue design curves were developed from the best–fit curves of the experimental data by first adjusting for the effects of mean stress on fatigue life and then reducing the fatigue life at each point on the adjusted curve by a factor of 2 on strain or 20 on cycles, whichever was more conservative. As described in the Section III criteria document, these factors were intended to account for data scatter (heat–to–heat variability), effects of mean stress or loading history, and differences in surface condition and size between the test specimens and actual components. The factors of 2 and 20 are not safety margins but rather conversion factors that must be applied to the experimental data to obtain reasonable estimates of the lives of actual reactor components. However, because the mean fatigue curve used to development the current Code design curve for austenitic SSs does not accurately represent the available experimental data,[1,2] the current Code design curve for SSs includes a reduction of only ≈1.5 and 15 from the mean curve for the SS data, not the 2 and 20 originally intended.

As explicitly noted in Subsection NB–3121 of Section III of the Code, the data on which the design fatigue curves (Figs. I–9.1 through I–9.6) are based did not include tests in the presence of corrosive environments that might accelerate fatigue failure. Article B–2131 in

Appendix B to Section III states that the owner's design specifications should provide information about any reduction to design fatigue curves that has been necessitated by environmental conditions. Existing fatigue strain–vs.–life (S–N) data illustrate potentially significant effects of light water reactor (LWR) coolant environments on the fatigue resistance of carbon steels (CSs) and low–alloy steels (LASs),[3–14] as well as of austenitic stainless steels (SSs),[2,15–24] (Fig. 1). Under certain environmental and loading conditions, fatigue lives of CSs can be a factor of 70 lower in the environment than in air.[4,12] Therefore, the margins in the ASME Code may be less conservative than originally intended.

Two approaches have been proposed for incorporating the effects of LWR environments into ASME Section III fatigue evaluations: (a) develop new design fatigue curves for LWR applications, and (b) use a fatigue life correction factor to account for environmental effects. Both approaches are based on the existing fatigue S–N data in LWR environments, i.e., the best–fit curves to the experimental fatigue S–N data in LWR environments are used to obtain the design curves or fatigue life correction factor. As and when more data became available, the best–fit curves were modified and updated to include the effects of various material, loading, and environmental parameters on fatigue life. Interim design fatigue curves that address environmental effects on fatigue life of carbon and low–alloy steels and austenitic SSs were first proposed by Majumdar et al.[25] Design fatigue curves based on a rigorous statistical analysis of the fatigue S–N data in LWR environments were developed by Keisler et al.[26,27] Results of the statistical analysis have also been used to estimate the probability of fatigue cracking in reactor components. The Idaho National Engineering Laboratory (INEL) assessed the significance of the interim fatigue design curves by performing fatigue evaluations of a sample of components in the reactor coolant pressure boundary.[28] In all, six locations were evaluated from facilities designed by each of the four U.S. nuclear steam supply system vendors. Selected components from older vintage plants designed using the B31.1 Code were also included in the evaluation. The design curves and statistical models for estimating fatigue lives in LWR environments have recently been updated for carbon and low–alloy steels[12–14] and austenitic SSs.[2,24]

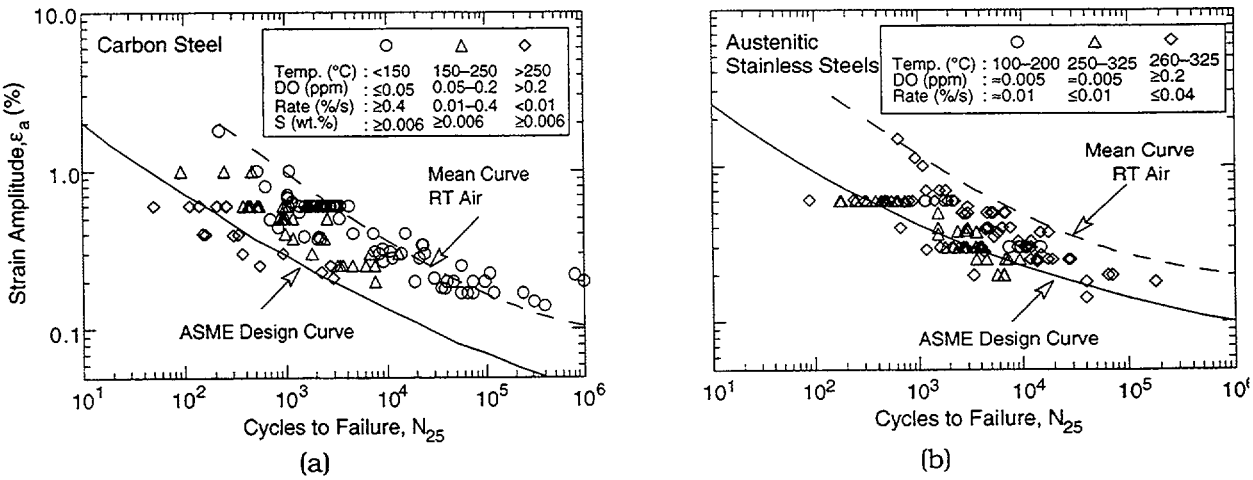

Figure 1. S–N data for (a) carbon steels and (b) austenitic stainless steels in water; RT = room temperature

The alternative approach, proposed initially by Higuchi and Iida,[4] considers the effects of reactor coolant environments on fatigue life in terms of a fatigue life correction factor F_{en},

which is the ratio of the life in air to that in water. To incorporate environmental effects into the ASME Code fatigue evaluations, a fatigue usage for a specific load set, based on the current Code design curves, is multiplied by the correction factor. Specific expressions for F_{en}, based on the statistical models[2,12-14,29,30] and on the correlations developed by the Environmental Fatigue Data Committee of Thermal and Nuclear Power Engineering Society of Japan,[31] have been proposed.

This paper summarizes the data available on the effects of various material, loading, and environmental parameters on the fatigue lives of carbon and low-alloy steels and austenitic SSs. Effects of reactor coolant environment on the mechanism of fatigue crack initiation are discussed. The two methods for incorporating the effects of LWR coolant environments into the ASME Code fatigue evaluations are presented. Although estimates of fatigue lives based on the two methods may vary because of differences between the ASME mean curves used to develop the current design curves and the best-fit curves to the existing data used to develop the environmentally adjusted curves, either of these methods provides an acceptable approach to account for environmental effects.

2.2 Mechanism of Fatigue Crack Initiation

The formation of surface cracks and their growth as shear (stage I) and tensile (stage II) cracks to an "engineering" size (3 mm deep) constitute the fatigue life of a material, which is represented by the fatigue S-N curves. The curves specify, for a given stress or strain amplitude, the number of cycles needed to form an engineering crack. In polycrystalline metals and alloys, the period for the formation of surface cracks is negligible; surface cracks, 10 μm or longer, form quite early in life.[11,32-36] Consequently, fatigue life is considered to be composed entirely of crack propagation.[37]

The growth of fatigue cracks may be divided into three regimes: (a) an initial period, which is very sensitive to microstructure, involves growth of microstructurally small cracks (MSCs) and is characterized by decelerating growth rate (region AB in Fig. 2); (b) a final period of growth that can be predicted from fracture mechanics methodology and is characterized by accelerating crack growth rate (region CD); and (c) a transition period that is controlled by a combination of the two regimes (region BC). Fatigue cracks greater than the critical length of MSCs show little or no influence from microstructure and are called mechanically small cracks. The transition from an MSC to a mechanically small crack has been estimated to occur at a crack size approximately eight times the unit size of the microstructure, i.e., 100-150 μm crack size. Conventionally, the number of cycles needed to form mechanically small cracks has been defined as the "initiation" stage (region ABC in Fig. 2), and growth of the mechanically small cracks to engineering size as the "propagation" stage. The reduction in life in LWR environments may arise from an increase in growth rates of cracks during the initial stage of MSC and shear crack growth and/or during the transition and final stage of tensile-crack growth.

The reduction in fatigue life in high-temperature water has often been attributed to easier crack initiation because surface micropits that occur in high-temperature water environments are thought to act as stress raisers and provide preferred sites for the formation of fatigue cracks.[5] However, experimental data do not support this argument; the fatigue lives of carbon and low-alloy steel specimens that have been preoxidized at 288°C in high-dissolved-oxygen (high-DO) water and then tested in air are identical to those of unoxidized specimens.[12] If the

micropits were responsible for the reduction in life, specimens preexposed to high-DO water and tested in air should show a decrease in life. Also, the fatigue limit of these steels should be lower in water than in air. Data from specimens in high-DO water indicate that the fatigue limit is either the same as, or ≈20% higher, in water than in air.[12]

The enhanced growth rates of long cracks in pressure vessel and piping steels in LWR environments have been attributed to either slip oxidation/dissolution[38] or hydrogen-induced cracking[39] mechanisms. Both mechanisms depend on the rates of oxide rupture, passivation, and liquid diffusion. Therefore, it is often difficult to differentiate between the two processes or to establish their relative contributions to crack growth in LWR environments.

Studies on crack initiation in smooth fatigue specimens indicate that the decrease in fatigue life of CSs and LASs in LWR environments is caused primarily by the effects of environment on the growth of cracks <100 μm deep.[12,34] When compared with crack growth rates in air, growth rates in high-DO water are nearly two orders of magnitude higher for cracks that are <100 μm and one order of magnitude higher for cracks that are >100 μm. Metallographic examinations of test specimens indicate that in high-DO water, <100-μm surface cracks grow entirely as tensile cracks normal to the stress, whereas in air or simulated PWR environments, they are at an angle of 45° to the stress axis.[34] Also, for CSs, <100-μm cracks propagate across both ferrite and pearlite regions, whereas in air they propagate only along ferrite regions. These results indicate that in high-DO water, growth of MSCs occurs by processes other than mechanical loading, e.g., by slip oxidation/dissolution process.

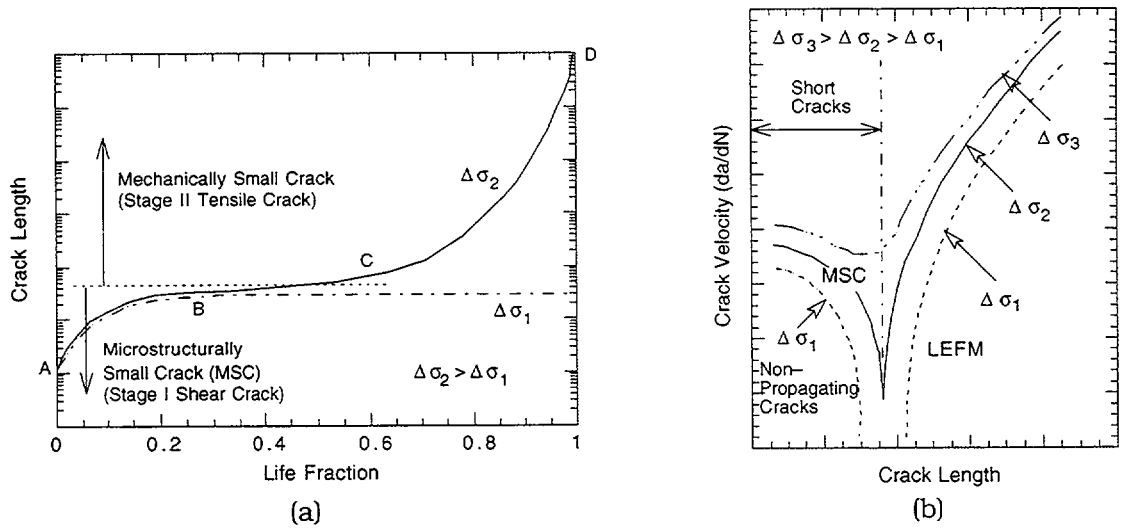

Figure 2. Schematic illustration of (a) growth of short cracks in smooth specimens as a function of fatigue life fraction and (b) crack velocity as a function of crack length

In high-DO water, crack initiation in CSs and LASs may be explained as follows: (a) surface microcracks form quite early in fatigue life; (b) during cyclic loading, the protective oxide film is ruptured at strains greater than the fracture strain of surface oxides, and the microcracks grow by anodic dissolution of the freshly exposed surface to crack depths greater than the critical length of MSCs; and (c) these mechanically small cracks grow to engineering size, and their growth, which is characterized by accelerating rates, can be predicted by fracture mechanics methodology.

Studies on crack initiation in austenitic SSs yield similar results; the decrease in fatigue life in LWR environments is caused primarily by the effects of environment on the growth of cracks that are <500 μm deep.[40] However, for SSs, fatigue lives are lower in low–DO water than in high–DO water; such results are difficult to reconcile in terms of the slip oxidation/dissolution mechanism. Also, SS specimens tested in water show well–defined fatigue striations, indicating that mechanical factors and not the slip dissolution/oxidation process are important.[24] The results indicate that environmentally assisted reduction in fatigue life of austenitic SSs is most likely caused by other mechanisms such as hydrogen–enhanced crack growth.

2.3 Fatigue S–N Data in LWR Environments

2.3.1 Carbon and Low–Alloy Steels

The fatigue lives of both CSs and LASs are decreased in LWR environments; the reduction depends on temperature, strain rate, DO level in water, and S content of the steel. Fatigue life is decreased significantly when four conditions are satisfied simultaneously, viz., strain amplitude, temperature, and DO in water are above a minimum level, and strain rate is below a threshold value. The S content in the steel is also important; its effect on life depends on the DO level in water. Although the microstructures and cyclic–hardening behavior of CSs and LASs differ significantly, environmental degradation of fatigue lives of these steels is very similar. For both steels, only a moderate decrease in life (by a factor of <2) is observed when any one of the threshold conditions is not satisfied. The effects of the critical parameters on fatigue life and their threshold values are summarized below.

(a) *Strain:* A minimum threshold strain is required for environmentally assisted decrease in fatigue lives of CSs and LASs.[12–14] The threshold value most likely corresponds to the rupture strain of the surface oxide film. Limited data suggest that the threshold value is ≈20% higher than the fatigue limit for the steel.

(b) *Strain Rate*: Environmental effects on fatigue life occur primarily during the tensile–loading cycle, and at strain levels greater than the threshold value required to rupture the surface oxide film. When any one of the threshold conditions is not satisfied, e.g., DO <0.05 ppm or temperature <150°C, the effects of strain rate are consistent with those in air, i.e., only the heats that are sensitive to strain rate in air show a decrease in life in water. When all other threshold conditions are satisfied, fatigue life decreases logarithmically with decreasing strain rate below 1%/s;[4,8,41] the effect of environment on life saturates at ≈0.001%/s.[12–14] The dependence of fatigue life on strain rate for A106–Gr B CS and A533–Gr B LAS is shown in Fig. 3. For A533–Gr B steel, the fatigue life at a strain rate of 0.0004%/s in high–DO water (≈0.7 ppm DO) is lower by more than a factor of 40 than that in air.

(c) *Temperature*: When other threshold conditions are satisfied, fatigue life decreases linearly with temperature above 150°C and up to 320°C.[4,5,8] Fatigue life is insensitive to temperatures below 150°C or when any other threshold condition is not satisfied.

(d) *Dissolved Oxygen in Water*: When other threshold conditions are satisfied, fatigue life decreases logarithmically with DO above 0.05 ppm; the effect saturates at ≈0.5 ppm

DO.[5,8] Fatigue life is insensitive to DO level below 0.05 ppm or when any other threshold condition is not satisfied.

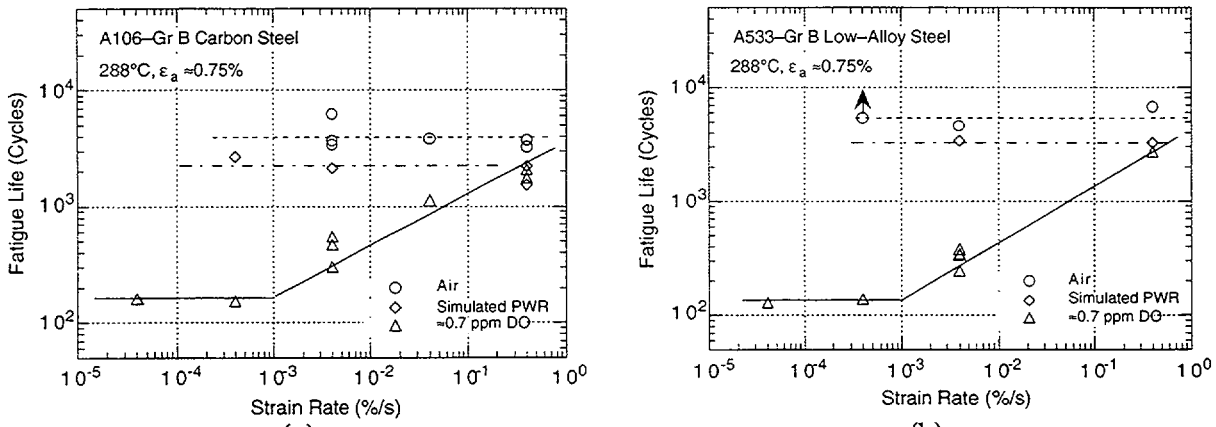

Figure 3. Dependence of fatigue lives of (a) carbon steels and (b) low–alloy steels on strain rate

(e) *S Content of Steel*: The effect of S content on fatigue life depends on the DO content in water. When the threshold conditions are satisfied and for DO contents ≤1.0 ppm, the fatigue life decreases with increasing S content. Limited data suggest that the effects of environment on life saturate at an S content of ≈0.015 wt.%.[12] At high DO levels, e.g., >1.0 ppm, fatigue life seems to be insensitive to S content in the range of 0.002–0.015 wt.%.[42] When any one of the threshold conditions is not satisfied, environmental effects on life are minimal and relatively insensitive to changes in S content.

2.3.2 Austenitic Stainless Steels

The fatigue lives of austenitic SSs are decreased in LWR environments; the reduction depends on strain rate, level of DO in water, and temperature.[18,22–24] The effects of LWR environments on fatigue life of wrought materials are comparable for Types 304, 316, and 316NG SSs. Although the fatigue lives of cast SSs are relatively insensitive to changes in ferrite content in the range of 12–28%,[18] the effects of loading and environmental parameters on the fatigue life of cast SSs differ somewhat. The significant results and threshold values of critical parameters are summarized below.

(a) *Strain*: A minimum threshold strain is required for environmentally assisted decrease in fatigue lives of austenitic SSs. Limited data suggest that the threshold strain range is between 0.32 and 0.36%.[19,24]

(b) *Dissolved Oxygen in Water*: For wrought austenitic SSs, environmental effects on fatigue life are more pronounced in low-DO, i.e., <0.01 ppm DO, than in high-DO, i.e., ≥0.1 ppm DO, water.[18,24] In high-DO water, environmental effects are moderate (less than a factor of 2 decrease in life) when conductivity is maintained at <0.1 μS/cm and electrochemical potential (ECP) of the steel has reached a stable value (Fig. 4). For fatigue tests in high-DO water, the SS specimens must be soaked for 5 to 6 days for the ECP of the steel to reach a stable value. Figure 4 shows that although fatigue life is decreased by a factor

of ≈2 when conductivity of water is increased from ≈0.07 to 0.4 μS/cm, the period for presoaking appears to have a greater effect on life than does the conductivity of water. In low–DO water, the additions of lithium and boron, or low conductivity, or preexposing the specimen for ≈5 days prior to the test, or dissolved hydrogen, have no effect on fatigue life of Type 304 SS (Table 1 Also, for cast austenitic SSs, the effect of DO content is somewhat different; the fatigue lives are approximately the same in both high– or low–DO water and are comparable to those observed for wrought SSs in low–DO water.[24]

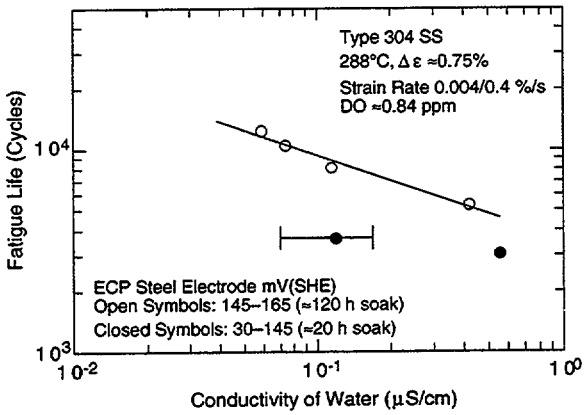

Figure 4.
Effects of conductivity of water and soak period on fatigue lives of Type 304 SS in high–DO water

Table 1. Fatigue test results for Type 304 austenitic SS at 288°C

Test No.	Diss. Oxygen[a] (ppb)	Diss. Hydrogen (cc/kg)	Li (ppm)	Boron (ppm)	Pre–soak (days)	pH at RT	Conduc-tivity[b] (μS/cm)	ECP SS mV (SHE)	Ten. Rate (%/s)	Stress Range (MPa)	Strain Range (%)	Life N_{25} (Cycles)
1805	–	–				–	–	–	4.0E-3	467.9	0.76	14,410
1808	4	23	2	1000	1	6.4	18.87	–686	4.0E-3	468.3	0.77	2,850
1821	2	23	2	1000	1	6.5	22.22	–693	4.0E-3	474.3	0.76	2,420
1859	2	23	2	1000	1	6.5	18.69	–692	4.0E-3	471.7	0.77	2,420
1861	1	23	–	–	1	6.2	0.06	–610	4.0E-3	463.0	0.79	2,620
1862	2	23	–	–	5	6.2	0.06	–603	4.0E-3	466.1	0.78	2,450
1863	1	–	–	–	5	6.3	0.06	–520	4.0E-3	476.5	0.77	2,250

[a]DO and ECPs measured in effluent.
[b]Conductivity of water measured in feedwater supply tank.

(c) *Strain Rate*: In high–DO water (conductivity <0.1 μS/cm and stable ECP of the steel), fatigue life is insensitive to changes in strain rate. In low–DO water, fatigue life decreases logarithmically with decreasing strain rate below ≈0.4%/s; the effect of environment on life saturates at ≈0.0004%/s for wrought SSs.[19,24] Existing data are too sparse to define the saturation strain rate for cast austenitic SSs.

(d) *Temperature*: Existing data are also too sparse to establish the effects of temperature on fatigue life over the entire range from room temperature to reactor operating temperatures. Limited data indicate that environmental effects on fatigue life are minimal below 200°C and significant above 250°C;[19] life appears to be relatively insensitive to changes in temperature in the range of 250–330°C. The Pressure Vessel Research Council (PVRC) steering committee for cyclic life and environmental effects (CLEE) has proposed a ramp function to describe temperature effects on the fatigue lives of austenitic SSs; environmental effects are moderate at temperatures below 180°C, significant above 220°C, and increase linearly from 180 to 220°C.[43]

2.4 Incorporating Environmental Effects into ASME Fatigue Evaluations

Two procedures are currently being proposed for incorporating effects of LWR coolant environments into the ASME Section III fatigue evaluations: (a) develop a new set of environmentally adjusted design fatigue curves[2,12,14,24] or (b) use fatigue life correction factors, F_{en}, to adjust the current ASME Code fatigue usage values for environmental effects.[2,14,29,30] For both approaches, the range and bounding values must be defined for key service parameters that influence fatigue life. It has been demonstrated that estimates of fatigue lives based on the two methods may differ because of differences between the ASME mean curves used to develop the current design curves and the best-fit curves to the existing data used to develop the environmentally adjusted curves. However, either of these methods provides an acceptable approach to account for environmental effects.

2.4.1 Design Fatigue Curves

A set of environmentally adjusted design fatigue curves can be developed from the best-fit stress-vs.-life curves to the experimental data in LWR environments by using the same procedure that was used to develop the current ASME Code design fatigue curves. The stress-vs.-life curves are obtained from the strain-vs.-life curves, e.g., stress amplitude is the product of strain amplitude and elastic modulus. The best-fit experimental curves are first adjusted for the effect of mean stress by using the modified Goodman relationship

$$S_a' = S_a\left(\frac{\sigma_u - \sigma_y}{\sigma_u - S_a}\right) \qquad \text{for } S_a < \sigma_y, \tag{1}$$

and

$$S_a' = S_a \qquad \text{for } S_a > \sigma_y, \tag{2}$$

where S_a' is the adjusted value of stress amplitude, and σ_y and σ_u are yield and ultimate strengths of the material, respectively. Equations 1 and 2 assume the maximum possible mean stress and typically give a conservative adjustment for mean stress, at least when environmental effects are not significant. The design fatigue curves are then obtained by lowering the adjusted best-fit curve by a factor of 2 on stress or 20 on cycles, whichever is more conservative, to account for differences and uncertainties in fatigue life that are associated with material and loading conditions.

Statistical models based on the existing fatigue S-N data have been developed for estimating the fatigue lives of pressure vessel and piping steels in air and LWR environments.[12,14,24] In air at room temperature, the fatigue life N of CSs is represented by

$$\ln(N) = 6.564 - 1.975 \ln(\varepsilon_a - 0.113) \tag{3}$$

and of LASs by

$$\ln(N) = 6.627 - 1.808 \ln(\varepsilon_a - 0.151), \tag{4}$$

where ε_a is applied strain amplitude (%). In LWR environments, the fatigue life of CSs is represented by

$$\ln(N) = 6.010 - 1.975 \ln(\varepsilon_a - 0.113) + 0.101\ S^*\ T^*\ O^*\ \dot{\varepsilon}^* \quad (5)$$

and of LASs by

$$\ln(N) = 5.729 - 1.808 \ln(\varepsilon_a - 0.151) + 0.101\ S^*\ T^*\ O^*\ \dot{\varepsilon}^*, \quad (6)$$

where S^*, T^*, O^*, and $\dot{\varepsilon}^*$ are transformed S content, temperature, DO, and strain rate, respectively, defined as follows:

$$\begin{aligned} S^* &= 0.015 && (DO > 1.0\ ppm) \\ S^* &= S && (DO \leq 1.0\ ppm\ \&\ 0 < S \leq 0.015\ wt.\%) \\ S^* &= 0.015 && (DO \leq 1.0\ ppm\ \&\ S > 0.015\ wt.\%) \end{aligned} \quad (7)$$

$$\begin{aligned} T^* &= 0 && (T < 150°C) \\ T^* &= T - 150 && (T = 150–350°C) \end{aligned} \quad (8)$$

$$\begin{aligned} O^* &= 0 && (DO < 0.05\ ppm) \\ O^* &= \ln(DO/0.04) && (0.05\ ppm \leq DO \leq 0.5\ ppm) \\ O^* &= \ln(12.5) && (DO > 0.5\ ppm) \end{aligned} \quad (9)$$

$$\begin{aligned} \dot{\varepsilon}^* &= 0 && (\dot{\varepsilon} > 1\%/s) \\ \dot{\varepsilon}^* &= \ln(\dot{\varepsilon}) && (0.001 \leq \dot{\varepsilon} \leq 1\%/s) \\ \dot{\varepsilon}^* &= \ln(0.001) && (\dot{\varepsilon} < 0.001\%/s). \end{aligned} \quad (10)$$

The discontinuity in the value of O^* at 0.05 ppm DO is due to an approximation and does not represent a physical phenomenon. In air at room temperature, the fatigue data for Types 304 and 316 SS are best represented by

$$\ln(N) = 6.703 - 2.030 \ln(\varepsilon_a - 0.126) \quad (11)$$

and for Type 316NG, by

$$\ln(N) = 7.422 - 1.671 \ln(\varepsilon_a - 0.126). \quad (12)$$

In LWR environments, fatigue data for Types 304 and 316 SS are best represented by

$$\ln(N) = 5.768 - 2.030 \ln(\varepsilon_a - 0.126) + T'\ \dot{\varepsilon}'\ O' \quad (13)$$

and for Type 316NG, by

$$\ln(N) = 6.913 - 1.671 \ln(\varepsilon_a - 0.126) + T'\ \dot{\varepsilon}'\ O', \quad (14)$$

where T', $\dot{\varepsilon}'$, and O' are transformed temperature, strain rate, and DO, respectively, defined as follows:

$$
\begin{aligned}
T' &= 0 && (T < 180°C) \\
T' &= (T - 180)/40 && (180 \le T < 220°C) \\
T' &= 1 && (T \ge 220°C) \qquad (15)
\end{aligned}
$$

$$
\begin{aligned}
\dot{\varepsilon}' &= 0 && (\dot{\varepsilon} > 0.4\%/s) \\
\dot{\varepsilon}' &= \ln(\dot{\varepsilon}/0.4) && (0.0004 \le \dot{\varepsilon} \le 0.4\%/s) \\
\dot{\varepsilon}' &= \ln(0.0004/0.4) && (\dot{\varepsilon} < 0.0004\%/s) \qquad (16)
\end{aligned}
$$

$$
\begin{aligned}
O' &= 0.260 && (DO < 0.05 \text{ ppm}) \\
O' &= 0 && (DO \ge 0.05 \text{ ppm}). \qquad (17)
\end{aligned}
$$

The models are recommended for predicted fatigue lives of $\le 10^6$ cycles. The design fatigue curves were obtained from the best-fit curves, represented by Eqs. 3–6 for CSs and LASs, and by Eqs. 11 and 13 for austenitic SSs. To be consistent with the current Code design curves, the mean-stress-adjusted best-fit curves were decreased by the same margins on stress and cycles that are present in the current Code curves, e.g., the adjusted best-fit curves were decreased by a factor of 2 on stress for CSs and LASs and by a factor of 1.5 for austenitic SSs. A factor of 20 on life was used for all curves, although the actual margin on life is 10–16 for SSs because of the differences between the ASME mean curve and the best-fit curve to existing fatigue data.

The new design fatigue curves for CSs and LASs and austenitic SS in air are shown in Fig. 5, those in LWR coolant environments are shown in Figs. 6–8; only the portions of the

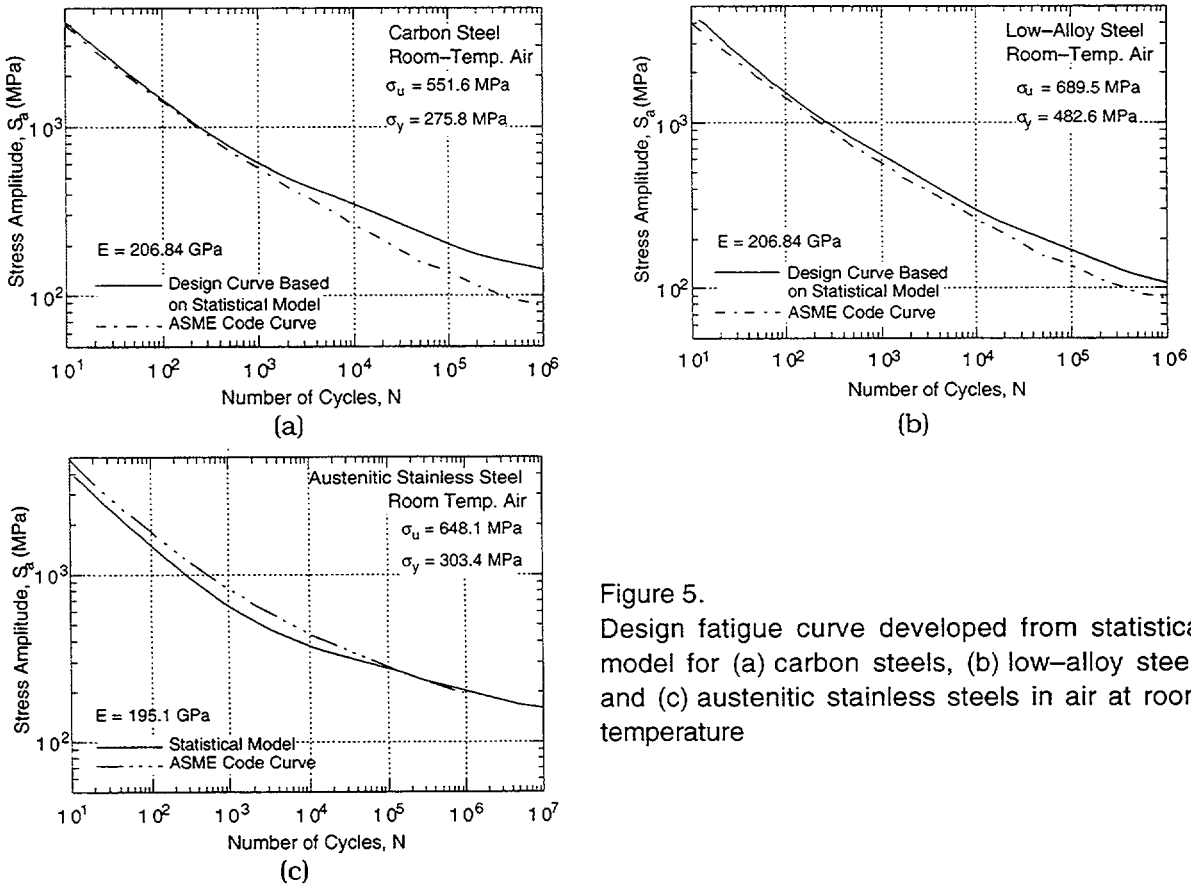

Figure 5.
Design fatigue curve developed from statistical model for (a) carbon steels, (b) low-alloy steels and (c) austenitic stainless steels in air at room temperature

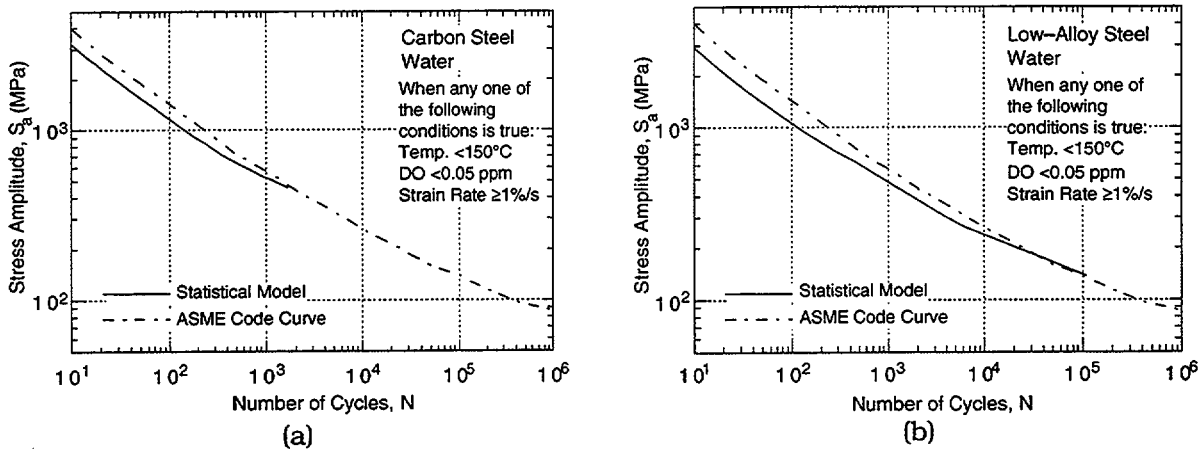

Figure 6. Design fatigue curves developed from statistical model for carbon and low–alloy steels under service conditions where one or more critical threshold values are not satisfied

environmentally adjusted curves that fall below the current ASME Code curve are shown in Figs. 6–8. Because the fatigue life of Type 316NG is superior to that of Types 304 or 316 SS, the design curves in Figs. 5 and 8 will be somewhat conservative for Type 316NG SS. For CSs and LASs, a set of design curves similar to those shown in Fig. 7 can be developed for low–S steels, i.e., steels with ≤0.007 wt.% S. The results indicate that in room-temperature air, the current ASME Code design curves for CSs and LASs are conservative with respect to the curves based on the statistical models, and those for austenitic SSs are nonconservative at stress levels above 300 MPa.

For environmentally adjusted design fatigue curves (Figs. 6–8), a minimum threshold strain is defined, below which environmental effects are modest. The threshold strain for CSs and LASs appears to be ≈20% higher than the fatigue limit of the steel. This translates into strain amplitudes of 0.140 and 0.185%, respectively, for CSs and LASs. These values must be adjusted for mean stress effects and variability due to material and experimental scatter. The threshold strain amplitudes are decreased by ≈15% for CSs and by ≈40% for LASs to account for the effects of mean stress, and by a factor of 1.7 on strain to provide 90% confidence for the variations in fatigue life associated with material variability and experimental scatter.[26] Thus, a threshold strain amplitude of 0.07% (or a stress amplitude of 145 MPa) is obtained for both CSs and LASs. The existing fatigue data indicate a threshold strain range of ≈0.32% for austenitic SSs. This value is decreased by ≈10% to account for mean stress effects and by a factor of 1.5 to account for uncertainties in fatigue life that are associated with material and loading variability. Thus, a threshold strain amplitude of 0.097% (stress amplitude of 189 MPa) is obtained for austenitic SSs. The PVRC steering committee for CLEE[43] has proposed a ramp for the threshold strain; a lower strain amplitude below which environmental effects are insignificant, a slightly higher strain amplitude above which environmental effects decrease fatigue life, and a ramp between the two values. The two strain amplitudes are 0.07 and 0.08% for carbon and low–alloy steels, and 0.10 and 0.11% for austenitic SSs (both wrought and cast SS). These threshold values have been used in developing Figs. 7 and 8.

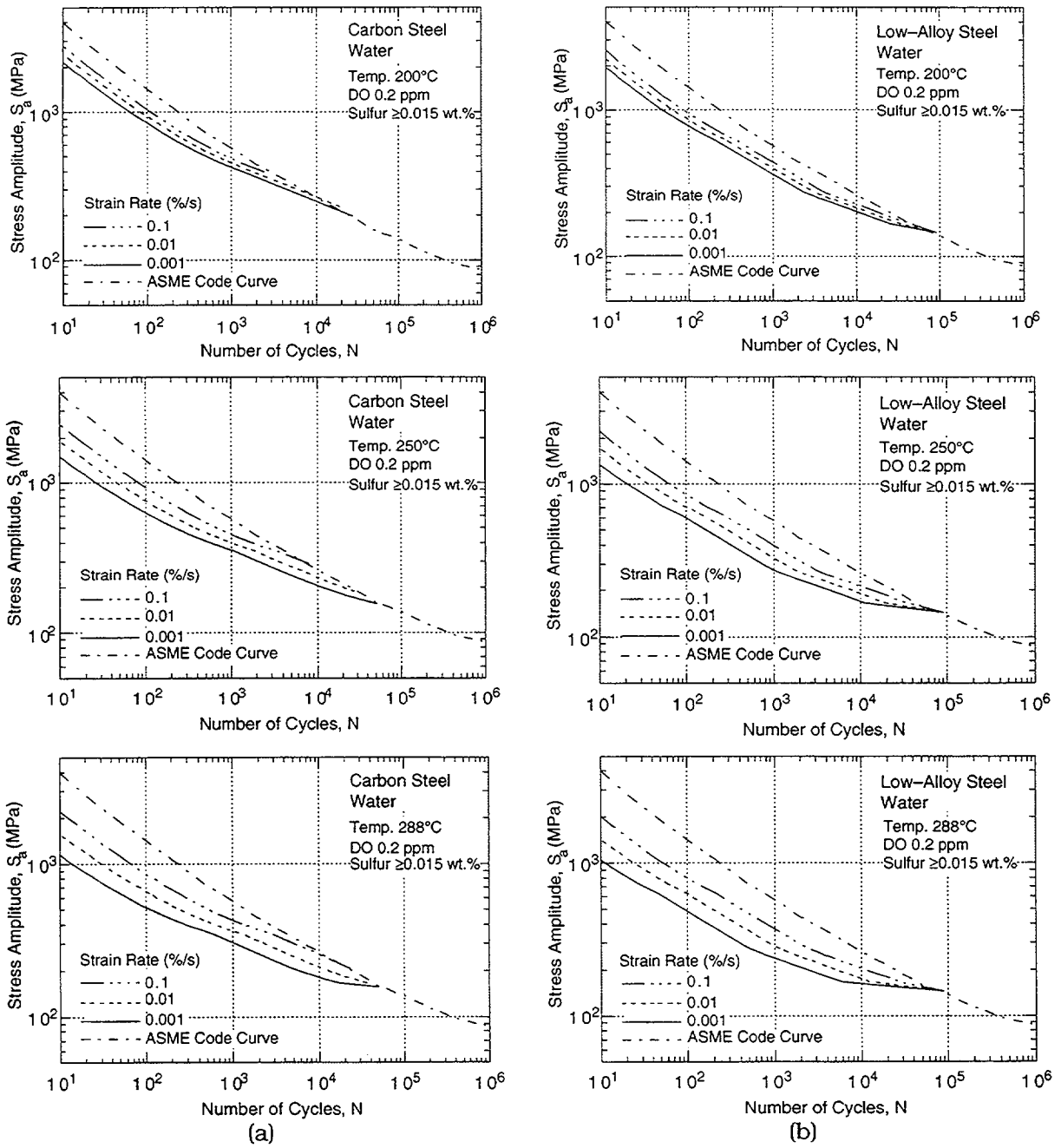

Figure 7. Design fatigue curves developed from statistical model for carbon and low–alloy steels under service conditions where one or more critical threshold values are not satisfied

2.4.2 Fatigue Life Correction Factor

The effects of reactor coolant environments on fatigue life have also been expressed in terms of a fatigue life correction factor F_{en}, which is the ratio of life in air at room temperature to that in water at the service temperature.[4] A fatigue life correction factor F_{en} can be obtained from the statistical model (Eqs. 3–17), where

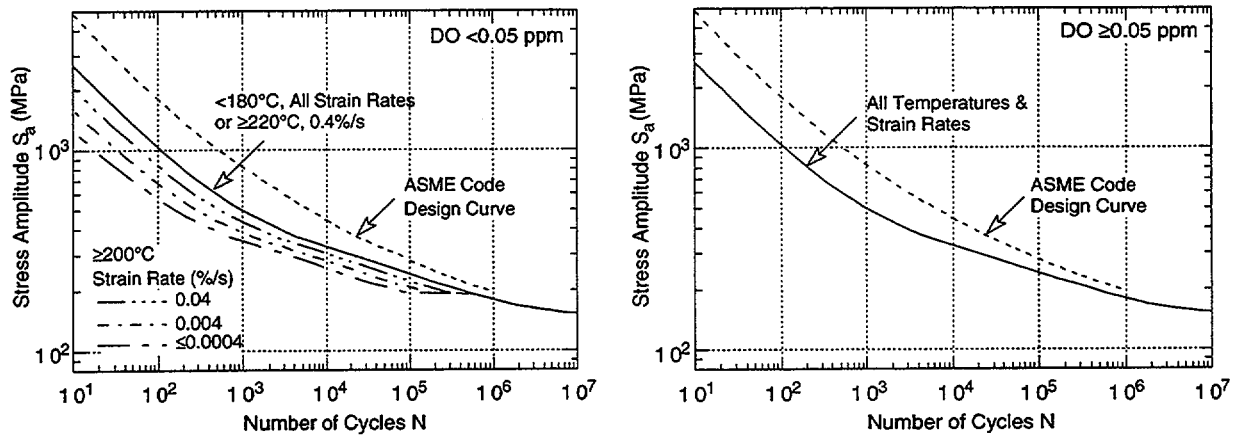

Figure 8. Design fatigue curves developed from statistical models for Types 304 and 316 SS in water with <0.05 and ≥0.05 ppm DO

$$\ln(F_{en}) = \ln(N_{RTair}) - \ln(N_{water}). \quad (18)$$

The fatigue life correction factor for CSs is given by

$$F_{en} = \exp(0.554 - 0.101\, S^*\, T^*\, O^*\, \dot{\varepsilon}^*), \quad (19)$$

for LASs, by

$$F_{en} = \exp(0.898 - 0.101\, S^*\, T^*\, O^*\, \dot{\varepsilon}^*), \quad (20)$$

and for austenitic SSs, by

$$F_{en} = \exp(0.935 - T'\, \dot{\varepsilon}'\, O'), \quad (21)$$

where the constants S^*, T^*, $\dot{\varepsilon}^*$ and O^* are defined in Eqs. 7–10, and T', $\dot{\varepsilon}'$ and O' are defined in Eqs. 15–17. A strain threshold is also defined, below which environmental effects are modest. The strain threshold is represented by a ramp, i.e., a lower strain amplitude below which environmental effects are insignificant, a slightly higher strain amplitude above which environmental effects are significant, and a ramp between the two values. Thus, the negative terms in Eqs. 19–21 are scaled from zero to their actual values between the two strain threshold. The two strain amplitudes are 0.07 and 0.08% for CSs and LASs, and 0.10 and 0.11% for austenitic SSs (both wrought and cast SS). To incorporate environmental effects into the Section III fatigue evaluation, a fatigue usage for a specific stress cycle, based on the current Code design fatigue curve, is multiplied by the correction factor. The experimental data adjusted for environmental effects, i.e., the product of experimentally observed fatigue life in LWR environments and F_{en}, are compared with the best-fit S–N curve in room-temperature air in Fig. 9.

A similar approach has been proposed by Mehta and Gosselin;[29,30] however, they defined F_{en} as the ratio of the life in air to that in water, both at service temperature. The F_{en} approach, also known as the EPRI/GE approach, has recently been updated to include the revised statistical models and the PVRC discussions on environmental fatigue evaluations.[44]

An "effective" fatigue life correction factor, expressed as $F_{en,eff} = F_{en}/Z$, is defined where Z is a factor that constitutes the perceived conservatism in the ASME Code design curves. A nonmandatory appendix, based on this procedure, is being proposed for inclusion in Section III of the ASME Code. The $F_{en,eff}$ approach presumes that all uncertainties have been anticipated and accounted for.

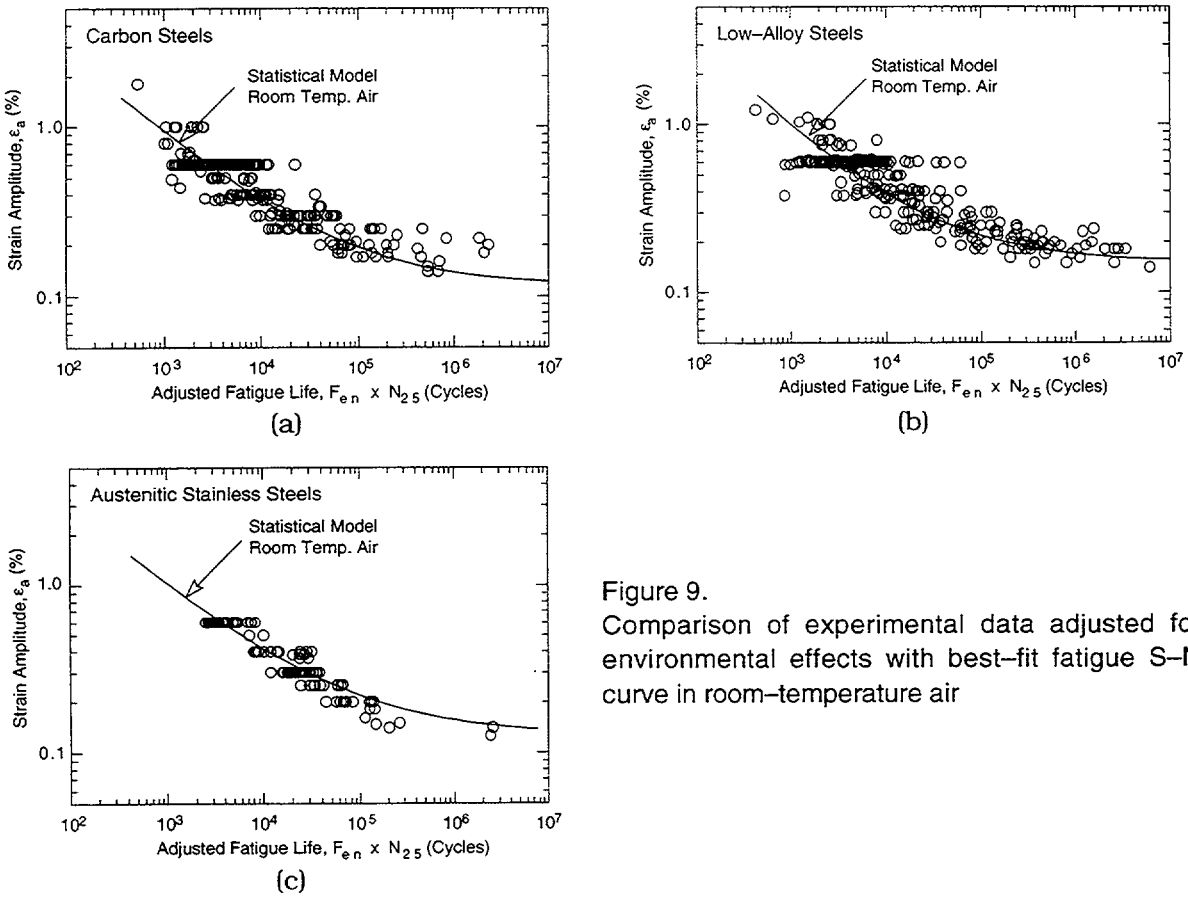

Figure 9.
Comparison of experimental data adjusted for environmental effects with best–fit fatigue S–N curve in room–temperature air

3 Irradiation–Assisted Stress Corrosion Cracking of Austenitic SS

3.1 Introduction

Failures of reactor–core internal components have been observed after accumulating fluence of >0.5 x 10^{21} n·cm^{-2} (E >1 MeV), or ≈0.7 dpa, in BWRs and at approximately one order of magnitude or higher fluences in some PWR components. The general pattern of the observed failures indicates that as nuclear plants age and neutron fluence increases, various nonsensitized austenitic SSs become susceptible to IG failure. Some components have cracked under minimal applied stress. Although most failed components can be replaced (e.g., PWR baffle-former bolts), some safety–significant structural components (e.g., the BWR top guide, shroud, and core plate) would be very difficult or costly to replace. Therefore, the structural integrity of these components at high fluence has been a subject of concern, and extensive research has been conducted to provide an understanding of this type of degradation, which is commonly known as irradiation-assisted stress corrosion cracking (IASCC).[45–78]

Irradiation produces profound effects on local coolant water chemistry and component microstructure. Neutron irradiation causes alteration of local microchemistry, microstructure, and mechanical properties of the core internal components, which are usually fabricated from ASTM Types 304, 304L, 316, or 348 SS. Irradiation produces defects, defect clusters, and defect-impurity complexes in grain matrices and alters the dislocation and dislocation loop structures, leading to radiation-induced hardening, and in many cases, flow localization via dislocation channeling. Irradiation also leads to changes in the stability of second–phase precipitates and the local alloy chemistry near grain boundaries, precipitates, and defect clusters. Grain–boundary microchemistry significantly different from bulk composition can be produced in association with not only radiation–induced segregation but also thermally driven equilibrium and nonequilibrium segregation of alloying and impurity elements.

Irradiation–induced grain–boundary depletion of Cr has been considered for many years to be the primary metallurgical process that causes IASCC. One of the most important factors that has been considered by many investigators to support the Cr–depletion mechanism is the observation that dependence on water chemistry (i.e., oxidizing potential) of intergranular stress corrosion cracking (IGSCC) of nonirradiated thermally sensitized material and of IASCC of BWR–irradiated solution–annealed material is similar. Other investigators have implicated radiation–induced segregation of ASTM–specified impurities such as Si, P, S, and other minor impurities not specified in the ASTM specification. However, the exact mechanism of IASCC still remains unknown. In general, IASCC is characterized by strong heat-to-heat variation in susceptibility, in addition to strong effects of irradiation condition, material type, and grade, even among materials of virtually identical chemical compositions. This indicates that the traditional interpretation based on the role of grain-boundary Cr depletion cannot completely explain the IASCC mechanism.

Therefore, an irradiation testing program has been conducted at ANL to investigate systematically the effects of alloying and impurity elements (Cr, Ni, Si, P, S, Mn, C, and N) on the susceptibility of austenitic stainless steels to IASCC at several fluence levels. In a previous study,[79] SSRT tests and fractographic analysis were conducted on model austenitic SS specimens irradiated at 289°C in helium in the Halden reactor to a "low-fluence" level of ≈0.3 x 10^{21} n·cm^{-2} (E > 1 MeV), or ≈0.43 dpa. Results of initial tests conducted on specimens that

were irradiated to a "medium-fluence" level of ≈0.9 x 10^{21} n·cm^{-2} (E > 1 MeV), or ≈1.3 dpa, have been reported in Ref. 80. This report describes complete test results that were obtained for all of the 23 "medium-fluence" specimens irradiated to ≈0.9 x 10^{21} n·cm^{-2} (E > 1 MeV). Initial results of correlation of the SSRT behavior with the compositional characteristics of the model alloys are also reported.

3.2 Slow-Strain-Rate-Tensile Test of Model Austenitic Stainless Steels Irradiated in the Halden Reactor (H. M. Chung, W. E. Ruther, and R. V. Strain)

3.2.1 Test Matrix, Specimen Fabrication, and Irradiation

Test Matrix

The irradiation test matrix was constructed according to the method of Taguchi, as described in Ref. 81. The base matrix followed Taguchi's standard orthogonal array L_{18} (2^1 x 3^7), which is an optimized matrix designed to determine systematically the effects of seven variables (i.e., bulk material concentrations of Cr, Si, P, S, Mn, C, and N) at three concentration levels, and one variable (Ni concentration) at two levels. A possible synergistic interaction was assumed only between Ni and Si. In this way, 18 statistically optimized alloys were designed and fabricated in the laboratory. In addition to the 18 statistically optimized alloys, 6 supplementary heats of commercial- and high-purity (CP and HP) grade Types 304, 316, and 348 SS were included in the test matrix.

Of these 24 alloys, 8 were replaced by commercially fabricated and purchased heats. Compositions of major impurities (i.e., Si, P, C, and N) of each of the 8 commercial heats matched closely those of each corresponding alloy designed according to the Taguchi's standard array L_{18} (2^1 x 3^7). The prefix "C" was added to the identification number of these 8 commercial heats, i.e., Heats C1, C3, C9, C10, C12, C16, C19, and C21 in Table 2.

The remaining 16 heats were fabricated in the laboratory; all were designated with identification numbers that began with "L". To this matrix of 24 alloys3 laboratory heats were added to test the effects of the fabrication procedure. Compositions of these 3 laboratory heats (i.e., Heats L25C3, L26C19, and L27C21 in Table 2) closely match those of the corresponding commercial heats (Heats C3, C19, and C21), respectively. Elemental compositions of the complete test matrix, comprising 27 model austenitic SS alloys, are given in Table 2.

Fabrication of Test Specimens

Slow-strain-rate tensile specimens were machined from solution-annealed and water-quenched plates or sheets that were fabricated from the 27 model austenitic SS alloys. The geometry of the SSRT specimens was 0.76 mm thick, 57.2 mm long, and 12.7 mm wide; and the gauge section of was 19.1 mm long and 3.1 mm wide. Gauge lengths and planes of the specimens were parallel to the rolling direction and plane of the sheets, respectively. Subsize compact-tension (1/4TCT) specimens were also irradiated in tandem in the same capsules with the SSRT specimens to determine J-R fracture toughness properties and crack growth rates (CGRs) after irradiation. Together, 96 SSRT and 24 CT specimens were prepared and irradiated in this study. After these specimens were mechanically machined in the shop, no additional heat-treatment was applied to any of the specimens. The machined specimens were

degreased in acetone and cleaned ultrasonically in alcohol before encapsulation in Type 304 SS capsules filled with research-grade He for irradiation in the Halden reactor.

Table 2. Elemental composition of 27 commercial and laboratory model austenitic stainless steel alloys irradiated in the Halden Reactor.

ANL	Source	Composition (wt.%)										
ID[a]	Heat ID	Ni	Si	P	S	Mn	C	N	Cr	O	B	Mo or Nb
C1	DAN-70378	8.12	0.50	0.038	0.002	1.00	0.060	0.060	18.11	-	<0.001	-
L2	BPC-4-111	10.50	0.82	0.080	0.034	1.58	0.074	0.102	17.02	0.0065	<0.001	-
C3	PNL-C-1	8.91	0.46	0.019	0.004	1.81	0.016	0.083	18.55	-	<0.001	-
L4	BPC-4-88	10.20	0.94	0.031	0.010	1.75	0.110	0.002	15.80	-	<0.001	-
L5	BPC-4-104	9.66	0.90	0.113	0.028	0.47	0.006	0.033	21.00	-	<0.001	-
L6	BPC-4-127	10.00	1.90	0.020	0.005	1.13	0.096	0.087	17.10	0.0058	<0.001	-
L7	BPC-4-112	10.60	0.18	0.040	0.038	1.02	0.007	0.111	15.40	0.0274	<0.001	-
L8	BPC-4-91	10.20	0.15	0.093	0.010	1.85	0.041	0.001	18.30	-	<0.001	-
C9	PNL-C-6	8.75	0.39	0.013	0.013	1.72	0.062	0.065	18.48	-	<0.001	-
C10	DAN-23381	8.13	0.55	0.033	0.002	1.00	0.060	0.086	18.19	-	<0.001	-
L11	BPC-4-93	8.15	0.47	0.097	0.009	1.02	0.014	0.004	17.40	-	<0.001	-
C12	DAN-23805	8.23	0.47	0.018	0.002	1.00	0.060	0.070	18.43	-	<0.001	-
L13	BPC-4-96	8.18	1.18	0.027	0.022	0.36	0.026	0.001	17.40	-	<0.001	-
L14	BPC-4-129	7.93	1.49	0.080	0.002	1.76	0.107	0.028	15.00	0.0045	<0.001	-
L15	BPC-4-126	8.00	1.82	0.010	0.013	1.07	0.020	0.085	17.80	0.0110	<0.001	-
C16	PNL-SS-14	12.90	0.38	0.014	0.002	1.66	0.020	0.011	16.92	-	<0.001	-
L17	BPC-4-128	8.00	0.66	0.090	0.009	0.48	0.061	0.078	15.30	0.0092	<0.001	-
L18	BPC-4-98	8.13	0.14	0.016	0.033	1.13	0.080	0.001	18.00	-	<0.001	-
C19	DAN-74827	8.08	0.45	0.031	0.003	0.99	0.060	0.070	18.21	-	<0.001	-
L20	BPC-4-101	8.91	0.017	0.010	0.004	0.41	0.002	0.002	18.10	-	<0.001	-
C21[b]	DAN-12455	10.24	0.51	0.034	0.001	1.19	0.060	0.020	16.28	-	<0.001	Mo 2.08
L22[c]	BPC-4-100	13.30	0.024	0.015	0.004	0.40	0.003	0.001	16.10	-	<0.001	Mo 2.04
L23[d]	BPC-4-114	12.04	0.68	0.030	0.047	0.96	0.043	0.092	17.30	0.0093	<0.001	Nb 1.06
L24[e]	BPC-4-105	12.30	0.03	0.007	0.005	0.48	0.031	0.002	16.90	0.0129	<0.001	Nb 1.72
L25C3	BPC-4-133	8.93	0.92	0.020	0.008	1.54	0.019	0.095	17.20	0.0085	0.010	-
L26C19	BPC-4-131	8.09	0.79	0.004	0.002	0.91	0.070	0.089	17.20	0.0080	<0.001	-
L27C21	BPC-4-132	10.30	0.96	0.040	0.002	0.97	0.057	0.019	15.30	0.0058	0.030	Mo 2.01

[a]First letters "C" and "L" denote commercial and laboratory heats, respectively.
[b]Commercial-purity Type 316 SS.
[c]High-purity Type 316 SS.
[d]Commercial-purity Type 348 SS.
[e]High-purity Type 348 SS.

Specimen Irradiation

A total of 96 SSRT and 24 CT specimens were encapsulated into six capsules, each capsule containing 16 SSRT and 4 CT specimens. A fixed 0.5-mm gap was allowed between the inner wall of the Type 304 SS capsule and specimen edges. The gap was filled with research-grade He. The gap size of 0.5 mm was selected to maintain specimen temperature at 288°C during irradiation in He. To prevent capsule wall creepdown and possible changes in gap size, spacers in the form of Type 304 SS wires (0.5-mm diameter) were placed between the specimens and the capsule inner wall. Type 304 SS filler bodies were inserted on both sides of

the SSRT specimen stack to avoid overheating the thin gauge section. The six capsules were irradiated in the Halden boiling heavy water reactor starting April 8, 1992. Fast neutron (E > 1 MeV) flux during the various irradiation cycles ranged from 1.80 x 10^{13} n cm^{-2} s^{-1} to 3.31 x 10^{13} n cm^{-2} s^{-1}. Irradiation history of the six capsules is summarized in Table 3.

Table 3. Summary of discharge fluence of model austenitic stainless steel alloys irradiated in Halden Reactor

Capsule ID	Fluence Level	Target Fluence[a] (10^{21} n cm^{-2})	Irradiation Cycle	Discharge Date	Target Fluence (10^{21} n cm^{-2})
1	Medium	1.0	IFA 530-3 to -6; D-07-004-2	Nov. 96	0.9
4	Low	0.4	IFA 530-3	Oct. 92	0.3
5	High	2.5	IFA 530-4 to -6; D-07-004-1 to-3	Nov. 99	2.0
6	High	2.5	IFA 530-4 to -6; D-07-004-1 to-3	Nov. 99	2.0
7	Medium	1.0	IFA 530-4 to -6; D-07-004-1	May 96	0.9
8	High	2.5	IFA 530-4 to -6; D-07-004-1 to-3	Nov. 99	2.0

[a]For neutron energy E >1 MeV.

3.2.2 Slow-Strain-Rate Tensile Test and Fractographic Analysis of Medium-Fluence Specimens

Procedure for SSRT Test

All SSRT tests were conducted in a low-activity-level hot cell in simulated BWR-like water at 289°C. Dissolved oxygen (DO) in the water was maintained at ≈8 ppm. Conductivity and pH of the water were kept at ≈0.07-0.10 and 6.3-6.8, respectively. Strain rate was held constant at 1.65 x 10^{-7} s^{-1}. Electrochemical potential (ECP) was measured on the effluent side at regular intervals. Results of slow-strain-rate tensile tests and fractographic analysis, completed for the 16 alloys that were irradiated to a fluence of ≈0.3 x 10^{21} n·cm^{-2} (E > 1 MeV), have been reported in Ref. 79. In this reporting period, tests were completed on 23 medium-fluence alloy specimens irradiated to ≈0.9 x 10^{21} n·cm^{-2} (E > 1 MeV). In addition to the irradiated specimens, unirradiated control specimens were tested under the same conditions.

Tabulation of Results of SSRT Test and Fractographic Analysis

Results obtained to date on specimens irradiated to fluences of zero, ≈0.3 x 10^{21} n·cm^{-2} (E > 1 MeV), and ≈0.9 x 10^{21} n·cm^{-2} are tabulated in Tables 4–9. Feedwater chemistry (i.e., DO, ECP, conductivity, and pH) and results from SSRT testing (i.e., 0.2%-offset yield strength, maximum strength, uniform plastic strain, and total plastic strain) are summarized in Tables 3, 5, and 7, respectively, for nonirradiated control specimens and specimens irradiated to ≈0.3 x 10^{21} n·cm^{-2} (E > 1 MeV) and ≈0.9 x 10^{21} n·cm^{-2}. Also shown in these tables are results of SEM fractographic analysis of the failure mode (i.e., ductile, intergranular, and transgranular fracture surface morphology) of the specimens. In Table 5, the results of SSRT and SEM fractographic analysis (percent IGSCC, percent TGSCC, and combined percent IGSCC+TGSCC) are correlated with compositional characteristics of the unirradiated specimens. Similar correlations for alloys irradiated to ≈0.3 x 10^{21} n·cm^{-2} (E > 1 MeV) and ≈0.9 x 10^{21} n·cm^{-2} are given in Tables 7 and 9, respectively.

Table 4. Results of SSRT[a] tests and SEM fractography for nonirradiated control specimens of model austenitic stainless steel alloys

Alloy & Spec. Ident. No.	SSRT No.	Feedwater Chemistry: Oxygen Conc. (ppm)	Average ECP (mV SHE)	Cond. at 25°C ($\mu S \cdot cm^{-1}$)	pH at 25°C	SSRT Parameters: Yield Stress (MPa)	Max. Stress (MPa)	Uniform Elong. (%)	Total Elong. (%)	Fracture Behavior: TGSCC[b] (%)	IGSCC (%)	TGSCC + IGSCC (%)
L23-4	CHR-1	8.6	+228	0.07	6.65	332	480	15.6	17.0	15	0	15
L7-4	CHR-2	8.0	+217	0.07	7.37	195	370	2.5	5.2	20	0	20
L7-B1	CHR-7		Tested in Air			282	676	42.3	43.9	0	0	0
L14-4	CHR-3	8.6	+208	0.07	7.37	240	474	41.8	44.2	0	0	0
L17-4	CHR-4	7.5	+262	0.06	7.09	189	412	11.6	13.3	60	0	60
L17-B1	CHR-19	7.8	+166	0.08	6.71	184	447	30.1	31.2	8	0	8
L6-4	CHR-5	7.9	+256	0.08	6.85	227	545	43.0	44.5	0	0	0
L27-4	CHR-6	9.3	+247	0.08	6.96	298	483	20.6	22.9	0	0	0
L26-4	CHR-8	9.4	+223	0.07	6.65	184	596	38.2	40.2	0	0	0
L2-4	CHR-9	8.6	+292	0.06	6.55	193	348	6.6	7.8	57	0	57
L25-4	CHR-10	8.2	+239	0.06	6.42	184	458	25.5	27.0	0	0	0
L15-4	CHR-11	8.2	+195	0.06	6.32	218	512	36.7	37.9	0	0	0
L24-4	CHR-12	8.4	+200	0.07	6.20	352	461	10.4	12.3	10	0	10
C1-15	CHR-13	8.1	+187	0.07	6.33	179	498	49.4	51.7	0	0	0
C19-B1	CHR-14	8.8	+179	0.08	6.29	178	501	47.4	49.2	0	0	0
C9-B1	CHR-15	8.5	+166	0.07	6.83	178	408	17.4	19.4	32	0	32
C12-B1	CHR-16	8.5	+124	0.07	6.18	182	511	46.0	47.6	0	0	0
C10-B1	CHR-17	9.2	+145	0.07	6.26	174	478	30.6	35.1	0	0	0
C21-9	CHR-18	9.2	+187	0.07	6.41	277	455	48.9	59.5	0	0	0

[a]Tested at 289°C at strain rate of $1.65 \times 10^{-7} s^{-1}$ in simulated BWR water containing ≈8 ppm DO.

Table 5. Compositional characteristics (composition in wt.%) of nonirradiated control specimens of model austenitic stainless steel alloys correlated with results of SSRT[a] tests and SEM fractography (HP = high purity, CP = commercial purity)

Alloy ID	Ni	Si	P	S	Mn	C	N	Cr	Mo/Nb	O wppm)	Remark[b]	YS (MPa)	UTS (MPa)	UE (%)	TE (%)	TGSCC (%)	IGSCC (%)	TG+IG SCC (%)
L23	12.04	0.68	0.030	0.047	0.96	0.043	0.092	17.30	Nb 1.06	93	CP 348	332	480	15.6	17.0	15	0	15
L7	10.60	0.18	0.040	0.038	1.02	0.007	0.111	15.40	-	274	High N, O; Low Si, C	195	370	2.5	5.2	20	0	20
L14	7.93	1.49	0.080	0.002	1.76	0.107	0.028	15.00	-	45	High Si, P, C; Low S	240	474	41.8	44.2	0	0	0
L17	8.00	0.66	0.090	0.009	0.48	0.061	0.078	15.30	-	90	High P; Low Cr, Mn, S	189	412	11.6	13.3	60	0	60
L17	8.00	0.66	0.090	0.009	0.48	0.061	0.078	15.30	-	90	High P; Low Cr, Mn, S	184	447	30.1	31.2	8	0	8
L6	10.00	1.90	0.020	0.005	1.13	0.096	0.087	17.10	-	58	High Si, C, Cr; Low S	227	515	43.0	44.5	0	0	0
L27	10.30	0.96	0.040	0.002	0.97	0.057	0.019	15.30	Mo 2.01	-	CP 316 ; high B (0.030)	298	483	20.6	22.9	0	0	0
L26	8.09	0.79	0.004	0.002	0.91	0.070	0.089	17.20	-	80	Low P, S	184	506	38.2	40.2	0	0	0
L2	10.50	0.82	0.080	0.034	1.58	0.074	0.102	17.02	-	66	High P, S, Mn, N	193	348	6.6	7.8	57	0	57
L25	8.93	0.92	0.020	0.008	1.54	0.019	0.095	17.20	-	85	high B (0.010)	184	458	25.5	27.0	0	0	0
L15	8.00	1.82	0.010	0.013	1.07	0.020	0.085	17.80	-	110	High N; Low C	218	512	36.7	37.9	0	0	0
L24	12.30	0.03	0.007	0.005	0.48	0.031	0.002	16.90	Nb 1.72	-	HP 348; Low Si, N	352	461	10.4	12.3	10	0	10
C1	8.12	0.50	0.038	0.002	1.00	0.060	0.060	18.11	-	-	Low S, CP 304	179	498	49.4	51.7	0	0	0
C19	8.08	0.45	0.031	0.003	0.99	0.060	0.070	18.21	-	-	Low Si, S, CP 304	178	501	47.4	49.2	0	0	0
C9	8.75	0.39	0.013	0.013	1.72	0.062	0.065	18.48	-	-	Low Si, High Mn	178	408	17.4	19.4	32	0	32
C12	8.23	0.47	0.018	0.002	1.00	0.060	0.070	18.43	-	-	Low Si, S, P	182	511	46.0	47.6	0	0	0
C10	8.13	0.55	0.033	0.002	1.00	0.060	0.086	18.19	-	-	Low S, high N	174	478	30.6	35.1	0	0	0
C21	10.24	0.51	0.034	0.001	1.19	0.060	0.020	16.28	Mo 2.08	-	CP 316; low B (0.001)	277	455	48.9	59.5	0	0	0

[a]Test at 289°C at a strain rate of $1.65 \times 10^{-7} s^{-1}$ in simulated BWR water that contained ≈8 ppm DO.
[b]HP = high purity, CP = commercial purity.

Table 6. Results of SSRT[a] test and SEM fractography for model austenitic stainless steels irradiated in He at 289°C to fluence of ≈0.3 x 10^{21} n·cm^{-2} (E > 1 MeV)

Alloy & Spec. Ident. No.	SSRT No.	Feedwater Chemistry: Oxygen Conc. (ppm)	Average ECP (mV SHE)	Cond. at 25°C (μS·cm^{-1})	pH at 25°C	SSRT Parameters: Yield Stress (MPa)	Max. Stress (MPa)	Uniform Elongation (%)	Total Elongation (%)	Fracture Behavior: TGSCC (%)	IGSCC (%)	TGSCC IGSCC (%)
C1-1	HR-1	8.3	+184	0.07	7.03	490	680	13.4	16.6	4	0	4
L5-1	HR-2	9.7	+208	0.07	6.89	413	539	29.5	32.7	2	2	4
L22-1	HR-3	8.0	+236	0.07	6.80	360	596	6.6	9.4	50	15	65
C3-1	HR-4	8.7	+161	0.07	6.68	338	491	27.7	31.6	5	0	5
C16-1	HR-5	8.3	+204	0.08	6.74	370	527	17.6	20.6	2	0	2
L4-1	HR-6	9.0	+202	0.08	6.70	367	542	19.7	22.3	46	0	46
L18-1	HR-7	9.0	+203	0.08	6.33	503	572	6.3	8.8	54	0	54
C10-1	HR-8	8.2	+174	0.07	6.35	523	640	17.4	18.9	6	0	6
C21-1	HR-9	8.1	+149	0.08	6.49	480	620	15.9	19.4	4	0	4
L11-1	HR-10	9.0	+157	0.08	6.17	487	599	2.3	3.8	62	0	62
L13-1	HR-11	8.7	+164	0.08	6.17	248	461	22.1	24.8	8	0	8
L20-1	HR-12	8.4	+174	0.07	6.20	454	552	2.9	5.1	32	2	34
C19-1	HR-13	9.5	+132	0.12	6.36	554	682	10.5	14.7	7	0	7
C9-1	HR-14	8.0	+192	0.11	6.30	522	607	13.4	14.6	24	0	24
C12-1	HR-15	9.0	+195	0.08	6.40	404	589	20.4	24.2	5	0	5
L8-1	HR-16	9.0	+215	0.08	6.60	411	571	15.6	17.9	54	0	54

[a]Test at 289°C at a strain rate of 1.65 x 10^{-7} s^{-1} in simulated BWR water that contained ≈8 ppm DO.

Table 7. Compositional characteristics (composition in wt.%) of model austenitic stainless steels irradiated to fluence of ≈0.3 x 10^{21} n·cm^{-2} (E > 1 MeV) correlated with results of SSRT[a] tests and SEM fractography (HP = high purity, CP = commercial purity)

Alloy ID	Ni	Si	P	S	Mn	C	N	Cr	Mo/Nb	Remark[b]	YS (MPa)	UTS (MPa)	UE (%)	TE (%)	TGSCC (%)	IGSCC (%)	TG+IG SCC (%)
C1	8.12	0.50	0.038	0.002	1.00	0.060	0.060	18.11	-	Low S, CP 304	490	680	13.4	16.6	4	0	4
L5	9.66	0.90	0.113	0.028	0.47	0.006	0.033	21.00	-	High P, Cr; Low C	413	539	29.5	32.7	2	2	4
L22	13.30	0.024	0.015	0.004	0.40	0.003	0.001	16.10	Mo 2.04	HP 316L, low Si, N	360	596	6.6	9.4	50	15	65
C3	8.91	0.46	0.019	0.004	1.81	0.016	0.083	18.55	-	CP 304L, Low Si	338	491	27.7	31.6	5	0	5
C16	12.90	0.38	0.014	0.002	1.66	0.020	0.011	16.92	-	High Ni; Low Si, S	370	527	17.6	20.6	2	0	2
L4	10.20	0.94	0.031	0.010	1.75	0.110	0.002	15.80	-	High Ni, Mn, C; Low N	367	542	19.7	22.3	38	0	38
L18	8.13	0.14	0.016	0.033	1.13	0.080	0.001	18.00	-	Low Si, N	503	572	6.3	8.8	54	0	54
C10	8.13	0.55	0.033	0.002	1.00	0.060	0.086	18.19	-	Low S, CP 304	523	640	17.4	18.9	6	0	6
C21	10.24	0.51	0.034	0.001	1.19	0.060	0.020	16.28	Mo 2.08	CP 316	480	620	15.9	19.4	4	0	4
L11	8.15	0.47	0.097	0.009	1.02	0.014	0.004	17.40	-	High P; Low Si, C, S, N	487	599	2.3	3.8	62	0	62
L13	8.18	1.18	0.027	0.022	0.36	0.026	0.001	17.40	-	High Si; Low Mn, C, N	248	461	22.1	24.8	8	0	8
L20	8.91	0.017	0.010	0.004	0.41	0.002	0.002	18.10	O 0.0940	highO; low Si, N; HP 304L	454	552	2.9	5.1	32	2	34
C19	8.08	0.45	0.031	0.003	0.99	0.060	0.070	18.21	-	Low Si, S	554	682	10.5	14.7	7	0	7
C9	8.75	0.39	0.013	0.013	1.72	0.062	0.065	18.48	-	Low Si; High Mn	522	607	13.4	14.6	24	0	24
C12	8.23	0.47	0.018	0.002	1.00	0.060	0.070	18.43	-	Low Si, P, S	404	589	20.4	24.2	5	0	5
L8	10.20	0.15	0.093	0.010	1.85	0.041	0.001	18.30	-	High Ni, P, Mn; Low Si, N	411	571	15.6	17.8	64	0	64

[a]Test at 289°C at a strain rate of 1.65 x 10^{-7} s^{-1} in BWR-simulated water; DO ≈8 ppm, effluent ECP +140 to +236 mV SHE, conductivity at 25°C 0.07-0.11 μS cm^{-1}, and pH 6.2-7.0.

[b]HP = high purity, CP = commercial purity.

Table 8. Results of SSRT[a] tests and SEM fractography for model austenitic stainless steels irradiated in He at 289°C to fluence of ≈0.9 x 10^{21} n·cm^{-2} (E > 1 MeV)

Alloy & Spec. Ident. No.	SSRT No.	Feedwater Chemistry: Oxygen Conc. (ppm)	Average ECP (mV SHE)	Cond. at 25°C (μS·cm^{-1})	pH at 25°C	SSRT Parameters: Yield Stress (MPa)	Max. Stress (MPa)	Uniform Elongation (%)	Total Elongation (%)	Fracture Behavior: TGSCC (%)	IGSCC (%)	TGSCC IGSCC (%)
L22-02	HR-17	8.0	+181	0.08	6.77	475	549	4.20	5.82	30	35	65
L11-02	HR-18	8.0	+191	0.08	6.55	820	856	0.43	1.65	50	14	64
L18-02	HR-19	8.0	+193	0.10	6.07	710	755	3.98	5.05	38	14	52
L20-02	HR-28	Test in 289°C Air				826	845	0.31	2.09	0	0	0
L20-05	HR-26	9.0	+182	0.09	6.32	670	743	0.37	1.03	0	0	0
L20-06	HR-27	8.0	+274	0.07	6.05	632	697	0.85	2.72	0	0	0
C9-02	HR-21	8.0	+240	0.07	6.47	651	679	1.42	2.50	62	22	84
L17-02	HR-22	8.0	+198	0.07	6.42	574	654	2.02	3.08	44	41	85
L7-02	HR-23	8.0	+215	0.07	6.03	553	561	0.24	2.44	38	54	92
C10-02	HR-24	7.0	+221	0.07	5.26	651	706	6.35	9.25	14	0	14
C3-02	HR-25	8.0	+240	0.07	6.34	632	668	16.72	19.74	9	4	13
C19-02	HR-30	Test in 289°C Air				888	894	6.41	10.21	1	0	1
C19-04	HR-31	8.0	+252	0.07	6.18	750	769	6.06	8.79	1	0	1
L6-02	HR-32	8.0	+250	0.07	6.40	493	546	2.45	3.77	8	27	35
L14-02	HR-33	8.0	+246	0.08	6.07	649	684	1.90	4.67	84	2	86
L13-02	HR-34	7.0	+222	0.09	6.85	602	624	1.67	4.95	55	2	57
L04-02	HR-35	7.0	+259	0.08	6.54	634	680	1.07	2.02	68	2	70
L05-02	HR-36	7.0	+243	0.07	6.85	665	725	3.07	4.57	3	5	8
C16-02	HR-37	7.0	+230	0.07	6.62	562	618	11.99	15.80	7	1	8
L8-02	HR-38	8.0	+242	0.07	6.57	838	838	0.12	3.12	15	22	37
C21-02	HR-39	8.0	+231	0.08	6.21	643	716	15.38	18.30	1	2	3
L2-02	HR-40	7.0	+239	0.07	7.11	839	849	0.88	1.56	38	4	42
L24-02	HR-41	8.0	+239	0.06	6.40	725	725	0.15	2.45	2	1	3
L23-02	HR-42	7.0	+237	0.08	6.60	787	818	0.38	1.24	3	24	27
C12-02	HR-43	7.0	+227	0.07	6.19	747	756	14.96	18.57	4	0	4
C1-02	HR-44	8.0	+229	0.07	6.30	707	763	13.36	17.04	2	0	2

[a]Test at 289°C at a strain rate of 1.65 x 10^{-7} s^{-1} in simulated BWR water that contained ≈8 ppm DO.

Alloy-to-Alloy Variation in Stress Corrosion Behavior at Medium Fluence

When compared with the properties of the unirradiated and low-fluence specimens, the effects of the increased fluence on yield strength, ultimate tensile strength, uniform elongation, total elongation, and fracture behavior of the medium-fluence specimens were significant. For example, the effects of fluence and test environment (i.e., air vs. water) on load elongation behavior are shown in Fig. 10 for Heat C19, a commercially purchased heat of Type 304 SS. For this commercial alloy, a significant effect of fluence on load-elongation behavior in water is evident as fluence increases from 0 to ≈0.3 x 10^{21} n·cm^{-2} and ≈0.9 x 10^{21} n·cm^{-2}. A similar effect of fluence was significantly more pronounced in most laboratory alloys than in commercial alloys. The results obtained from the SSRT tests and SEM fractography of the medium-fluence specimens, i.e., yield strength, ultimate tensile strength, uniform elongation, total elongation, percent TGSCC, percent IGSCC, and percent TGSCC+IGSCC, are plotted for each alloy in Figs. 11–17, respectively.

Table 9. Compositional characteristics (composition in wt.%) of model austenitic stainless steels irradiated to fluence of ≈0.9 x 10^{21} n·cm^{-2} (E > 1 MeV) correlated with results of SSRT[a] tests and SEM fractography (HP = high purity, CP = commercial purity)

Alloy ID	Ni	Si	P	S	Mn	C	N	Cr	Mo/Nb	Remark[b]	YS (MPa)	UTS (MPa)	UE (%)	TE (%)	TGSCC (%)	IGSCC (%)	TG+IG SCC (%
L22-02	13.30	0.024	0.015	0.004	0.40	0.003	0.001	16.10	Mo 2.04	HP 316L; low Si, N, S	475	549	4.20	5.82	30	35	65
L11-02	8.15	0.47	0.097	0.009	1.02	0.014	0.004	17.40	-	high P; low Si, C, S, N	820	856	0.43	1.65	50	14	64
L18-02	8.13	0.14	0.016	0.033	1.13	0.080	0.001	18.00	-	low Si, N	710	755	3.98	5.05	38	14	52
L20-05	8.91	0.017	0.010	0.004	0.41	0.002	0.002	18.10	O 0.0940	high O; low Si, N; HP 304L	670	743	0.37	1.03			
L20-06	8.91	0.017	0.010	0.004	0.41	0.002	0.002	18.10	O 0.0940	highO; low Si, N; HP 304L	632	697	0.85	2.72			
C9-02	8.75	0.39	0.013	0.013	1.72	0.062	0.065	18.48	-	low Si; high Mn	651	679	1.42	2.50	62	22	84
L17-02	8.00	0.66	0.090	0.009	0.48	0.061	0.078	15.30	O 0.0090	high P; low Cr, Mn, S	574	654	2.02	3.08	44	41	85
L7-02	10.60	0.18	0.040	0.038	1.02	0.007	0.111	15.40	O 0.0274	high S, N, O; low Si, C	553	561	0.24	2.44	38	54	92
C10-02	8.13	0.55	0.033	0.002	1.00	0.060	0.086	18.19	-	CP 304; low S; high N	651	706	6.35	9.25	14	0	14
C3-02	8.91	0.46	0.019	0.004	1.81	0.016	0.083	18.55	-	CP 304L; high Mn, N; low S	632	668	16.7	19.7	9	4	13
C19-04	8.08	0.45	0.031	0.003	0.99	0.060	0.070	18.21	O 0.0200	CP 304; low S	750	769	6.06	8.79	1	0	1
L6-02	10.00	1.90	0.020	0.005	1.13	0.096	0.087	17.10	O 0.0058	high Si; low S	493	546	2.45	3.77	8	27	35
L14-02	7.93	1.49	0.080	0.002	1.76	0.107	0.028	15.00	O 0.0045	high Si, P, Mn; low Cr, S	649	684	1.90	4.67	84	2	86
L13-02	8.18	1.18	0.027	0.022	0.36	0.026	0.001	17.40	-	high Si, S; Low Mn, C, N	602	624	1.67	4.95	55	2	57
L4-02	10.20	0.94	0.031	0.010	1.75	0.110	0.002	15.80	-	high Si, C; low N, Cr	634	680	1.07	2.02	68	2	70
L5-02	9.66	0.90	0.113	0.028	0.47	0.006	0.033	21.00	-	high Si, P, Cr; Low Mn, C	665	725	3.07	4.57	3	5	8
C16-02	12.90	0.38	0.014	0.002	1.66	0.020	0.011	16.92	0.0157	high Ni; low P, S, C	562	618	12.0	15.8	7	1	8
L8-02	10.20	0.15	0.093	0.010	1.85	0.041	0.001	18.30	-	high P, Mn; low Si, N	838	838	0.12	3.12	15	22	37
C21-02	10.24	0.51	0.034	0.001	1.19	0.060	0.020	16.28	Mo 2.08	CP 316, low S	643	716	15.4	18.3	1	2	3
L2-02	10.50	0.82	0.080	0.034	1.58	0.074	0.102	17.02	O 0.0066	high O, P, S, N	839	849	0.88	1.56	38	4	42
L24-02	12.30	0.03	0.007	0.005	0.48	0.031	0.002	16.90	Nb 1.72 O 0.0129	HP 348L; low Si, P, S, C, N	725	725	0.15	2.45	2	1	3
L23-02	12.04	0.68	0.030	0.047	0.96	0.043	0.092	17.30	Nb 1.06 O 0.0093	CP 348, high S	787	818	0.38	1.24	3	24	27
C12-02	8.23	0.47	0.018	0.002	1.00	0.060	0.070	18.43	-	304, low S, low P	747	756	15.0	18.6	4	0	4
C1-02	8.12	0.50	0.038	0.002	1.00	0.060	0.060	18.11	-	304, low S	707	763	13.4	17.0	2	0	2

[a]Test at 289°C at a strain rate of 1.65 x 10^{-7} s^{-1} in BWR-simulated water; DO ≈8 ppm, effluent ECP +140 to +236 mV SHE, conductivity at 25°C 0.07-0.11 μS cm^{-1}, and pH 6.2-7.0.

[b]HP = high purity, CP = commercial purity.

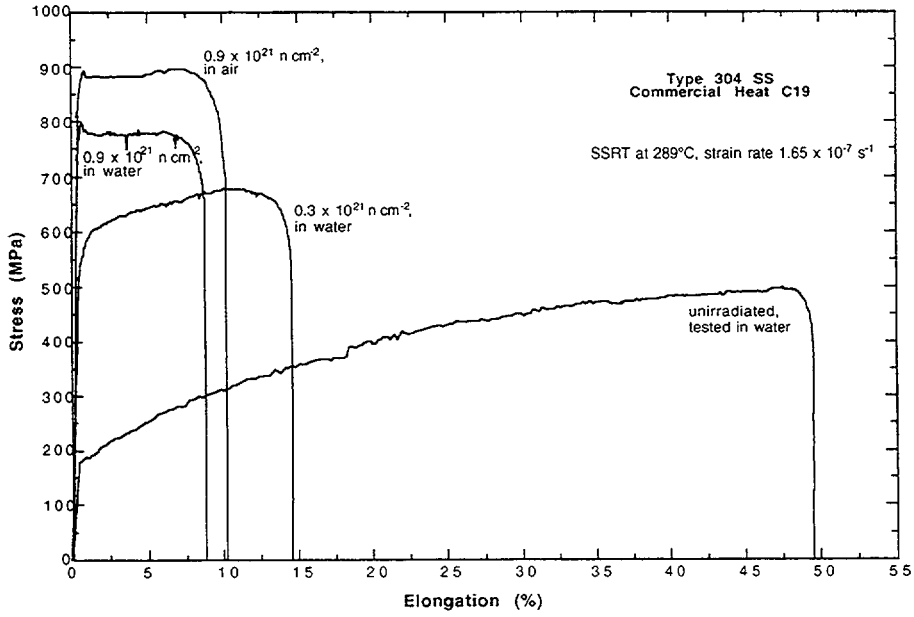

Figure 10. Effects of fluence and test environment on load elongation behavior of Type 304 SS commercial heat C19

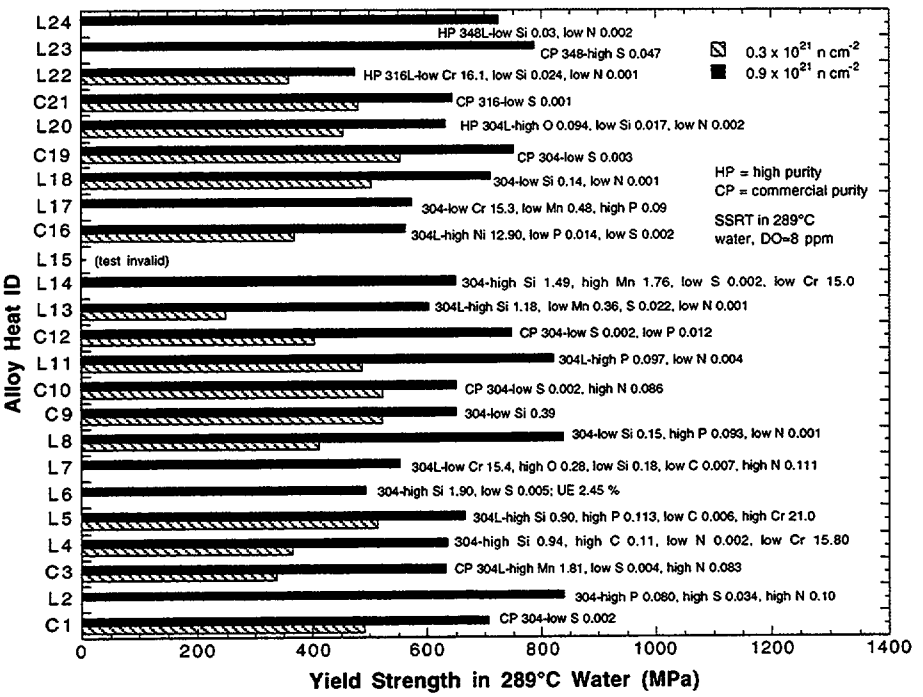

Figure 11. Effects of fluence on yield strength measured in 289°C water containing ≈8 ppm DO

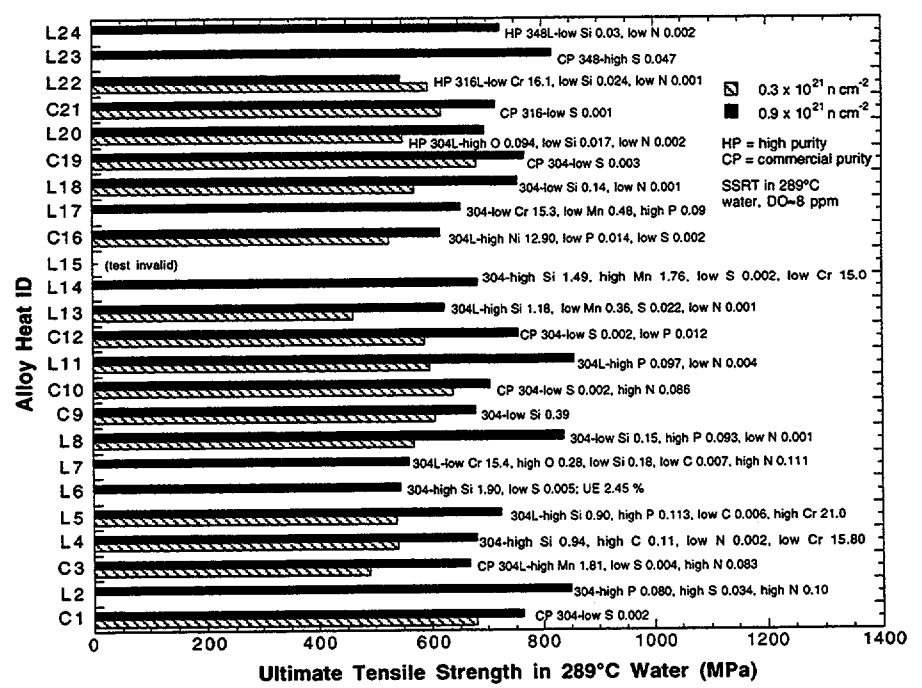

Figure 12. Effects of fluence on maximum strength measured in 289°C water containing ≈8 ppm DO

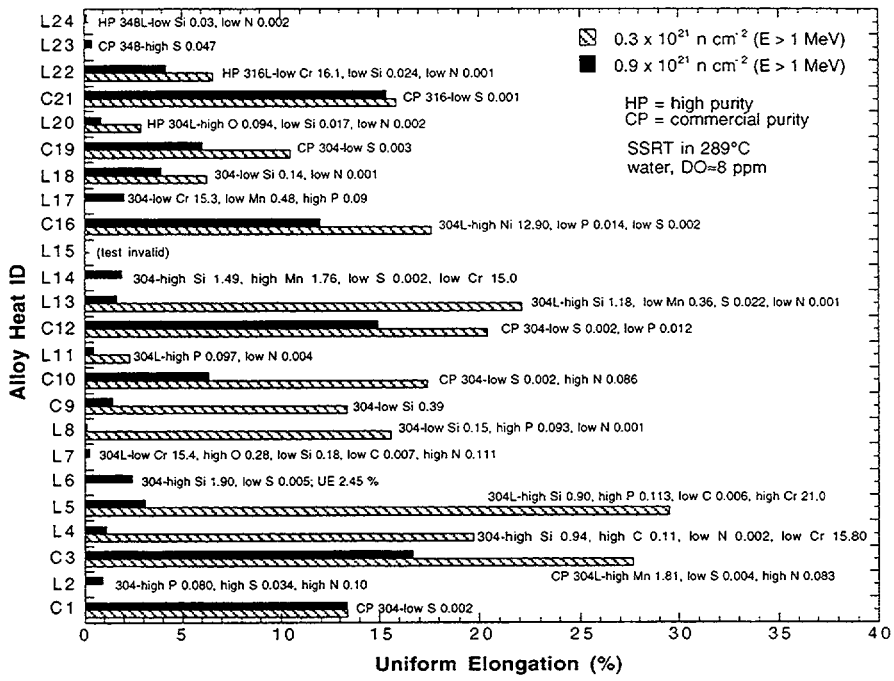

Figure 13. Effects of fluence on uniform elongation measured in 289°C water containing ≈8 ppm DO

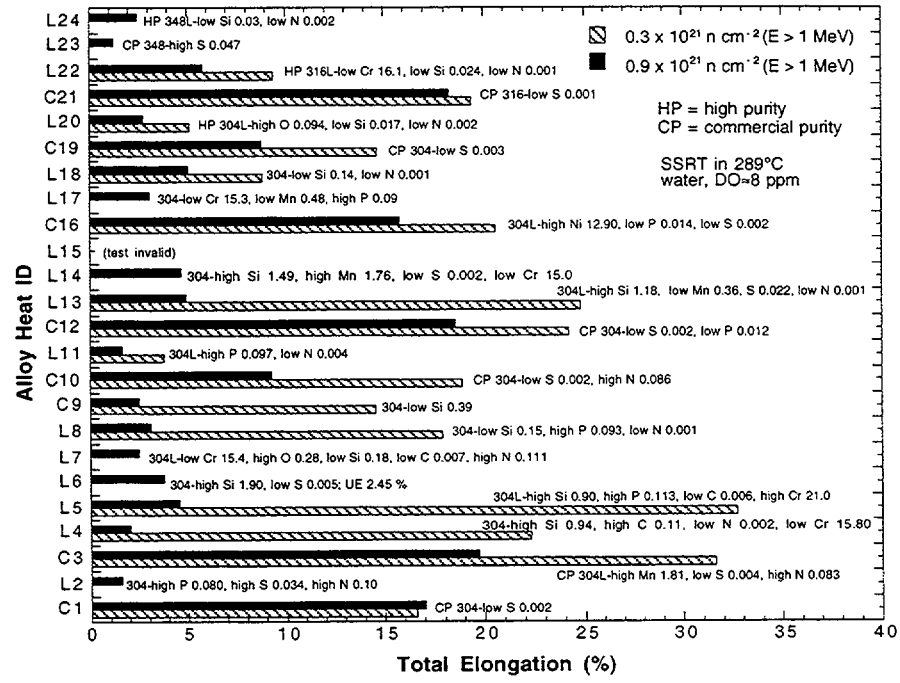

Figure 14. Effects of fluence on total elongation measured in 289°C water containing ≈8 ppm DO

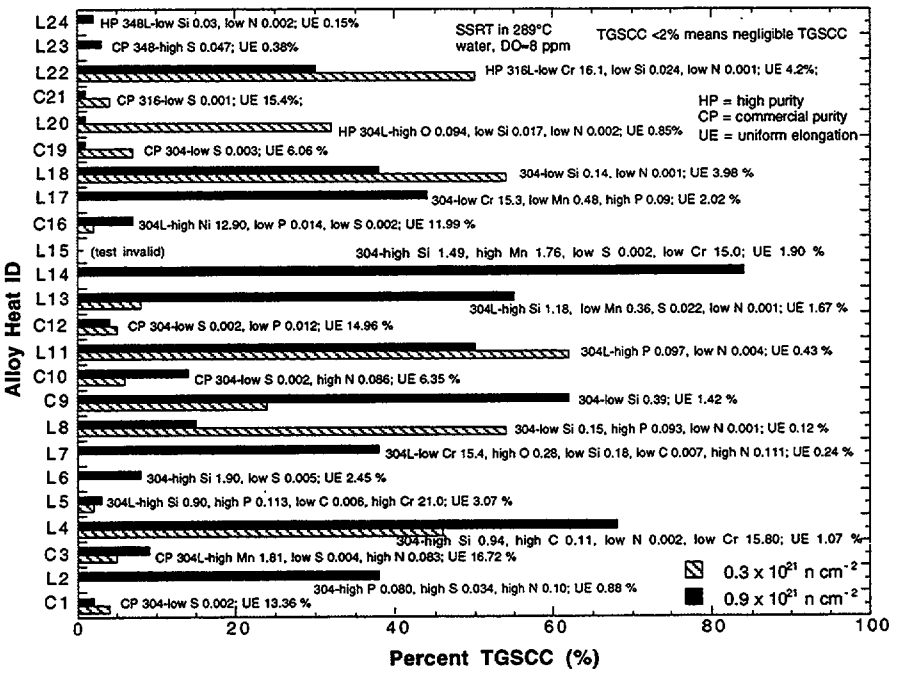

Figure 15. Effects of fluence on percent TGSCC measured in 289°C water containing ≈8 ppm DO

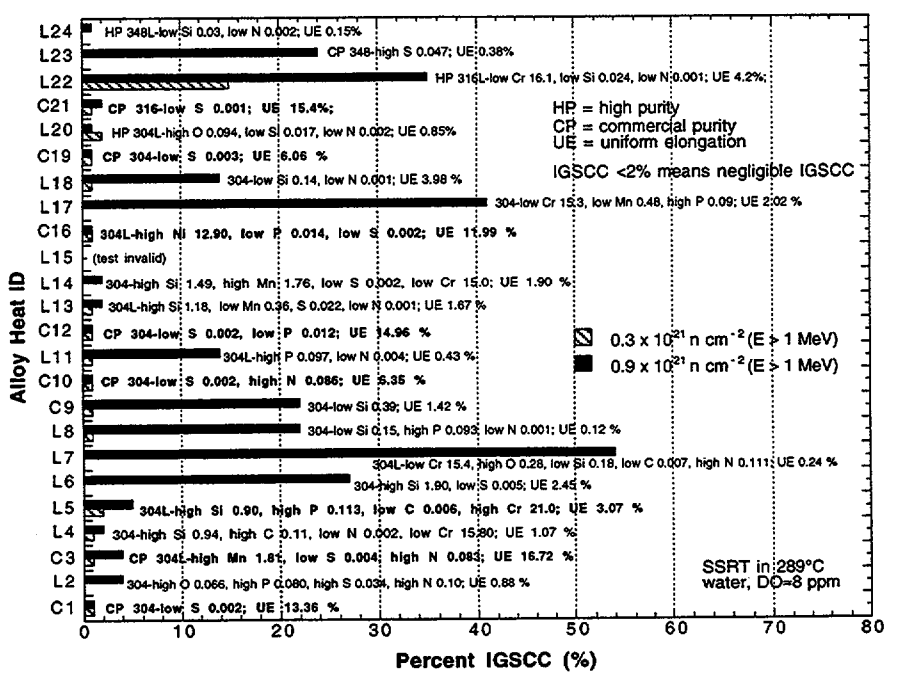

Figure 16. Effects of fluence on percent IGSCC measured in 289°C water containing ≈8 ppm DO

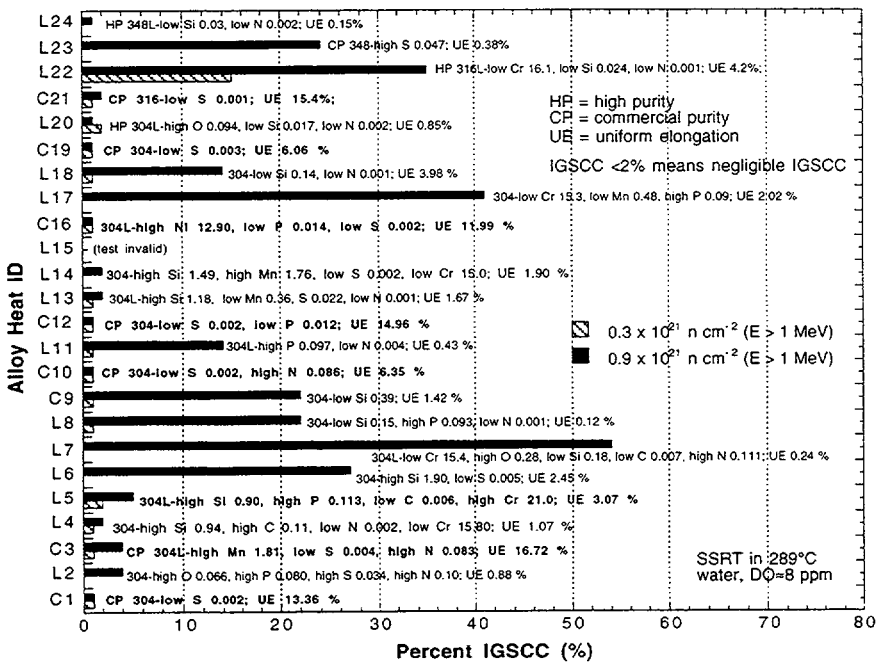

Figure 17. Effects of fluence on percent TGSCC + IGSCC measured in 289°C water containing ≈8 ppm DO

Effect of Silicon

Yield strength of the model alloys, measured in BWR-like water at 289°C, was nearly constant at ≈200 MPa in the unirradiated state and was more or less independent of Si concentration (see Fig. 18). However, as fluence was increased to ≈0.3 x 10^{21} n·cm^{-2} and ≈0.9 x 10^{21} n·cm^{-2}, the degree of increase in yield strength was significantly lower for alloys that contain >0.9 wt.% Si than for alloys that contain <0.8 wt.% Si. This finding indicates that nature of irradiation-induced hardening centers and the degree of irradiation hardening are significantly influenced by alloy Si content. Silicon atoms in austenitic stainless steels occupy substitutional sites. Therefore, Si atoms are likely to interact preferentially with irradiation-induced vacancy sites in the steel. This effect is likely to inhibit the formation of vacancy clusters or vacancy-impurity complexes, and is therefore conducive to a less significant irradiation-induced hardening. An effect similar to that of Si was, however, not observed for C and N.

Among laboratory heats of Types 304 and 304L SS, alloys that contain <0.67 wt.% Si exhibited significant susceptibility to IGSCC, whereas alloys with 0.8–1.5 wt.% Si exhibited negligible susceptibility to IGSCC (see Fig. 19). However, an alloy with ≈1.9 wt.% Si exhibited some degree of susceptibility to IGSCC (percent IGSCC ≈ 27, see Alloy L6 in Table 9). These observations indicate that an Si concentration of ≈0.8 to ≈1.5 wt.% is beneficial in delaying the onset of or suppressing the susceptibility to IASCC. To determine if similar effects are evident at higher fluence levels would require testing of the high-fluence specimens that will be discharged after irradiation to ≈2.0 x 10^{21} n·cm^{-2} (E > 1 MeV).

Of the 23 alloys irradiated to ≈0.9 x 10^{21} n·cm^{-2}, Alloy L7 (which contains unusually low concentrations of Cr [15.4 wt.%] and Si [0.18 wt.%] and an unusually high concentration of S

[0.038 wt.%], exhibited the worst susceptibility to IASCC (i.e., ≈54% IGSCC, ≈92% TGSCC + IGSCC). Alloy L7 also contained an unusually high concentration of O (0.027 wt.%). Considering deleterious effect of O,[72,78] the unusually high concentration of O is believed to be one of the important factors that led to the poor performance of the alloy. Alloy L7 exhibited significant susceptibility to TGSCC (≈20% TGSCC) in water even in the unirradiated state (Table 5).

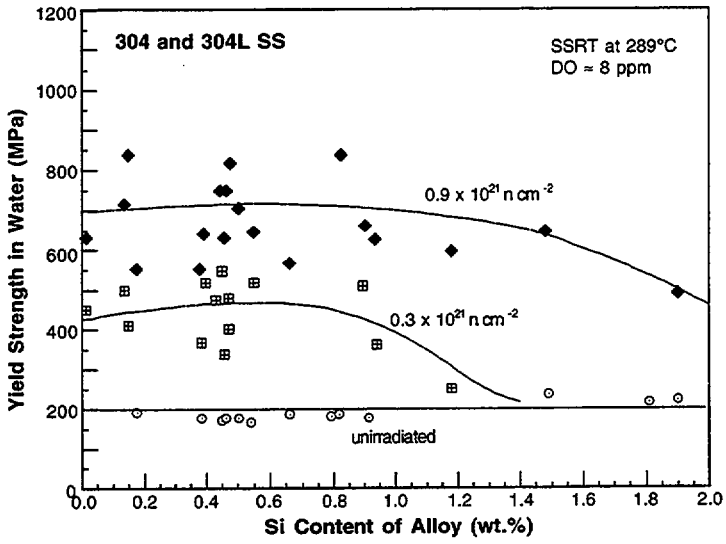

Figure 18. Effect of Si concentration on yield strength of Types 304 and 304L alloys measured in 289°C water before and after irradiation

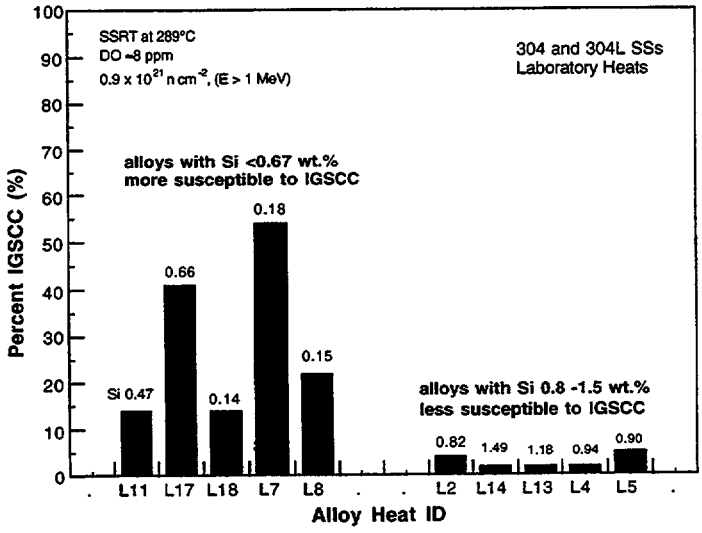

Figure 19. Effect of Si on susceptibility to IGSCC of laboratory alloys of Types 304 and 304L SS measured after irradiation to ≈0.9 x 10^{21} n·cm^{-2} (E > 1 MeV); alloys susceptible to IASCC contain relatively low concentrations of Si (<0.67 wt.%); alloys resistant to IASCC contain relatively high concentrations of Si (0.8-1.5 wt.%)

3.3 Fracture Toughness J–R Test of Austenitic Stainless Steels Irradiated in the Halden Reactor (E. E. Gruber and O. K. Chopra)

3.3.1 Introduction

Austenitic stainless steels (SSs) are used extensively as structural alloys in reactor pressure vessel internal components because of their high strength, ductility, and fracture toughness. Fracture of these steels occurs by stable tearing at stresses well above the yield stress, and tearing instabilities require extensive plastic deformation. However, exposure to neutron irradiation for extended periods changes the microstructure and degrades the fracture properties of these steels. Irradiation leads to a significant increase in yield strength and reduction in ductility and fracture resistance of austenitic SSs.[82–84]

Neutron irradiation of austenitic SSs at temperatures below 400°C leads to the formation of a substructure with very fine defects that consist of small (<5 nm) vacancy and interstitial loops or "black spots" and larger (>5 nm) faulted interstitial loops.[85–87] The latter are obstacles to dislocation motion and lead to matrix strengthening and increase in tensile strength. Also, irradiation–induced defects cause loss of ductility and reduced strain-hardening capacity of the material. The effects of radiation on various austenitic SSs vary significantly and appear to be related to minor differences in the chemical composition of the steels;[82] the chemical composition can influence the stacking fault energy and/or irradiation–induced microstructure. As the yield strength approaches ultimate strength, planar slip or dislocation channeling is promoted and leads to pronounced degradation in the fracture resistance of these steels.[84] In general, higher stacking–fault energy enhances and cold working inhibits dislocation channeling.[82]

The effect of neutron exposure on the fracture toughness J_{IC} of austenitic SSs irradiated at 350–450°C is shown in Fig. 20.[88–96] The effects of irradiation may be divided into three regimes: little or no loss of toughness below a threshold exposure of ≈1 dpa, substantial decrease in toughness at exposures of 1–10 dpa, and no further reduction in toughness above a saturation exposure of 10 dpa. The effect is largest in high–toughness steels. The degradation in fracture properties saturates at a J_{IC} value of ≈30 kJ/m^2 (or equivalent critical stress intensity factor K_{JC} of 70 MPa m$^{0.5}$). Also, the failure mode changes from dimple fracture to channel fracture.

Most of the existing fracture toughness test data have been obtained at temperatures above 350°C; fracture toughness results that are relevant to LWRs are very limited.[83] This paper presents fracture toughness J–R curves for four heats of Type 304 SS that were irradiated to fluence levels of ≈0.3 and 0.9 x 10^{21} n cm^{-2} (E > 1 MeV) (≈0.45 and 1.35 dpa) at ≈288°C in an He environment in the Halden heavy water boiling reactor. The results are compared with data obtained from irradiated reactor internal components removed from operating plants.

3.3.2 Experimental

Fracture toughness J–R curve tests were performed on 1/4–T compact tension (CT) specimens in air at 288°C according to the requirements of ASTM Specification E 1737 for "J–Integral Characterization of Fracture Toughness." Crack extensions were determined by

both DC potential and elastic unloading compliance techniques. The composition of the various heats of Type 304 SS is presented in Table 10. Figure 21 shows the configuration of the CT specimens. Crack length and J-integral were calculated with the correlations recommended for disk-shaped compact tension DC(T) specimens in ASTM Specification E 1737.

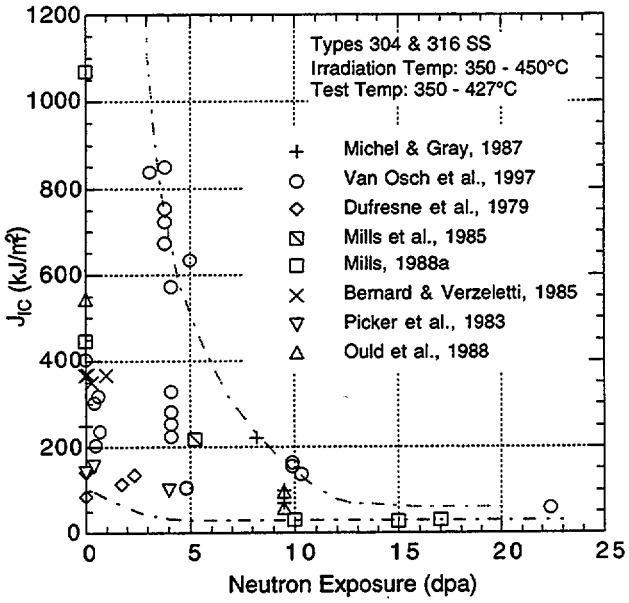

Figure 20.
Fracture toughness J_{IC} as a function of neutron exposure for austenitic Types 304 and 316 SS

Table 10. Composition (wt.%) of model Type 304 SS alloys irradiated in the Halden reactor

Alloy ID[a]	Vendor Heat ID	Analysis	Ni	Si	P	S	Mn	C	N	Cr	O[b]
L2	BPC-4-111	Vendor	10.50	0.82	0.080	0.034	1.58	0.074	0.102	17.02	66
		ANL	–	–	–	–	–	–	–	–	–
C16	PNL-SS-14	Vendor	12.90	0.38	0.014	0.002	1.66	0.020	0.011	16.92	–
		ANL	12.32	0.42	0.026	0.003	1.65	0.029	0.011	16.91	157
C19	DAN-74827	Vendor	8.08	0.45	0.031	0.003	0.99	0.060	0.070	18.21	–
		ANL	8.13	0.51	0.028	0.008	1.00	0.060	0.068	18.05	200
L20	BPC-4-101	Vendor	8.91	0.17	0.010	0.004	0.41	0.002	0.002	18.10	–
		ANL	8.88	0.10	0.020	0.005	0.47	0.009	0.036	18.06	940

[a]First letters "C" and "L" denote commercial and laboratory heats, respectively.
[b]In wppm.

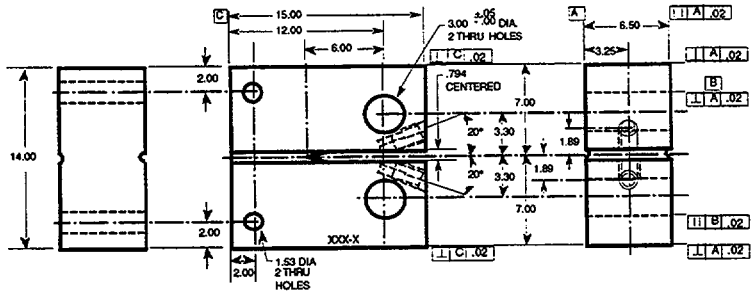

Figure 21. Configuration of compact-tension specimen for this study (dimensions in mm)

The fracture toughness test facility is designed for in-cell testing, with the hydraulic actuator, test train, furnace, and other required equipment mounted on a portable, wheeled cart that can be easily rolled into the cell. Detailed descriptions of the test facility and procedures are given in Refs. 97 and 98.

Before testing, the specimens were fatigue-precracked at room temperature. The precracked specimens were then tested at 288°C at a constant extension rate; tests were interrupted periodically to determine the crack length. Specimens were held at constant extension to measure crack length by both the DC potential drop and elastic unloading compliance techniques. For most steels, load relaxation occurs during the hold period or unloading, which causes a time-dependent nonlinearity in the unloading curve. Consequently, before unloading, the specimen was held for ≈1 min to allow load relaxation.

Specimen extension was monitored and controlled outside the high-temperature zone. The displacement of load points (center of the loading pins) was determined by subtracting the machine compliance from the measured extension. Examples of load-vs.-loadline displacement curves for irradiated Type 304 SS are shown in Fig. 22.

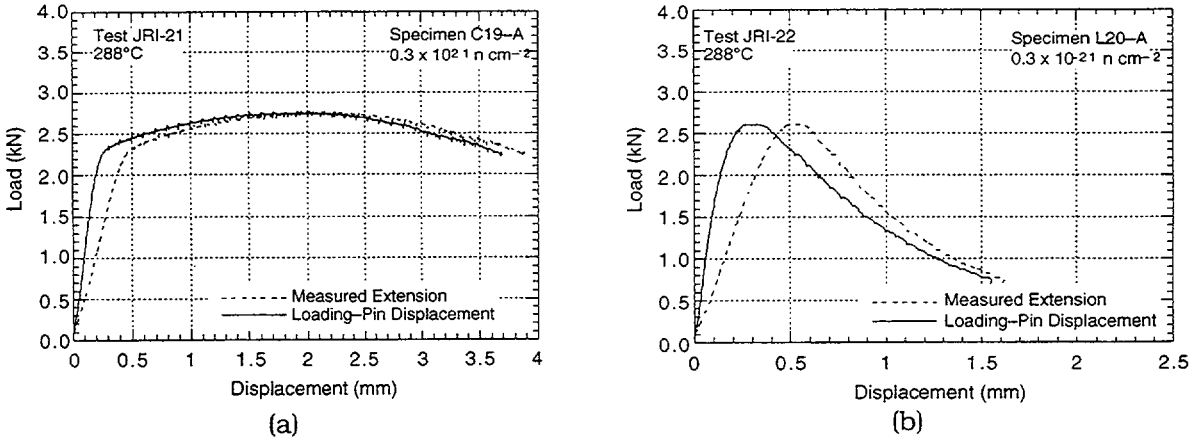

Figure 22. Examples of load-vs.-loadline displacement curves for irradiated specimens of Heats (a) C19 and (b) L20 of Type 304 SS tested at 288°C

The final crack size was marked by heat tinting and/or by fatigue cycling at room temperature. The specimens were then fractured and the initial (i.e., fatigue precrack) and final (test) crack lengths of both halves of the fractured specimen were measured optically. The crack lengths were determined by the 9/8 averaging technique, i.e., the two near-surface measurements were averaged and the resultant value was averaged with the remaining seven measurements.

The crack length measurements obtained by the elastic unloading compliance method were adjusted only with the measured initial crack length, whereas those obtained by the DC potential-drop technique were adjusted with both the initial and final crack lengths. The two-point pinning method was used to correct the measured potentials. The DC potential data were also corrected for the effects of plasticity on the measured potential, i.e., large crack-tip plasticity can increase measured potentials without crack extension because of resistivity increases. As per ASTM E 1737, the change in potential before crack initiation was ignored and the remainder of the potential change was used to establish the J-R curve. Plots of

normalized potential vs. loadline displacement generally remain linear until the onset of crack extension. For all data within the linear portion of the curve, crack extension was calculated from the blunting line relationship $\Delta a = J/(4\sigma_f)$. For high-strain-hardening materials, e.g., austenitic SSs, a slope that is four times the flow stress ($4\sigma_f$) represents the blunting line better than a slope of $2\sigma_f$, as defined in ASTM E 1737.[84]

For materials with relatively low fracture toughness, e.g., J_{IC} <300 kJ/m^2, the measurements of crack extension by the elastic unloading compliance method showed excellent agreement with those obtained by DC potential methods, whereas measurements obtained by elastic unloading compliance showed significant scatter for materials with high fracture toughness. The fracture toughness J-R curves for a relatively low- and high-fracture toughness material, obtained by the unloading compliance and DC potential methods, are shown in Figs. 23 and 24, respectively.

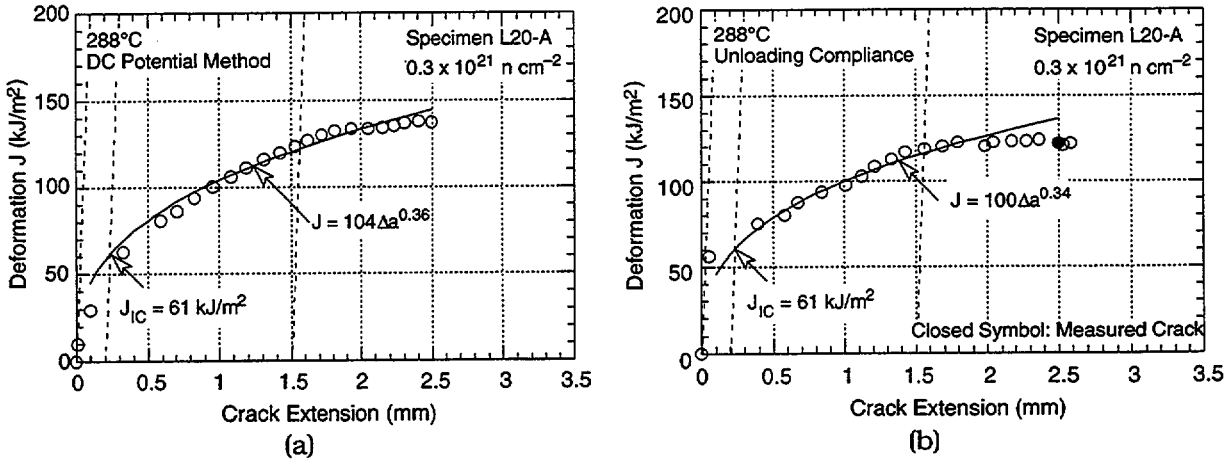

Figure 23. Fracture toughness J-R curves determined by DC (a) potential drop and (b) unloading compliance methods for Heat L20 irradiated to 0.3 x 10^{21} n·cm^{-2} (0.45 dpa) at 288°C. Dashed lines represent blunting line and 0.2- and 1.5-mm offset lines.

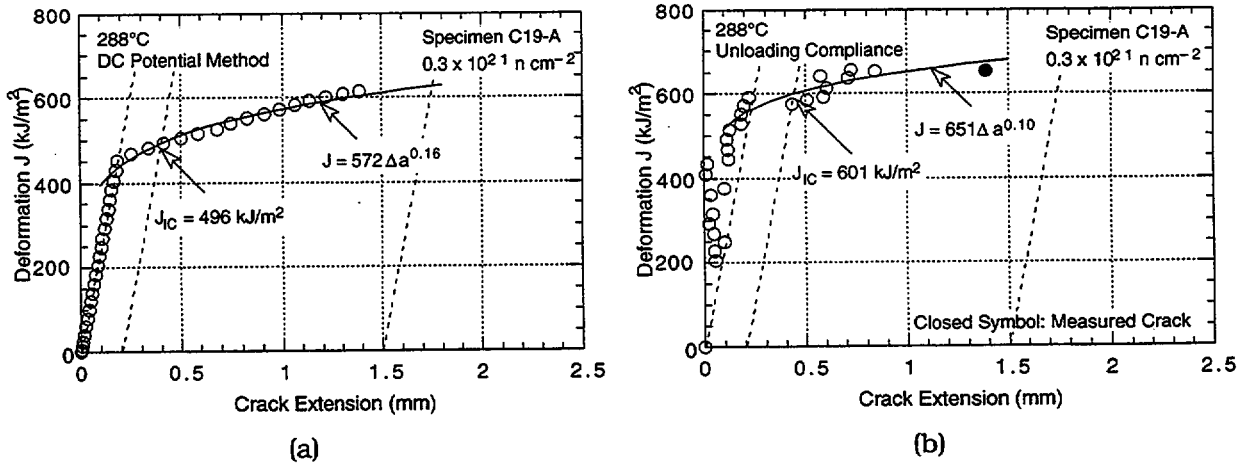

Figure 24. Fracture toughness J-R curves determined by (a) DC potential drop and (b) unloading compliance methods for Heat C19 irradiated to 0.3 x 10^{21} n·cm^{-2} (0.45 dpa) at 288°C. Dashed lines represent blunting line and 0.2- and 1.5-mm offset lines.

3.3.3 Results

Nonirradiated Type 304 Stainless Steel

The fracture toughness J–R curves for nonirradiated specimens of Heats L2, L20, C16, and C19, obtained by the DC potential method, are shown in Figs. 25–28; duplicate tests were conducted for Heats L2 and C16. The results indicate that the fracture toughness of the laboratory Heats L2 and L20 is very low. The J–R curves are significantly lower than those typically observed for Type 304 SSs, Fig. 29.[93,99-102] The J_{IC} values at temperatures up to 550°C are typically >400 kJ/m^2 for wrought austenitic SSs;[84] experimental J_{IC} for Heats L2 and L20 is ≈170 and 80 kJ/m^2, respectively. The commercial Heats C16 and C19 show very high fracture toughness. For both steels, the entire J–R curve is composed of the blunting line; fracture toughness J_{IC} could not be determined for Heat C16.

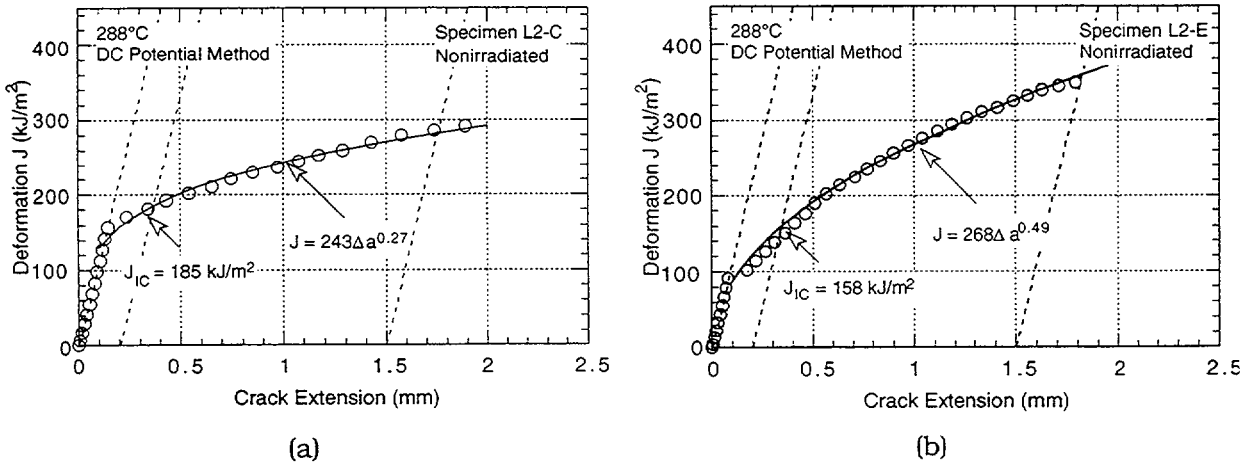

Figure 25. Fracture toughness J–R curve obtained by DC potential method for nonirradiated specimens (a) L2–C and (b) L2–E of Heat L2 of Type 304 SS at 288°C

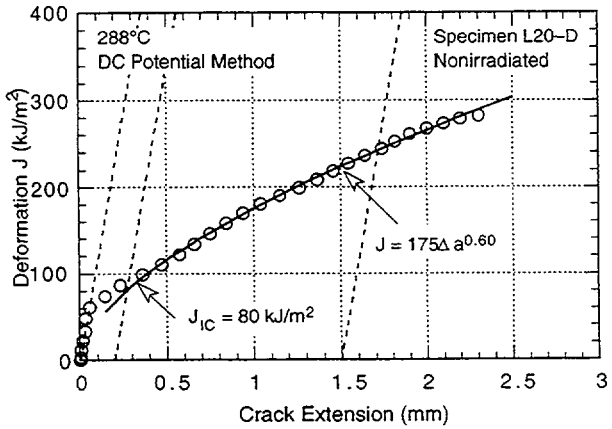

Figure 26.
Fracture toughness J–R curve obtained by DC potential method for nonirradiated specimen of Heat L20 of Type 304 SS at 288°C

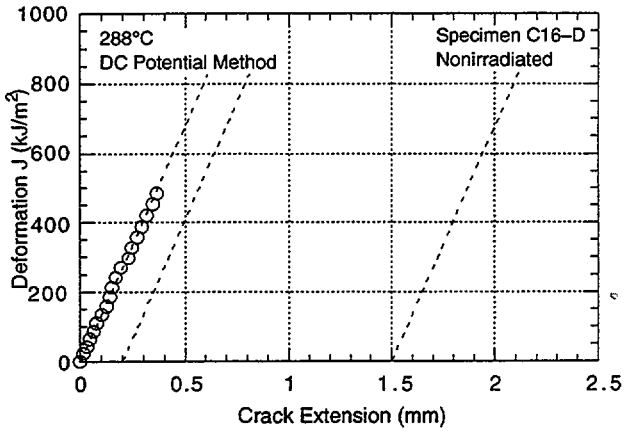

Figure 27.
Fracture toughness J–R curve obtained by DC potential method for nonirradiated specimen of Heat C16 of Type 304 SS at 288°C

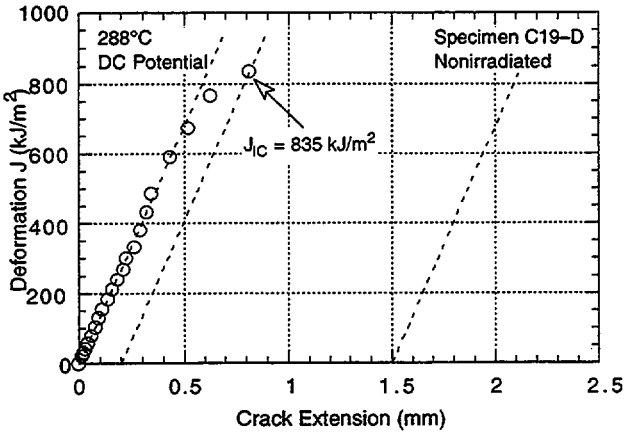

Figure 28.
Fracture toughness J–R curve obtained by DC potential method for nonirradiated specimen of Heat C19 of Type 304 SS at 288°C

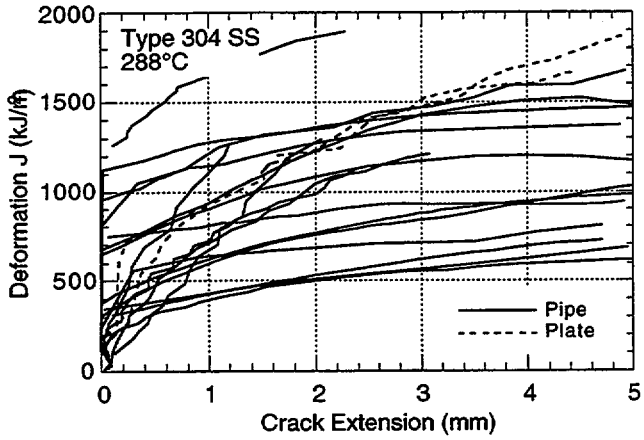

Figure 29.
Fracture toughness J–R curves for Type 304 stainless steels at 288°C

Irradiated Type 304 Stainless Steels

Fracture toughness J–R curve tests were conducted at 288°C on Heats C19, L20, C16, and L2 of Type 304 SS irradiated in helium at 288°C to 0.9 x 10^{21} n·cm^{-2} (E > 1 MeV) (1.35 dpa) in the Halden reactor. Heats C19 and L20 were also tested after a fluence of 0.3 x 10^{21} n·cm^{-2} (E > 1 MeV) (0.45 dpa). The J–R curves obtained by the DC potential method for the various steels are shown in Figs. 30–33.

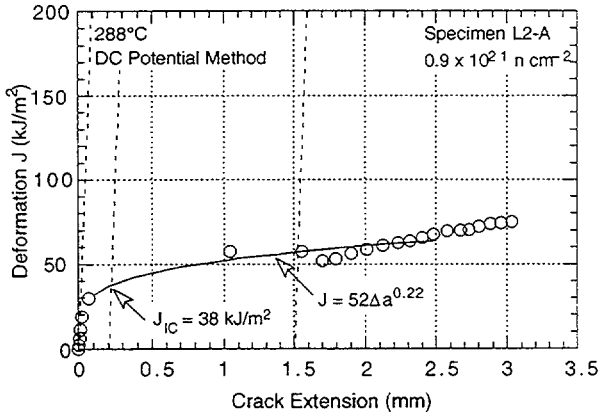

Figure 30.
Fracture toughness J–R curve at 288°C for Heat L2 irradiated to 0.9 x 10^{21} n·cm^{-2} (E > 1 Me) (1.35 dpa) at 288°C

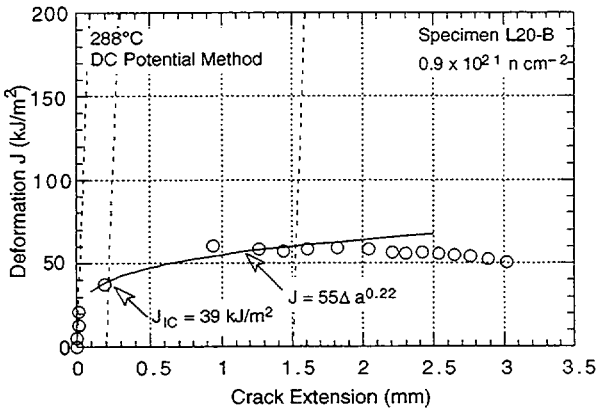

(a)

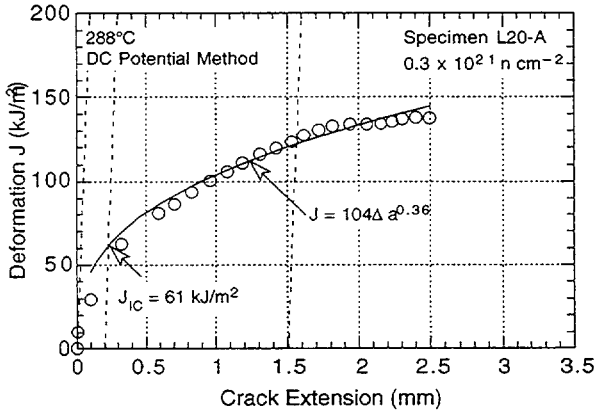

(b)

Figure 31. Fracture toughness J–R curves at 288°C for Heat L20 irradiated to (a) 0.3 and (b) 0.9 x 10^{21} n·cm^{-2} (E > 1 Me) (0.45 and 1.35 dpa) at 288°C

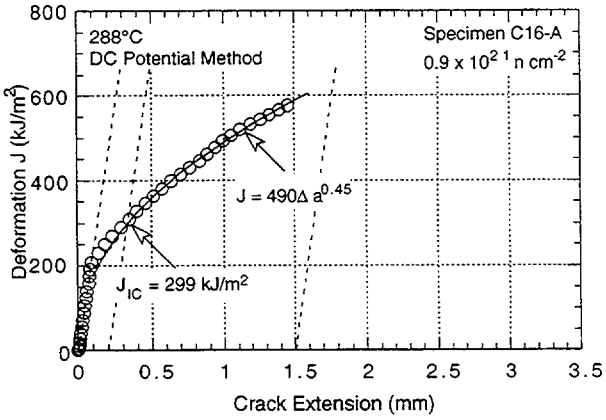

Figure 32.
Fracture toughness J–R curve at 288°C for Heat C16 irradiated to 0.9 x 10^{21} n·cm^{-2} (E > 1 Me) (0.45 dpa) at 288°C

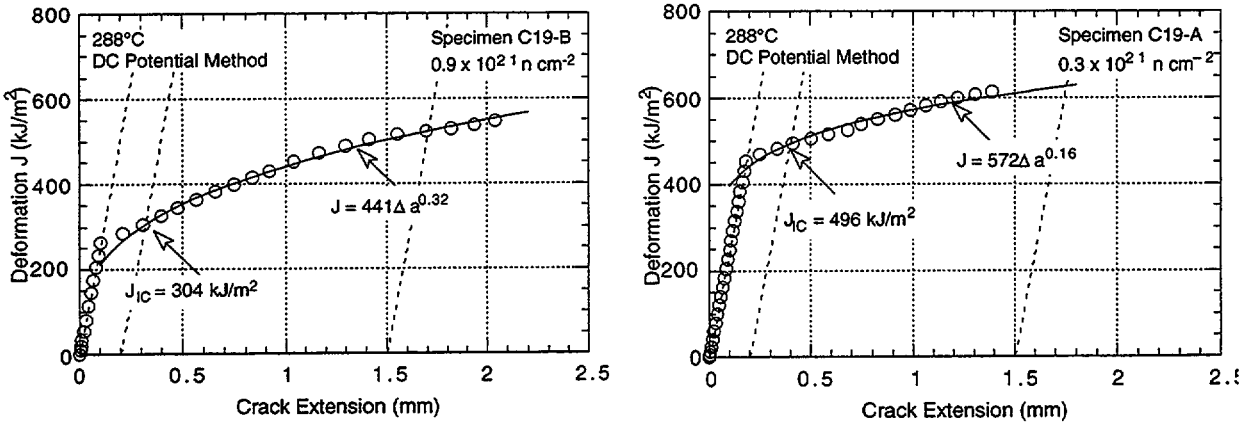

Figure 33. Fracture toughness J–R curve at 288°C for Heat C19 irradiated to (a) 0.3 and (b) 0.9 x 10^{21} n·cm^{-2} (E > 1 Me) (0.45 and 1.35 dpa) at 288°C

Neutron irradiation at 288°C decreases the fracture toughness of all steels. In general, fracture toughness of the commercial Heats C16 and C19 is superior to that of the laboratory Heats L20 and L2. The values of fracture toughness J_{IC} for the specimens irradiated to 0.9 x 10^{21} n·cm^{-2} (1.35 dpa) are 299 and 304 kJ/m^2 for Heats C16 and C19, respectively, and 38 and 39 kJ/m^2 for Heats L2 and L20, respectively. The differences between the fracture toughness of the irradiated commercial and laboratory heats arise primarily from differences in toughness of the nonirradiated steels, i.e., the fracture toughness of the laboratory heats is significantly lower than that of the commercial heats. For these materials, minor differences in the chemical composition of the steels, e.g., differences in nickel content for Heats C16 and C19 or silicon content for Heats L2 and L20, appear to have little or no effect on the fracture toughness of irradiated steels.

The differences in the fracture toughness of laboratory and commercial heats is reflected in their fracture behavior. Photomicrographs of the fracture surfaces of broken nonirradiated specimens of Heats L2, L20, and C19 are shown in Fig. 34. Heat L2 contains relatively high S and P contents and many clusters of MnS inclusions. Failure occurs primarily by grain boundary separation, which is accompanied by some plastic deformation and decohesion along the MnS clusters (Fig. 34d). Heat L20 exhibits a dimple fracture; failure occurs by nucleation and growth of microvoids and rupture of remaining ligaments. Heat L20 contains relatively high oxygen and many oxide particle inclusions. In Fig. 34b, nearly every dimple appears to have been initiated by decohesion of an oxide inclusion. An identical fracture behavior was observed for Heat L20 irradiated to 0.9 x 10^{21} n·cm^{-2} (1.35 dpa). In contrast, commercial heats exhibit ductile failure with some dimple fracture, as shown for Heat C19 in Fig. 34c.

The experimental J_{IC} values for the four heats are plotted as a function of neutron exposure in Fig. 35. Results from tests on Type 304 SS reactor internal materials from operating BWRs[83] are also included in the figure. All of the CT specimen data from commercial heats fall within the scatter band for the data obtained at higher temperatures.

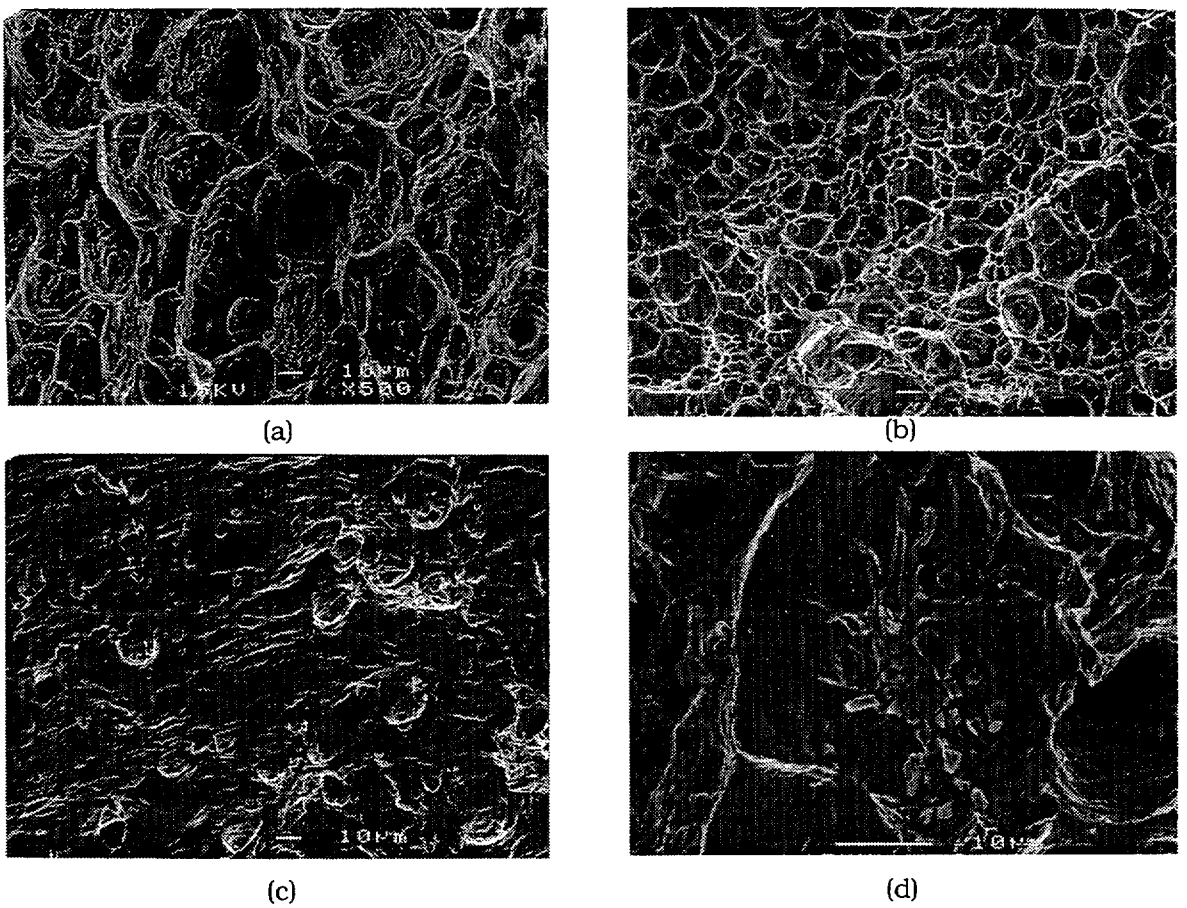

Figure 34. Photomicrographs of fracture surfaces of nonirradiated specimens of Heats (a) L2, (b) L20, and (c) C19 tested at 288°C, and (d) MnS inclusions in Heat L2

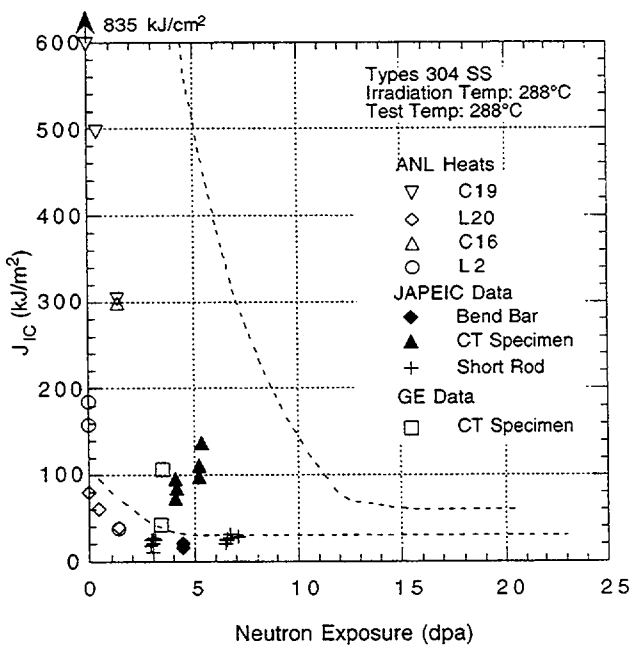

Figure 35.
Fracture toughness J_{IC} as a function of neutron exposure for austenitic Types 304 and 316 SS

4 Environmentally Assisted Cracking of Alloys 600 and 690 in Simulated LWR Water (W. K. Soppet, O. K. Chopra, and W. J. Shack)

The objective of this work is to evaluate the resistance of Alloys 600 and 690 to EAC in simulated LWR coolant environments. High-Ni alloys have experienced general corrosion (tube wall thinning), localized IGA, and SCC in LWRs. Secondary-side IGA* and axial and circumferential SCC** have occurred in Alloy 600 tubes at tube support plates in many steam generators. Primary-water SCC of Alloy 600 steam generator tubes in PWRs at roll transitions and U-bends and in tube plugs*** is a widespread problem that has been studied intensively. Cracking has also occurred in Alloy 600 and other high-Ni alloys (e.g., Inconel-82 and -182 and Alloy X750) that are used in applications such as instrument nozzles and heater thermal sleeves in the pressurizer† and the penetrations for control-rod drive mechanisms in reactor vessel closure heads in the primary system of PWRs;†† in dissimilar-metal welds between SS piping and LAS nozzles, in jet pump hold-down beams,††† and in shroud-support-access-hole covers§ in BWRs. Alloy 600, in general, undergoes differing thermomechanical processing for applications other than steam generator tubes. Because environmental degradation of the alloys in many cases is very sensitive to processing, further evaluation of even SCC is needed. In addition, experience strongly suggests that materials that are susceptible to SCC are also susceptible to environmental degradation of fatigue life and fatigue-crack growth properties. In this investigation, we have obtained information on the effect of temperature, load ratio R, and stress intensity (K) on EAC of Alloys 600 and 690 in simulated BWR and PWR water. The experimental details and results from this study are presented elsewhere.[104-107]

4.1 Fatigue Crack Growth Rates in Air

4.1.1 Alloy 600

The existing fatigue crack growth (da/dN) data on Alloy 600 have been analyzed to establish the effects of temperature, load ratio, frequency, and stress intensity range ΔK on crack growth rates in air. The relevant fatigue CGR (da/dN) data on Alloy 600 have been compiled by Kharshafdjian and Park.[103] The data base is composed of 465 tests in air[104-112] at temperatures up to 538°C; the number of tests at various temperatures are as follows: 166

*USNRC Information Notice No. 91-67, "Problems with the Reliable Detection of Intergranular Attack (IGA) of Steam Generator Tubing," Oct. 1991.

**USNRC Information Notice No. 90-49, "Stress Corrosion Cracking in PWR Steam Generator Tubes," Aug. 1990; Notice No. 91-43, "Recent Incidents Involving Rapid Increases in Primary-to-Secondary Leak Rate," July 1991; Notice No. 92-80, "Operation with Steam Generator Tubes Seriously Degraded," Dec. 1992; Notice No. 94-05, "Potential Failure of Steam Generator Tubes with Kinetically Welded Sleeves," Jan. 1994.

***USNRC Information Notice No. 89-33, "Potential Failure of Westinghouse Steam Generator Tube Mechanical Plugs," March 1989; Notice No. 89-65, "Potential for Stress Corrosion Cracking in Steam Generator Tube Plugs Supplied by Babcock and Wilcox," Sept. 1989; Notice No. 94-87, "Unanticipated Crack in a Particular Heat of Alloy 600 Used for Westinghouse Mechanical Plugs for Steam Generator Tubes," Dec. 1994.

†USNRC Information Notice No. 90-10, "Primary Water Stress Corrosion Cracking (PWSCC) of Inconel 600," Feb. 1990.

††USNRC Generic Letter 97-01: "Degradation of Control Rod Drive Mechanism and Other Vessel Closure Head Penetrations," Apr. 1, 1997; USNRC Information Notice No. 96-11, "Ingress of Demineralizer Resins Increases Potential for Stress Corrosion Cracking of Control Rod Drive Mechanism Penetrations," Feb. 1996; INPO Document SER 20-93 "Intergranular Stress Corrosion Cracking of Control Rod Drive Mechanism Penetrations," Sept. 1993.

†††USNRC Information Notice 93-101, "Jet Pump Hold-Down Beam Failure," Dec. 1993.

§USNRC Information Notice 92-57, "Radial Cracking of Shroud Support Access Hole Cover Welds," Aug. 1992.

at room temperature, 13 at 35°C, 9 at 130°C, 14 at 289°C, 26 at 316°C, 20 at 320°C, 11 at 380°C, 76 at 427°C, and 130 at 538°C. The composition of the various heats of Alloy 600 used in these studies are given in Table 11 and their heat treatment conditions and mechanical properties are given in Table 12.

The EDEAC (EPRI Database for Environmentally Assisted Cracking) fatigue crack growth data base for SSs indicate that in addition to material considerations, the temperature, stress ratio R, and cyclic frequency have a significant effect on CGRs.[113] Growth rates are best represented by

$$da/dN = C\ F\ S\ (\Delta K)^n, \tag{22}$$

where the coefficients C, F, and S provide the dependence of temperature, frequency, and stress ratio, and n is the exponent for the power-law dependence of growth rates on stress intensity factor range ΔK.

Table 11. Composition of Alloy 600 heats used for fatigue crack growth studies in air

Source	Heat	C	Si	Ni	Cr	Fe	Mn	P	S	Cu	Mo	Ti	Al	Co	Nb+Ta
EPRI	NX0922	0.032	0.24	77.50	14.73	6.99	0.18	0.003	0.003	0.006	0.03	0.30	0.12	0.01	-
James	NX9929	0.050	0.28	77.38	15.24	6.69	0.32	-	0.007	0.010	-	0.17	0.06	0.07	-
Amzallag et al	-	0.060	0.33	73.29	16.50	9.49	0.31	0.009	0.003	0.001	-	-	-	0.01	-
Nagano et al.	-	0.026	0.37	73.45	15.97	-	0.38	0.009	0.001	-	-	0.21	0.13	-	-
ANL	NX8197	0.080	0.27	73.82	15.43	9.20	0.20	0.016	0.002	0.110	0.58	0.18	0.24	0.06	0.07
ANL	NX8844B	0.080	0.27	75.16	15.03	7.93	0.24	0.019	0.001	0.220	0.17	0.21	0.28	0.04	0.04
ANL	NX8844J	0.060	0.32	74.94	15.00	8.14	0.23	0.014	0.002	0.220	0.16	0.24	0.24	0.03	0.03

Table 12. Heat treatment conditions and tensile properties[a] of Alloy 600 heats used for fatigue crack growth studies in air

Source	Heat	Heat Treatment Condition	Yield Stress (MPa)	Tensile Stress (MPa)	Red. in Area (%)
EPRI	NX0922	Mill-Annealed, 8 min at 1050°C Water-Quenched	310	640	-
Was & Ballinger	-	As Received	-	-	-
Was & Ballinger	-	Annealed 30 min at 1100°C	-	-	-
James	NX9929	Annealed 45 min at 863°C Air-Cooled	244	651	67.2
Amzallag et al.	-	Wrought Material, 950°C Air-Quenched	252	665	47.0
Nagano et al.	-	20 min at 1025°C WQ, 30% CW, 1 h at 700°C	-	-	-
Nagano et al.	-	45 min at 1025°C WQ, 30% CW, 1 h at 900°C WQ, 15 h at 700°C	156	523	67.9
ANL	NX8197	Mill-Annealed	383	684	41.9
ANL	NX8844B	Solution-Annealed 1 h at 872°C	337	732	37.6
ANL	NX8844J	Solution-Annealed 1 h at 1038°C	272	674	45.1

[a]At room temperature.

The existing fatigue CGR data on Alloy 600 were analyzed by using Eq. 22 to establish the effects of temperature, stress ratio R, cyclic frequency, and stress intensity factor range ΔK on the CGRs in air. First, the exponent n was determined from individual data sets in which only ΔK was varied and the temperature, frequency, and R were all constant. Plots of CGR vs.

ΔK from several data sets (Figs. 36 and 37) yield values of n in the range of 3.5–5.5; a value of 4.1 was selected for further analysis.

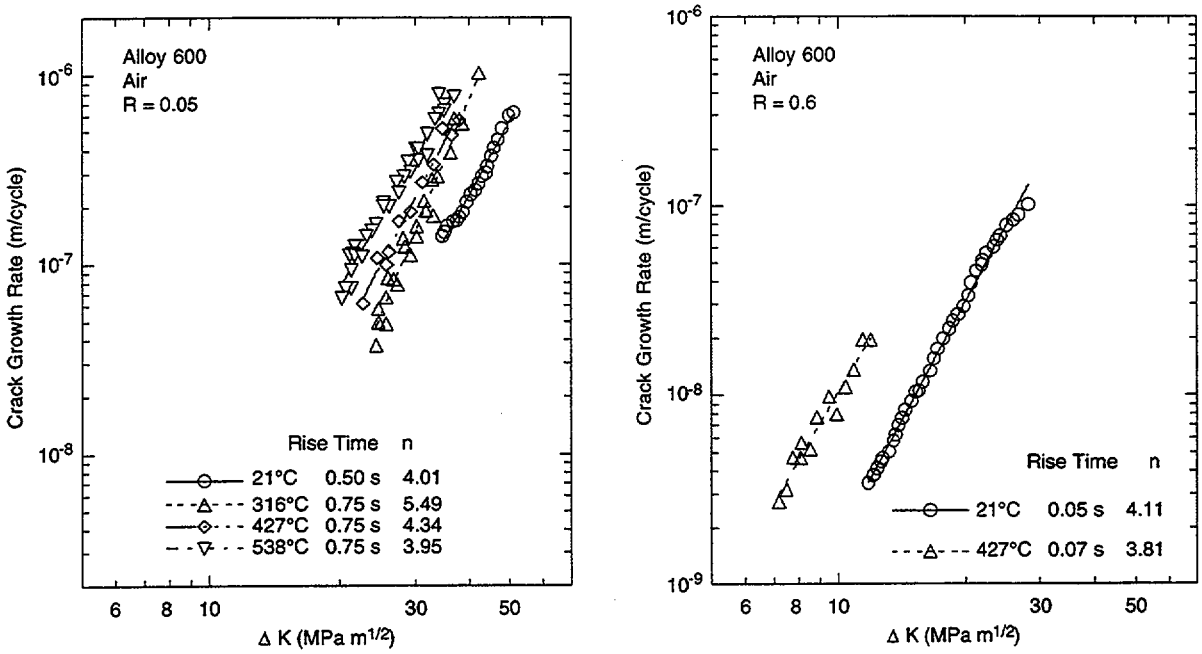

(a) (b)

Figure 36. Effect of temperature on fatigue crack growth rate of Alloy 600 in air. Data at 21°C from Ref. 112 (Was and Ballinger) and at higher temperatures from Ref. 108 (James).

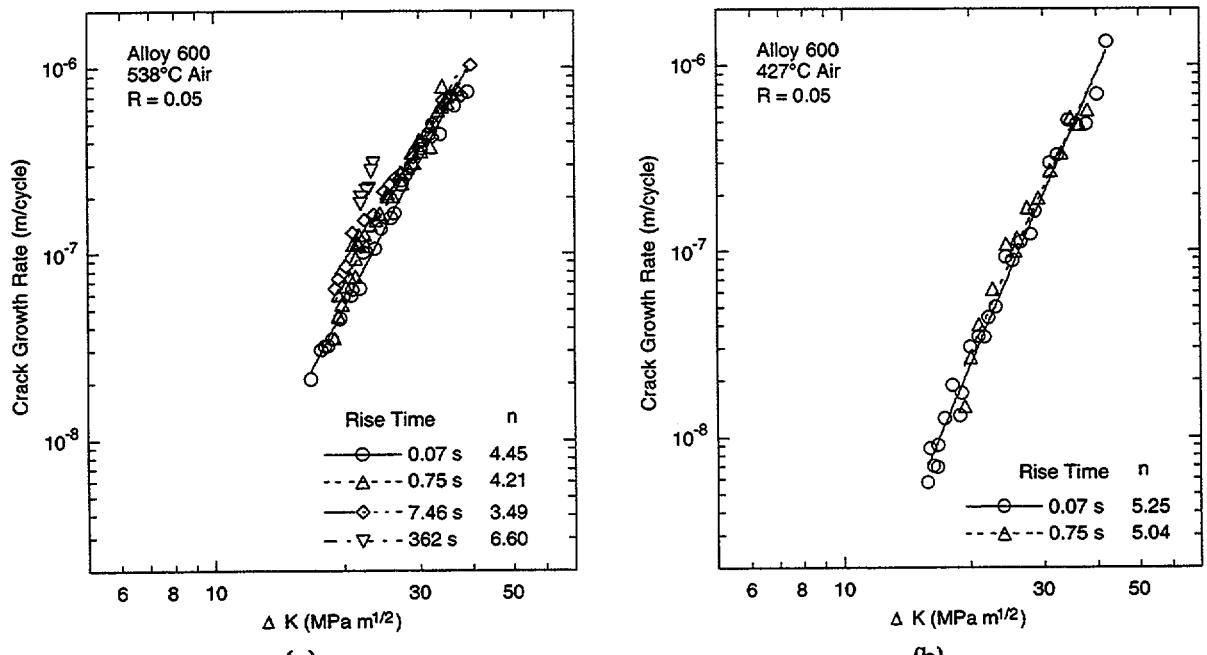

(a) (b)

Figure 37. Effect of rise time on fatigue crack growth rate of Alloy 600 in air. Data from Ref. 108 (James).

The results also indicate that the effects of temperature on growth rates are significant, whereas rise time or frequency has little effect on CGRs, i.e., coefficient F = 1 in Eq. 22. Because the cyclic stress ratio R has a significant influence on CGRs in association with K_{max}, various forms of coefficient S have been used by different investigators to treat stress-ratio effects on CGRs. For example, S has been expressed as (a + b R) for different regions of R < 0.79 and 0.70 < R < 1.0 (James and Jones),[113] $(a - R)^p$ (Bamford et al.),[114] $1/(1 - R)^{n/(1-p)}$ (Walker),[115,116] $[1/(1 - 0.05\ R^2)]^4$ (Bernard and Slama),[117] and $(a - R)^p$ (Rabbe and Lieurade),[118] where a, b, and p are constants. The following form of coefficient S yielded the best fit to the experimental data in air

$$S = (1 - b\ R)^{-p}, \tag{23}$$

where R is the stress ratio and b and p are constants. Best fits to individual data sets at constant temperature yield values of 0.82 and –2.2 for constants b and p, respectively. Finally, the temperature dependence of coefficient C was determined from data sets that were normalized for the effects of load ratio R (Fig. 38). The results indicate significant variation in coefficient C from either heat–to–heat differences or differences in heat treatment, e.g., at room temperature, C varies by a factor of 2 for the different heats and heat treatment conditions (Fig. 38). Two forms of the temperature dependence of coefficient C, an exponential or a third-order polynomial of temperature, were used to represent the experimental data; the latter gave a better fit of the data. Thus, the CGR (m/cycle) of Alloy 600 in air is expressed as

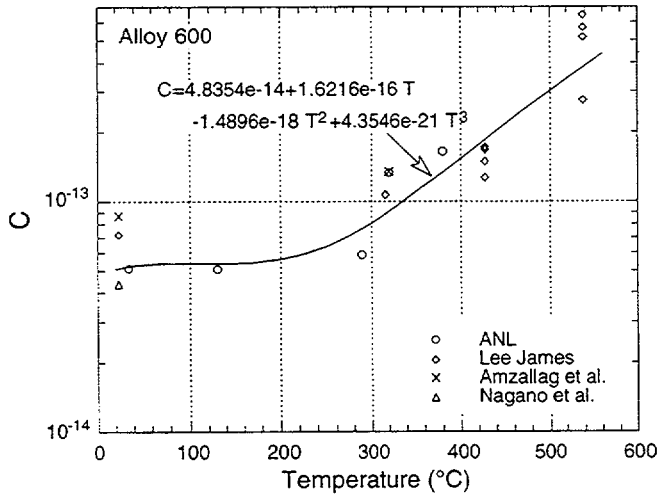

Figure 38.
Variation of constant C for Alloy 600 with temperature. Data obtained at ANL (Refs. 104–107) and by James (Ref. 108), Amzallag et al. (Ref. 110), and Nagano et al. (Ref. 111).

$$da/dN = C_{A600}\ (1 - 0.82\ R)^{-2.2}\ (\Delta K)^{4.1}, \tag{24}$$

where ΔK is in $MPa \cdot m^{1/2}$, and constant C_{A600} is given by a third-order polynomial of temperature T (°C) expressed as

$$C_{A600} = 4.835 \times 10^{-14} + 1.622 \times 10^{-16}\ T - 1.490 \times 10^{-18}\ T^2 + 4.355 \times 10^{-21}\ T^3. \tag{25}$$

The residual errors for each variable are plotted in Fig. 39. Most data subsets and plots do not show significant patterns, such as changing variance or a nonzero slope. In general, Eqs. 24 and 25 represent the existing CGR data very well; biases seem to be traceable to either

heat–to–heat variation or changes in heat treatment condition. The predicted vs. experimental CGRs for Alloy 600 at different temperatures are shown in Fig. 40.

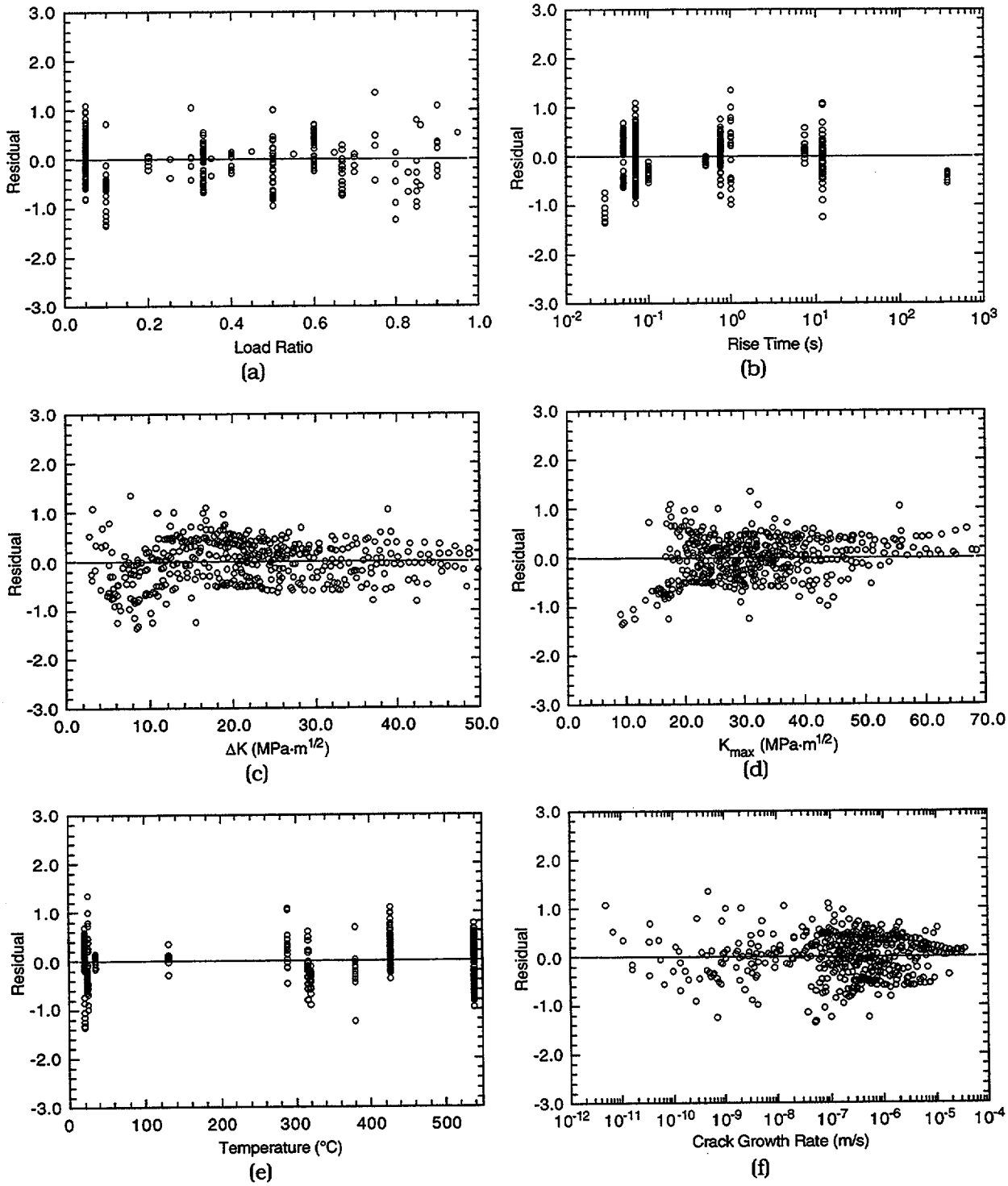

Figure 39. Residual error for CGRs of Alloy 600 in air as a function of (a) load ratio, (b) rise time, (c) stress intensity range ΔK, (d) K_{max}, (e) temperature, and (f) crack growth rate

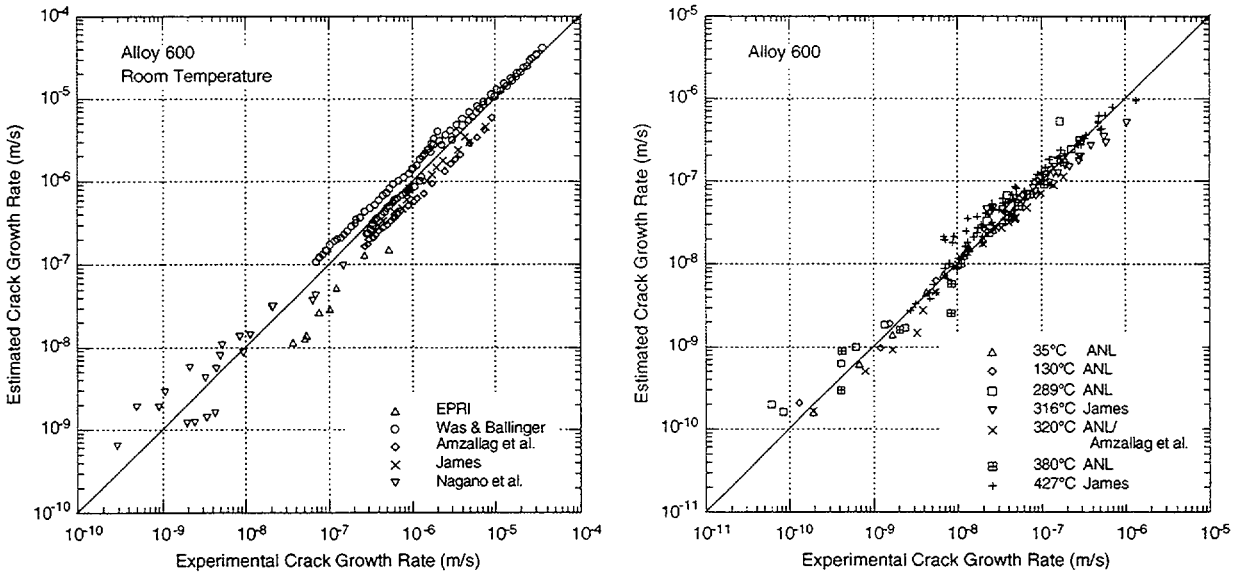

Figure 40. Predicted vs. experimental values of fatigue crack growth rate of Alloy 600 in air at (a) room temperature and (b) temperatures between 35 and 427°C. Data obtained at ANL (Refs. 104–107) and by James (Ref. 108), EPRI (Ref. 109), and Amzallag et al. (Ref. 110).

4.1.2 Alloy 690

The fatigue CGR (da/dN) data on Alloy 690 in air are very limited.[104–107] The data base is composed of ≈60 tests at temperatures between 35 and 380°C. The composition of the various heats of Alloy 690 used in these studies are given in Table 13 and their heat treatment conditions and mechanical properties are given in Table 14.

Table 13. Composition of Alloy 690 heats used for fatigue crack growth studies in air

Source	Heat	C	Si	Ni	Cr	Fe	Mn	P	S	Cu	Mo	Ti	Al	Co	Nb+Ta
ANL	NX8244HK-1A	0.024	0.18	59.09	30.66	9.22	0.20	0.004	0.002	<0.01	<0.01	0.20	0.31	<0.01	<0.01
ANL	NX8244HK-1B	0.023	0.18	59.20	30.64	9.19	0.21	0.005	0.002	<0.01	<0.01	0.19	0.32	<0.01	<0.01
ANL	NX8662HG-33	0.030	0.16	58.88	30.46	9.22	0.11	0.017	0.001	0.05	0.04	0.25	0.32	0.02	0.01

Table 14. Heat treatment conditions and tensile properties of Alloy 690 heats used for fatigue crack growth studies in air

Source	Heat	Heat Treatment Condition	Yield Stress MPa	Tensile Stress MPa	Red. in Area %
ANL	NX8244HK-1A	Annealed 1 h at 982°C	251	656	54.0
ANL	NX8244HK-1B	Annealed 1 h at 1093°C	214	598	64.8
ANL	NX8662HG-33	Annealed + Heat Treated 5 h at 715°C	292	677	46.1

The existing fatigue CGR data on Alloy 690 in air are inadequate to establish the effects of stress ratio R, cyclic frequency, and stress intensity factor range ΔK on the CGRs in Eq. 22. The functional forms for coefficients F and S and the value of n in Eq. 22 were assumed to be the same as those for Alloy 600. The temperature dependence of coefficient C was determined from data sets that were normalized for the effects of load ratio R (Fig. 41). Thus, the CGR (m/cycle) of Alloy 690 in air is expressed as

$$da/dN = C_{A690} (1 - 0.82\ R)^{-2.2} (\Delta K)^{4.1}, \quad (26)$$

where ΔK is in MPa·m$^{1/2}$ and constant C_{A690} is given by a third-order polynomial of temperature T (°C) expressed as

$$C_{A690} = 5.423 \times 10^{-14} + 1.83 \times 10^{-16}\ T - 1.725 \times 10^{-18}\ T^2 + 5.490 \times 10^{-21}\ T^3. \quad (27)$$

The predicted vs. experimental CGRs for Alloy 600 at different temperatures are shown in Fig. 42. The estimated values show good agreement with the experimental results.

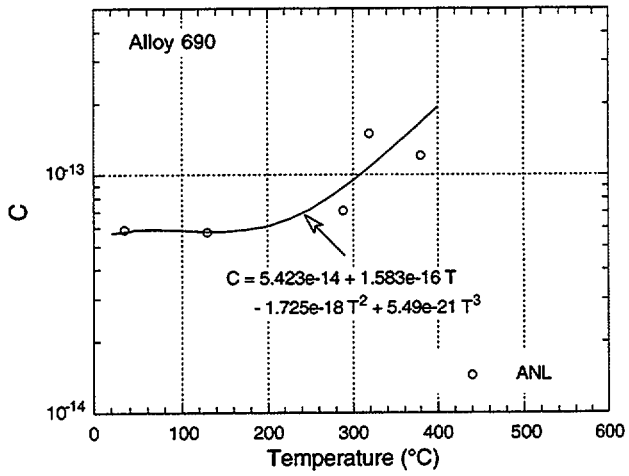

Figure 41.
Variation of constant C for Alloy 690 with temperature. Data obtained at ANL (Refs. 104–107).

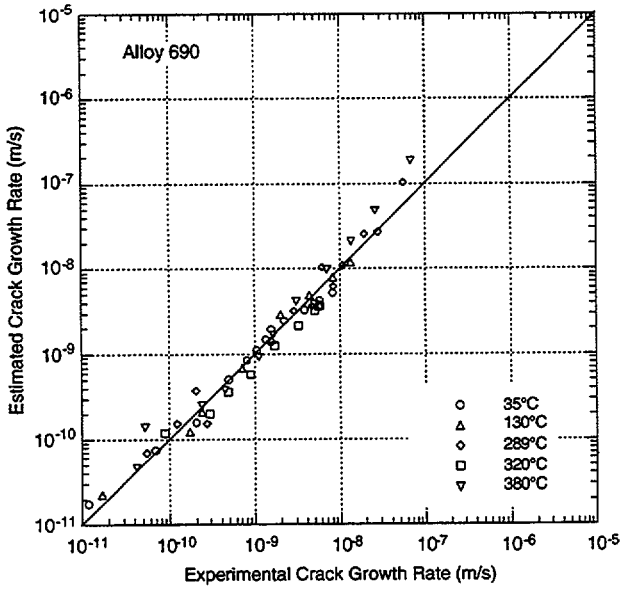

Figure 42.
Predicted vs. experimental values of fatigue crack growth rate of Alloy 690 in air at temperatures between 35 and 380°C. Data obtained at ANL (Refs. 104–107).

5 Assessment of Industry Crack-Growth Models (W. J. Shack)

5.1 Introduction

The PLEDGE code is based on the work done by Ford and Andresen and their colleagues at General Electric (GE) on environmentally assisted cracking. This work has been described in many papers and presentations, and a recent survey paper by Ford[119] contains many references. More details of the supporting experiments and the model are given in Ref. 120.

The Ford–Andresen model assumes that the CGR can be correlated with the oxidation that occurs when the protective film at the crack tip is ruptured.[119] Faraday's law can be used to relate the oxidation charge density (Q) to the amount of metal transformed from the metallic state to the oxidized state or dissolved. In reactor systems, the protective oxide reforms rapidly at the bared surface, and crack advance can be maintained only if the crack tip is being strained so that the film rupture process can be repeated. The frequency of rupture is $\dot{\varepsilon}_{ct}/\varepsilon_f$, where ε_f is the fracture strain of the oxide and $\dot{\varepsilon}_{ct}$ is the crack tip strain rate. The average CGR is then

$$v = \frac{M}{z\rho F}\frac{Q}{\varepsilon_f}\dot{\varepsilon}_{ct}, \tag{28}$$

where M and ρ are the atomic weight and density of the crack–tip metal, F is Faraday's constant, and z is the number of electrons involved in the overall oxidation of an atom of metal. The oxidation charge can be obtained by integrating over time the oxidation current that occurs after the rupture event, which is assumed to follow a power law relationship of the form:

$$i = i_o\left[\frac{t}{t_o}\right]^{-n}, \tag{29}$$

where i_o and t_o are constants that depend on the material, potential, and environment. Integrating Eq. (and eliminating Q from Eq. 28 gives:

$$v \approx \frac{M}{z\rho F}\frac{i_o t_o^n}{(1-n)\varepsilon_f^n}\dot{\varepsilon}_{ct}^n. \tag{30}$$

To use Eq. 30 to obtain quantitative predictions of CGR, Ford and Andresen have carried out three types of experiments and calculations:

1. Definition of the crack tip alloy/environment in terms of material composition, electrochemical potential (ECP), anion content, and pH.

   These are related to the corresponding bulk water chemistry parameters through modeling of potential-driven transport and experiments on simulated crevices. The models and experiments suggest that the potentials at the crack tip are low and that the impurity concentrations (SO_4^{2-}) at the crack tip are 100–200 times greater than those in the bulk solution. The crack tip material is characterized in terms of the degree of chromium depletion. For example, solution-annealed material corresponds to Fe-18Cr-

8Ni, sensitized material corresponds to a lower chromium content such as Fe12Cr10Ni or Fe-8Cr-10Ni, and highly sensitized material is bounded by assuming that the grain boundary is chromium-free, i.e., Fe.

2. Measurement of the oxidation current that is produced when the protective film on a material corresponding to crack tip material is ruptured in an environment corresponding to the crack tip environment.

   Ford and Andresen made these measurements through experiments in which the protective film on a thin wire specimen is removed by first applying a reducing potential and then quickly pulsing the specimen to the potential of interest and measuring the current flow as a function of time. The parameters i_o, t_o, and n are determined as functions of the material, potential, and environment by fitting the resulting current decay curves with a power law of the form Eq. 29.

3. Definition of the crack tip strain rate $\dot{\varepsilon}_{ct}$, which controls the rate of rupture of the protective film at the crack tip in terms of parameters such as crack tip stress intensity factor K and frequency.

   Under constant load, $\dot{\varepsilon}_{ct}$ is usually assumed to be proportional to K^m. The proportionality constant and m are determined empirically. For cyclic loading, Shoji showed that $\dot{\varepsilon}_{ct}$ is proportional to the CGR in an inert environment (air).[121] The proportionality constant is determined empirically. The crack growth contributions from the cyclic and constant loads are summed,

$$v = v_{air} + A\left(\dot{\varepsilon}_{ct_{cyclic}}\right)^m + A\left(\dot{\varepsilon}_{ct_{const}}\right)^m \tag{31}$$

   rather than summing the crack tip strain rates, i.e.,

$$v = v_{air} + A\left(\dot{\varepsilon}_{ct_{cyclic}} + \dot{\varepsilon}_{ct_{const}}\right)^m . \tag{32}$$

The general description of the stress corrosion cracking process that underlies PLEDGE is now widely accepted. It provides the conceptual framework in which most workers in this area discuss their results or refine models for certain aspects of problem,[121-123] although some of assumptions related to crevice electrochemistry have been a matter of discussion.[124–127] A comprehensive independent survey of some related studies has been provided by Turnbull and Psaila-Dombrowski.[125]

The actual implementation and development of the model is considered proprietary by GE. It is clear that the processes involved are complex and that a number of assumptions and approximations must be introduced. In addition to the experiments necessary to determine the oxidation current, etc., PLEDGE also requires purely empirical calibration to determine, e.g., the constants needed to define $\dot{\varepsilon}_{ct}$. Tto use this code for regulatory purposes, the uncertainties in these predictions due to uncertainties in the assumptions of the models used to develop the code and the uncertainties in the quantitative parameters used in the code must be addressed. It appears unrealistic to do this on a "first principles" basis by identifying the uncertainties in

each part of the model and then propagating those uncertainties through the model. The only practical approach is through comparison with relevant experimental measurements of CGRs.

In this report, PLEDGE predictions are compared with experimental data collected by the BWRVIP,[128] data developed at ANL as part of USNRC-sponsored research, data provided by P. L. Andresen of GE,* data used to develop the original USNRC disposition curve, and other data gathered from the literature.[129-136] Some of the data provided by Andresen were developed at GE, while other data were developed at ABB and VVT as part of an SCC CGR round-robin sponsored by the Swedish nuclear regulatory authority SKI.[137] The BWRVIP-14 database is proprietary. For some of the older ANL data at high dissolved oxygen (DO) levels (7–8 ppm) and for some of the data from the literature (such as that used to develop the original USNRC disposition curve), ECP measurements were not available. These data were included by using assumed values for the ECP; this was felt to be reasonable because at these oxygen levels, the ECP is only a weak function of the DO level.

5.2 Overall Comparisons with Experimental Data

A database of experimentally determined CGRs under conditions considered more representative of BWR conditions was developed from data reported in BWRVIP-14[128] and from data developed at ANL as part of USNRC-funded research on environmentally assisted cracking and from the data supplied by P. L. Andresen. About 40% of the data are from constant load tests; the remainder are from cyclic load tests with load ratios R between 0.9 and 0.95 and frequencies of 0.08 Hz or less. The tests cover a wide range of sensitization conditions, conductivities, electrochemical potentials, and stress intensity factors. The BWRVIP database contains data for temperatures from 240–289°C. Only the data with temperatures greater than 262°C were compared with PLEDGE, because PLEDGE does not include temperature as a variable. None of the materials are from actual weldments. The materials were sensitized by furnace heat treatment.

The comparison was limited to tests with $20 \le K \le 40$ MPa·m$^{1/2}$. The upper limit on K was introduced to ensure validity of the CGR measurements from a fracture mechanics standpoint. The lower limit on K was introduced to minimize confounding of data for active crack growth with data that show anomalously low crack growth velocities. As Andresen observed,[137] there are many reasons for anomalously low crack growth rates in stress corrosion tests: incomplete transition from the transgranular fatigue starter crack to intergranular cracking, residual stresses from fabrication, machining, or fatigue precracking, test perturbations in load, temperature, or water chemistry. Although these problems can affect results at any K value, they become more acute for lower values of K. Experience suggests that it is easier to achieve more consistent results at stress intensities of 20-25 MPa·m$^{1/2}$. Inclusion of data at lower K values will contribute to scatter; models will tend to overpredict CGRs in these cases.

All of the data in the BWRVIP-14 and Andresen databases were assumed to represent intergranular cracking. Many of the data in the ANL represent transgranular cracking under cyclic loading. For comparison with PLEDGE, the ANL data were split into two groups, one in which the cracking was intergranular, and the other in which the cracking was transgranular.

---

*Personal Communication, P. L. Andresen (GE) to W. J. Shack (ANL), October 1998.

There is considerable scatter in all the data sets. This reflects the experimental difficulties in measuring the low crack growth rates of practical interest and in measuring and controlling all the test parameters that can affect stress corrosion crack growth rates. The crack tip strain rates are also sensitive to thermomechanical loading history and the detailed microstructure. There is considerably more scatter for the BWRVIP data than for the ANL data or SKI round-robin data. This is not unexpected. The BWRVIP data were obtained under constant-load conditions, which tend to produce more scatter than the low-amplitude "ripple" loading used to develop most of the ANL data or the long-rise-time cyclic loading in the SKI tests. In addition, the SKI round-robin showed that the "normal" testing procedures used by the round-robin laboratories, which contributed heavily to the BWRVIP database, led to a wide range of scatter and uncertainty in the CGRs and ECPs.[137] The Andresen data were developed after the procedures at the round-robin laboratories were revised to provide more consistent and reproducible results. The requirements for "good" SCC data identified by Andresen include comparison of inlet and outlet conductivities, identification of the species responsible for the measured conductivity, relation of inlet and outlet DO, position of the reference electrode, and verification of the measured CG by posttest fractography. It is difficult to assess the validity of the BWRVIP data in these terms on the basis of the information available. The ANL data meet most of these requirements except for direct measurement of ECP on the specimen. Scatter in SCC testing is undoubtedly significant and greater than in mechanical fatigue testing.

An important input to PLEDGE is the electropotentiokinetic reactivation (EPR), a measure of the degree of sensitization of the material. Variations in EPR value over the range of 0–30 C/cm^2 result in a factor of ≈ 50 change in the crack growth rates predicted by PLEDGE at high ECP. EPR provides a characterization of the grain boundary chromium level. However, the correlation between EPR and grain boundary chromium content is subject to significant uncertainty. Because EPR depends on both width and depth of the chromium-depleted zone, the EPR value depends strongly on the overall thermal history and not just on the grain boundary chromium content. For example, low-temperature aging tends to produce narrower depleted zones than high-temperature aging treatments, so that an EPR value for a low-temperature-aged material corresponds to a lower grain boundary chromium concentration than that corresponding to the same EPR value for a high-temperature-aged material. The calculations with PLEDGE used reported values of the EPR except for the ANL data, which used a two-step sensitization process containing a low-temperature-aging step. In this case, the value reported by ANL was 2 C/cm^2. Because this would underestimate the EPR value that would be observed for the same grain boundary chromium level in a material with a high-temperature treatment, a value of 15 C/cm^2 was initially assumed in the calculations. Because EPR, as used in PLEDGE, is not truly a measured quantity (it really reflects the analyst's judgment as to the degree of chromium depletion at the grain boundary), the strong dependence on EPR makes it a potent "adjustable" parameter. Post-hoc adjustments of the EPR value would permit PLEDGE predictions to be "tuned" to experimental data.

The PLEDGE predictions are compared in Fig. 43 with the Andresen, ANL IGSCC, and BWRVIP databases. Although there is considerable scatter in the results, in almost all cases the PLEDGE prediction is conservative. PLEDGE predictions are compared with ANL TGSCC in Fig. 44. In this case, the appropriate EPR value is 0 and there is no particular bias to the predictions. The number of conservative predictions are about the same as the number of nonconservative predictions.

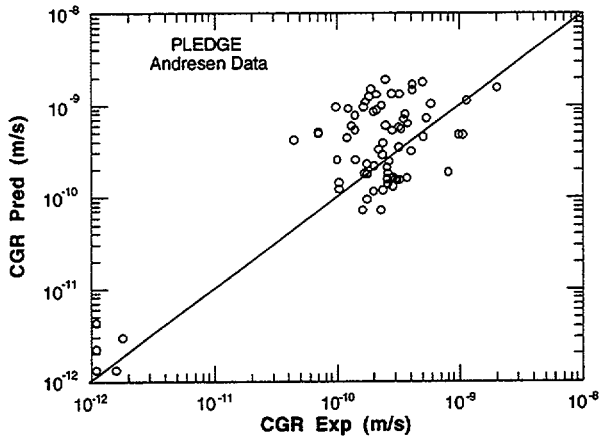

(a)

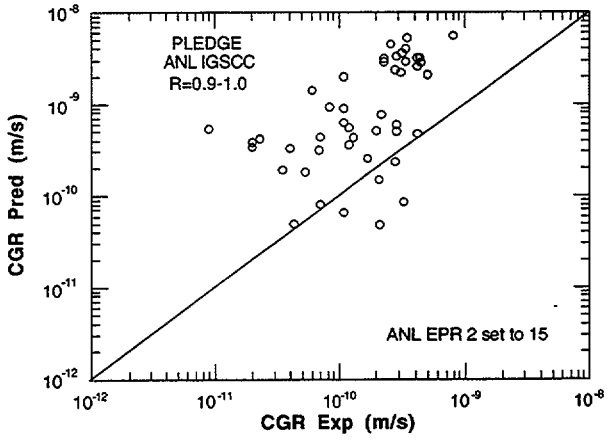

(b)

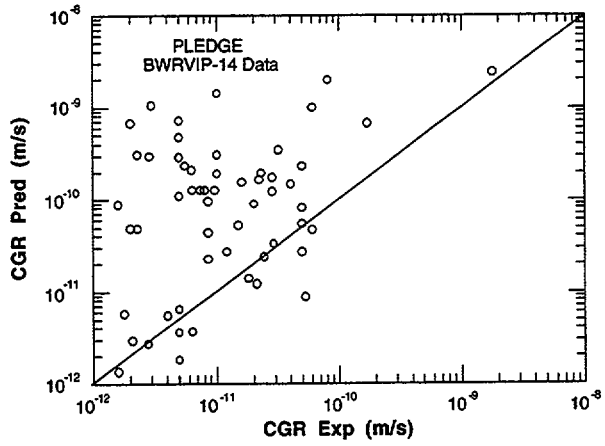

(c)

Figure 43.
(a) Comparison of PLEDGE model predictions with Andresen data set; (b) Comparison of PLEDGE model predictions with ANL IGSCC data set; (c) Comparison of PLEDGE model predictions with BWRVIP data set

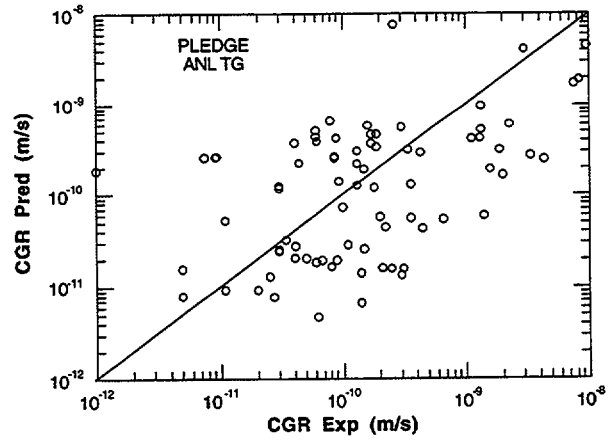

Figure 44.
Comparison of PLEDGE model predictions with ANL TG data set

The predictions of PLEDGE and the BWRVIP models with data for high-DO levels from ANL and Refs. 129 and 130 are shown in Fig. 45. Both the PLEDGE and BWRVIP models are conservative in most cases. In Fig. 46, comparisons are shown with cyclic CGR data from ANL and Refs. 131-136. With an EPR value of 15 C/cm^2 the PLEDGE predictions are conservative for both sensitized and nonsensitized materials. When the EPR value is set to 0, as would be appropriate for nonsensitized materials, the results are not necessarily conservative.

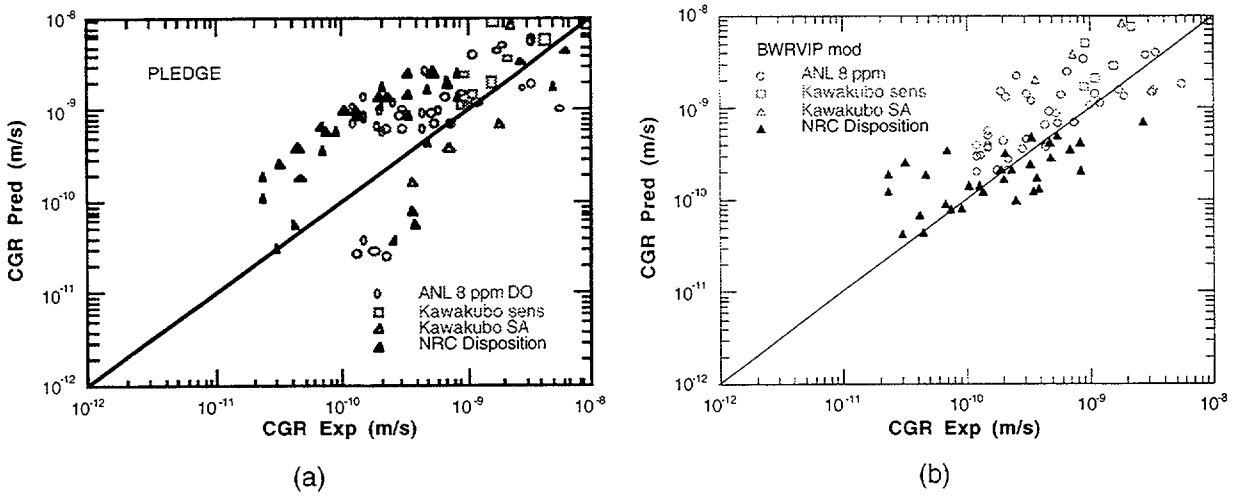

(a) (b)

Figure 45. (a) Comparison PLEDGE model predictions with ANL high–DO data, data from Kawakubo et al.,[129] and data used to develop NRC Disposition curve; (b) Comparison of BWRVIP 95 model predictions modified to account for cyclic loading with same data.

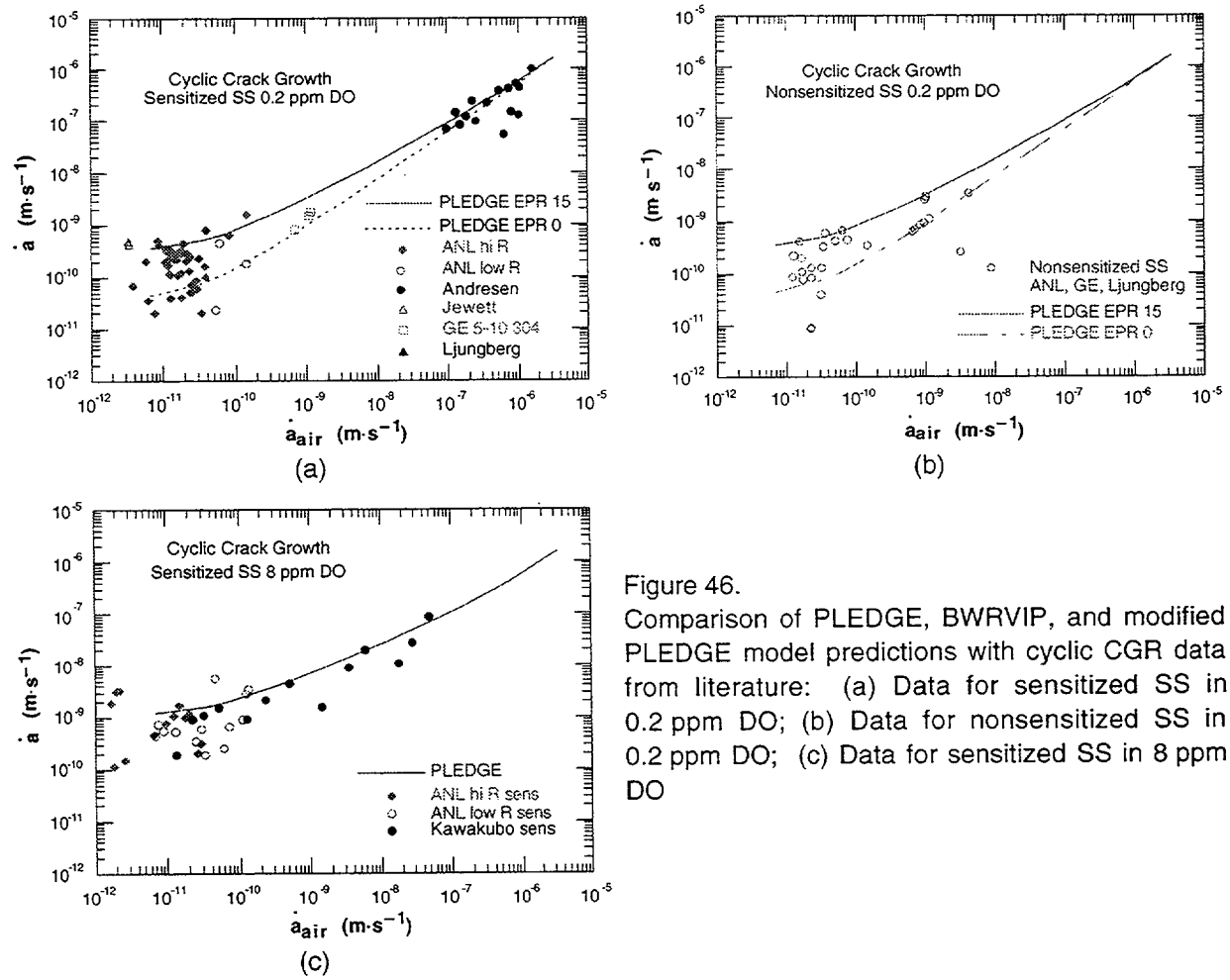

(a) (b)

(c)

Figure 46.
Comparison of PLEDGE, BWRVIP, and modified PLEDGE model predictions with cyclic CGR data from literature: (a) Data for sensitized SS in 0.2 ppm DO; (b) Data for nonsensitized SS in 0.2 ppm DO; (c) Data for sensitized SS in 8 ppm DO

PLEDGE appears to provide conservative predictions of crack growth rates in sensitized materials if an appropriate value is used for EPR. For applications to weldments, a value of 15 C/cm^2 appears appropriate and yields a moderate degree of conservatism. For environmentally assisted fatigue for which the growth is expected to be transgranular, the choice of EPR = 0 gives reasonable values for the mean behavior, but does not bound much of the data. Some additional margin appears appropriate. This could again be provided by assuming EPR = 15 C/cm^2.

Tablle 15. Mean error (ME) difference between PLEDGE predictions of CGR and experimental measurements for the four data sets

	BWRVIP	ANL IGSCC	Andresen	ANL TGSCC
Upper 95% ME	10.5	6.3	1.8	0.8
ME	8.3	5.2	1.6	0.7
Lower 95% #15 ME	6.5	4.4	1.4	0.6

Table 15 shows the mean error (ME) expressed as the mean value of the ratio of the predicted crack growth rate to the observed crack growth rate so that perfect agreement would give ME = 1 for the four data sets. An ME > 1 implies the PLEDGE predictions are conservative. As noted previously from examination of Figs. 43-46, PLEDGE is generally conservative for all the data sets with intergranular cracking and slightly nonconservative for the transgranular cracking data.

The predictions are poorest in terms of both mean error and scatter for the BWRVIP data set. This set, which is based on constant-load tests, appears to be biased toward low crack growth rates. As discussed previously, Andresen[137] noted an inherent bias in experimental data on SCC toward low crack growth rates—there are more reasons for crack growth to be retarded than accelerated. Even in the SKI round-robin, the observed scatter in the data under conditions that were supposedly tightly controlled covered three orders in magnitude, and many tests were reported as giving no SCC under material, environmental, and loading conditions for which SCC would be expected and had been observed in other tests.[137] In an attempt to remove some of this bias, the BWRVIP data base was screened to eliminate data where the CGR seemed unreasonably (low less than one order of magnitude) for the nominal conditions of the test. No CGR data were screened out because they were too high. The results for the screened set are summarized in Table 16 and shown in Fig. 47(a). The mean error for the screened set is a factor of 2 smaller than that for the original BWRVIP data set.

Table 16. Mean error difference between PLEDGE predictions of CGR and experimental measurements for screened BWRVIP data set and ANL IGSCC data set using reported EPR values

	BWRVIP screened	ANL IGSCC No EPR adjustment
Upper 95% ME	5.3	1.3
ME	4.2	1.0
Lower 95% ME	3.2	0.8

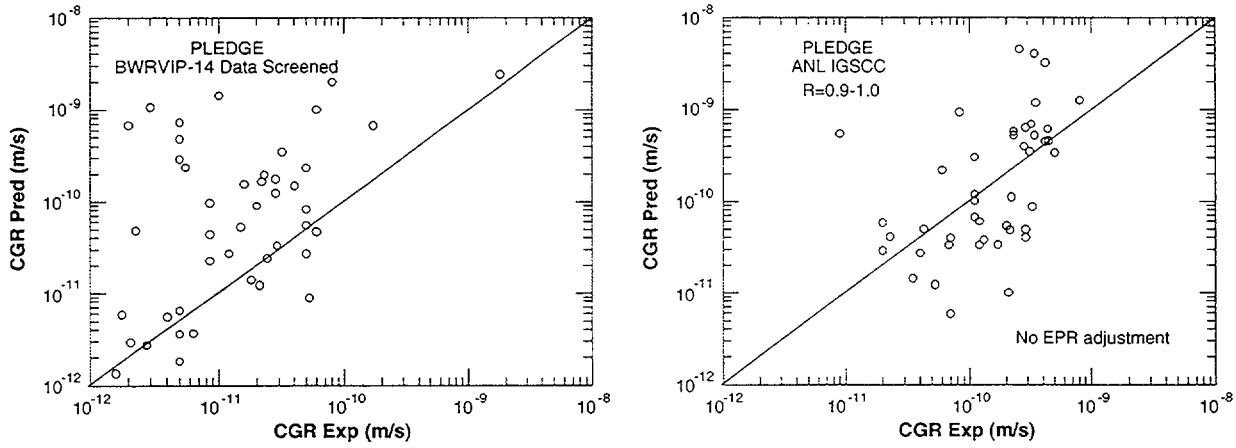

(a) (b)

Figure 47. (a) Comparison of PLEDGE model predictions with screened BWRVIP data set; (b) Comparison of PLEDGE model predictions with ANL IGSCC data set with no adjustment to reported EPR values

As discussed previously, because the ANL specimens with EPR = 2 C/cm^2 were sensitized with a low-temperature heat treatment that would be expected to give narrower and deeper Cr depletion zones than the higher-temperature heat treatments used to obtain most of the other reported data, an EPR of 15 C/cm^2 was used in the initial PLEDGE calculations instead of the value of 2 to make the ANL results more consistent with other reported results. If instead the actual reported values are used, the mean error decreases, as shown in Table 16 and Fig. 47 (b). This again emphasizes the sensitivity of PLEDGE predictions to the choice of EPR value. In most cases, EPR values will not be available, and even if they are it may be difficult to identify the appropriate correspondence with the values used by PLEDGE, which depend on the time/temperature histories used by Ford and Andresen to determine the EPR/Cr depletion/CGR correlation. Although the use of the reported EPR gives better agreement with the PLEDGE predictions, the fundamental meaning of EPR in PLEDGE says that the EPR value obtained with the ANL low-temperature heat treatment should be increased when making comparisons with PLEDGE calculations. The choice of the appropriate value is a matter of engineering judgment. An EPR of 15 C/cm^2 should be conservative for most welds and the ANL heat treatment. All references to comparisons of the ANL IG data with PLEDGE outside of Table 16 are based on EPR = 15 C/cm^2 for the low-temperature heat treatments.

5.3 Comparison of Specific Dependencies on EPR, Conductivity, and ECP

The errors were plotted as a function of the conductivity, ECP, EPR, and K to determine whether there was any correlation between these variables and the magnitude of the errors in the PLEDGE predictions. Examples of these graphs are shown in Figs. 48–51. These results suggest that errors are most strongly correlated to conductivity. To examine this more rigorously, the data were sorted into two categories: low-conductivity data with conductivities $\leq$ 0.2 μS/cm, and high-conductivity data with conductivities $\geq$ 0.2 μS/cm. As shown in Table 17, the PLEDGE predictions for the high- and low-conductivity data are significantly different for all the data sets. In each case, the PLEDGE predictions are more conservative for the high-conductivity data than for the low-conductivity data, i.e., PLEDGE overestimates the effect of increases in conductivity on increases in CGRs.

Table 17. Effect of conductivity on mean error difference between PLEDGE predictions of CGR and experimental measurements for the four data sets

	Andresen Low Conductivity	Andresen High Conductivity	ANL IG Low Conductivity	ANL IG High Conductivity
Upper 95% ME	1.1	4.6	4.3	10.4
ME	1.0	4.1	3.2	9.3
Lower 95% ME	0.9	3.6	2.5	8.4
	BWRVIP Low Conductivity	**BWRVIP High Conductivity**	**ANL TG Low Conductivity**	**ANL TG High Conductivity**
Upper 95% ME	3.4	10.4	0.3	5.0
ME	2.6	6.9	0.3	3.9
Lower 95% ME	2.0	4.6	0.2	3.1

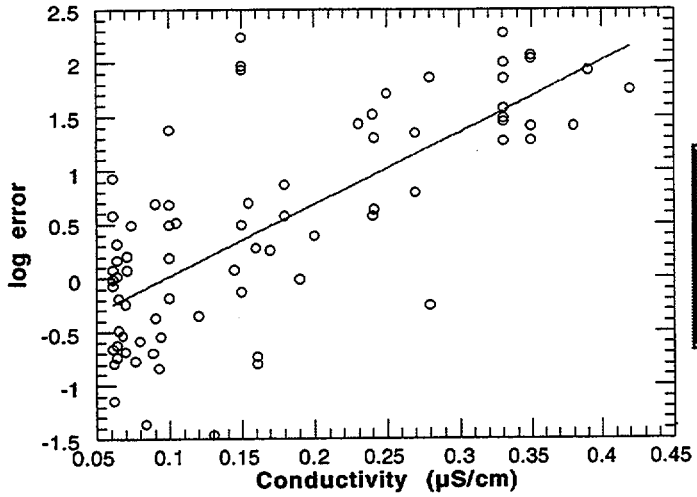

y = m1+m2*m0		
	Value	Error
m1	-0.64935	0.14196
m2	6.6696	0.71957
Chisq	34.538	NA
R	0.72843	NA

(a) Andresen

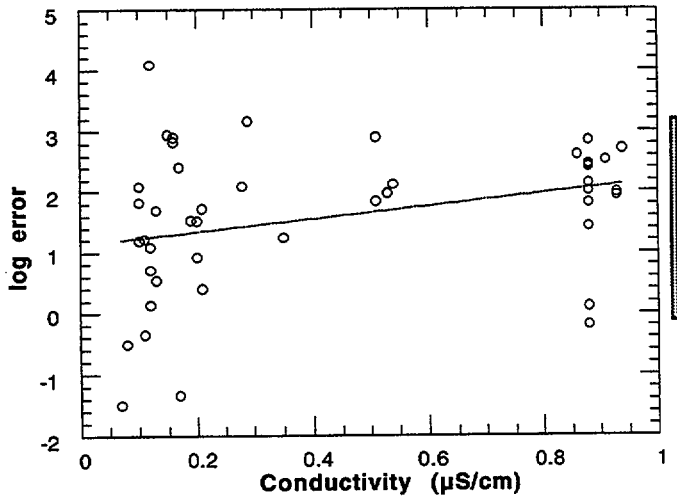

y = m1+m2*m0		
	Value	Error
m1	1.1259	0.27473
m2	1.0664	0.50141
Chisq	59.155	NA
R	0.30532	NA

(b) ANL IGSCC

Figure 48. Variation of errors in PLEDGE predictions with conductivity for (a) Andresen, (b) ANL IGSCC (with adjusted EPR values)

This has a significant effect when assessing the degree of conservatism associated with PLEDGE predictions. For modern BWRs, only the low-conductivity data are really relevant, and Table 17 shows that the conservatism of the PLEDGE predictions is lower by a factor of ≈2 than would be implied from the results for the complete data sets shown in Table 15.

Because of the fairly large effect of the conductivity on the errors associated with the PLEDGE predictions, attempts were made to examine effects of other variables based on examination of the data sets for either low or high conductivity rather than on the combined databases. However, too few data are generally available to obtain statistically significant comparisons. The screened BWRVIP database does contain enough low-conductivity data with differing degrees of sensitization to obtain some information on the effect of EPR, as shown in Table 18, which indicates that the PLEDGE calculations are more conservative for the more highly sensitized specimens, i.e., PLEDGE appears to overestimate the effect of EPR.

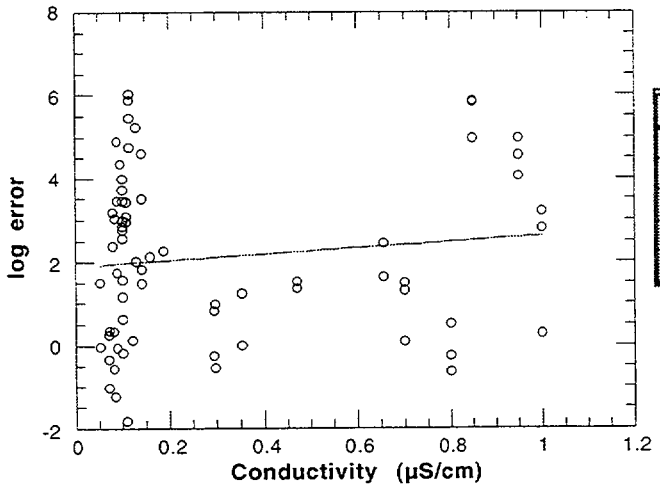

y = m1+m2*m0		
	Value	Error
m1	1.8937	0.33202
m2	0.72292	0.75623
Chisq	276.59	NA
R	0.11433	NA

(c) BWRVIP

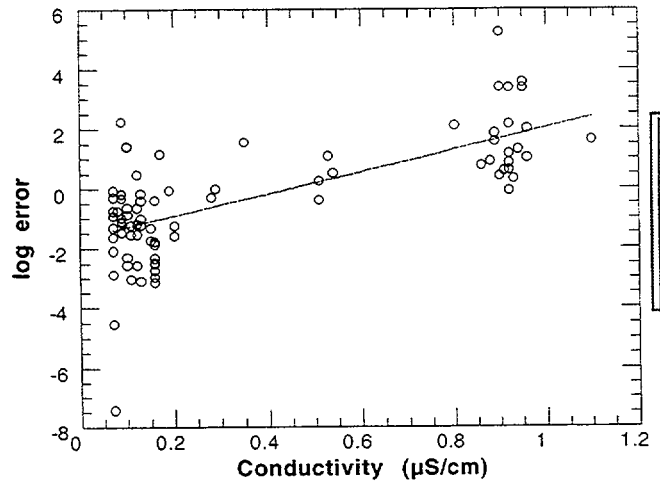

y = m1+m2*m0		
	Value	Error
m1	-1.6605	0.21567
m2	3.6909	0.44236
Chisq	179.55	NA
R	0.66885	NA

(d) ANL TGSCC

Figure 48. (contd). Variation of errors in PLEDGE predictions with conductivity for (c) BWRVIP, and (d) ANL TGSCC data sets

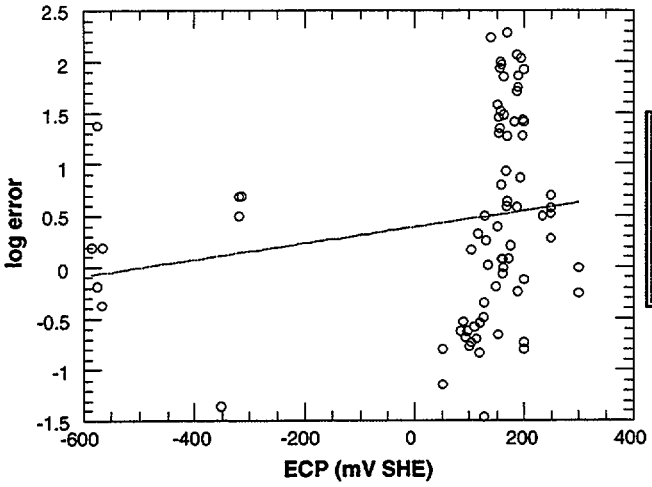

y = m1+m2*m0		
	Value	Error
m1	0.38907	0.11944
m2	0.00079075	0.00052444
Chisq	71.444	NA
R	0.17043	NA

(a) Andresen

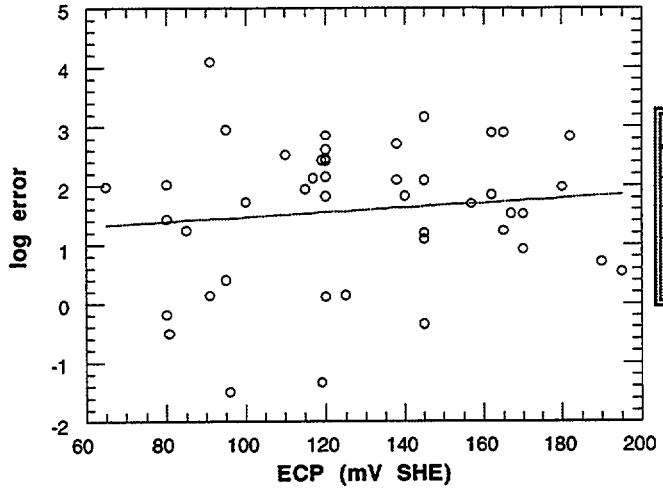

y = m1+m2*m0		
	Value	Error
m1	1.0601	0.71993
m2	0.0040725	0.0054291
Chisq	64.413	NA
R	0.11237	NA

(b) ANL IG

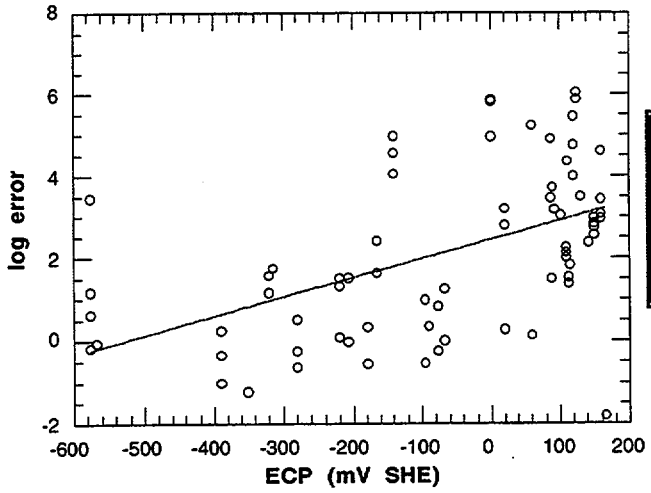

y = m1+m2*m0		
	Value	Error
m1	2.4509	0.2176
m2	0.0046416	0.0009541
Chisq	208.68	NA
R	0.50537	NA

(c) BWRVIP

Figure 49. Variation of errors in PLEDGE predictions with ECP for (a) Andresen, (b) ANL IGSCC (with adjusted EPR values), (c) BWRVIP

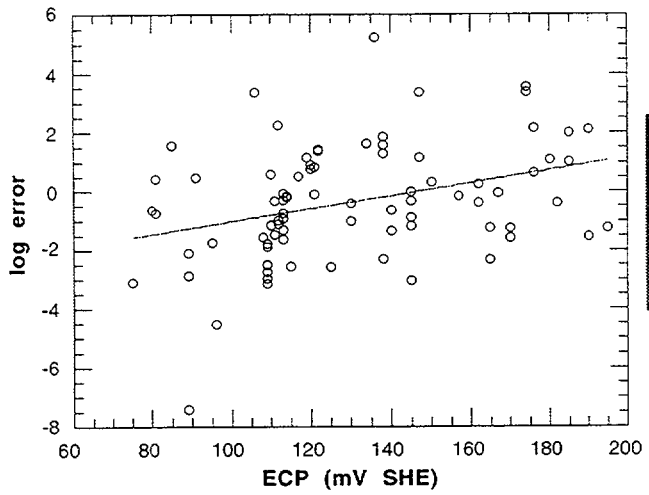

y = m1+m2*m0		
	Value	Error
m1	-3.2116	0.84993
m2	0.021911	0.00645
Chisq	286.46	NA
R	0.34396	NA

(d) ANL TGSCC

Figure 49. (contd). Variation of errors in PLEDGE predictions with ECP for (d) ANL TGSCC data sets

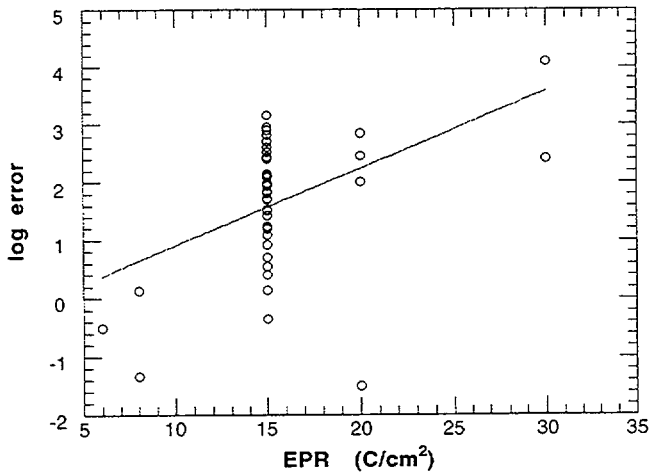

y = m1+m2*m0		
	Value	Error
m1	-0.42568	0.63911
m2	0.13339	0.039638
Chisq	47.012	NA
R	0.46084	NA

(a) ANL IG

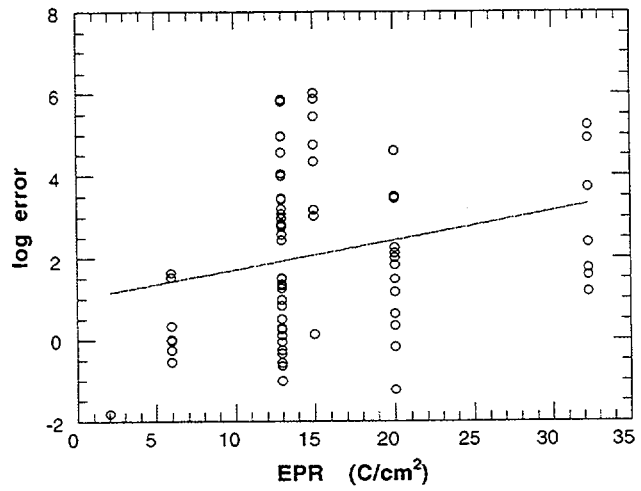

y = m1+m2*m0		
	Value	Error
m1	0.99279	0.57971
m2	0.072127	0.034138
Chisq	263.22	NA
R	0.2465	NA

(b) BWRVIP

Figure 50. Variation of errors in PLEDGE predictions with EPR for (a) ANL IGSCC (with adjusted EPR values) and (b) BWRVIP data sets

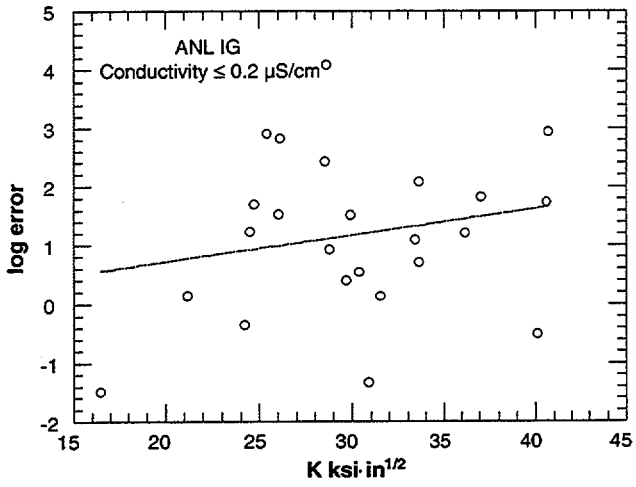

y = m1+m2*m0		
	Value	Error
m1	-0.18808	1.4244
m2	0.045353	0.046416
Chisq	41.142	NA
R	0.20394	NA

(a) ANL IGSCC

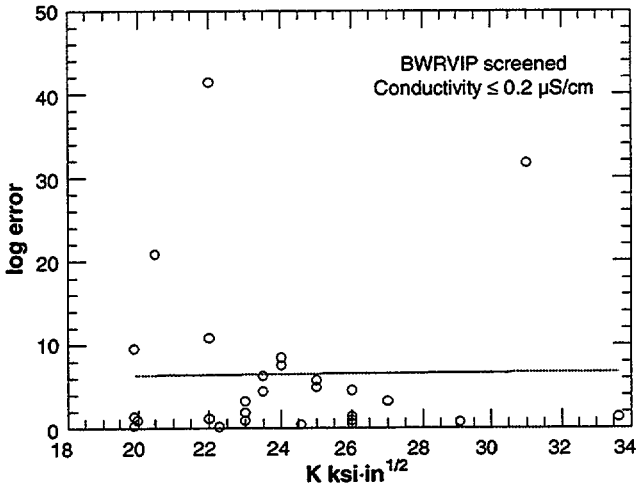

y = m1+m2*m0		
	Value	Error
m1	5.8147	14.346
m2	0.026671	0.58886
Chisq	2529.5	NA
R	0.009058	NA

(b) BWRVIP

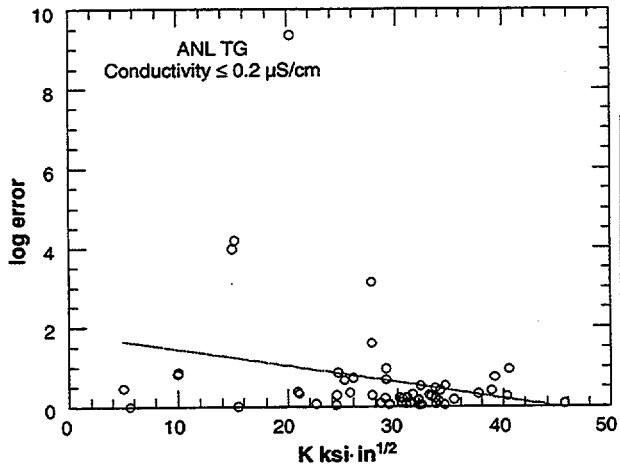

y = m1+m2*m0		
	Value	Error
m1	1.8539	0.55952
m2	-0.041025	0.019508
Chisq	117.15	NA
R	0.26833	NA

(c) ANL TGSCC

Figure 51. Variation of errors in PLEDGE predictions with EPR for the (a) Andresen, (b) ANL IGSCC (with adjusted EPR values), (c) BWRVIP, and (d) ANL TGSCC data sets

Table 18. Effect of EPR on mean difference between PLEDGE predictions of CGR and experimental measurements for screened BWRVIP data sets

	EPR 13–15 C/cm^2	EPR 20–30 C/cm^2
Upper 95% ME	2.3	6.3
ME	1.5	4.6
Lower 95% ME	0.9	3.4

Estimates of the effect of ECP were made by using the low-conductivity portions of the ANL TG and Andresen databases. These results are summarized in Table 19. No significant effect of ECP could be seen in the ANL TG data, but the results from the Andresen data suggest that the PLEDGE calculations are somewhat more conservative for very low and very high ECP.

Table 19. Effect of ECP on mean difference between PLEDGE predictions of CGR and experimental measurements for low-conductivity data in Andresen and ANL TG data sets

	Andresen ECP<–400	Andresen 53<ECP<140	Andresen ECP>140	ANL TG 75<ECP<140	ANL TG ECP>140
Upper 95% ME	1.6	0.8	1.5	0.3	0.4
ME	1.2	0.7	1.3	0.3	0.3
Lower 95% ME	0.9	0.6	1.2	0.2	0.3

Data from other sources were also examined to determine dependence on conductivity, sensitization, and ECP. The data of Kawakubo et al.[129] comparing crack growth rates in materials with EPR = 0 and 15 C/cm^2 are shown in Fig. 52(a), along with the corresponding PLEDGE predictions in Fig. 52(b). The prediction is about three times that observed at a stress intensity of K = 27 MPa·m$^{1/2}$. Data with EPR of 10–15 and 30 C/cm^2 used to develop the NRC disposition curve[130] are shown in Fig. 53(a), along with the corresponding PLEDGE predictions in Fig. 53(b). There is large scatter in the data, but nominally the difference is again about a factor of 3 at a stress intensity K = 27 MPa·m$^{1/2}$. These results are consistent with the results determined from the BWRVIP data, as shown in Table 18.

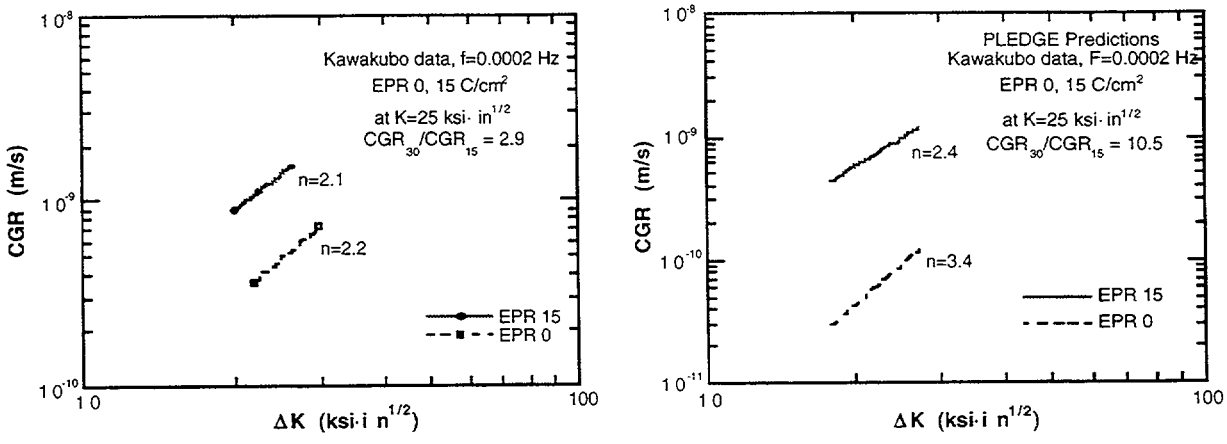

(a) (b)

Figure 52. (a) Effect of sensitization on CGR observed in cyclic load tests of Kawakubo et al.[129]; (b) PLEDGE prediction of change in CGR due to change in sensitization

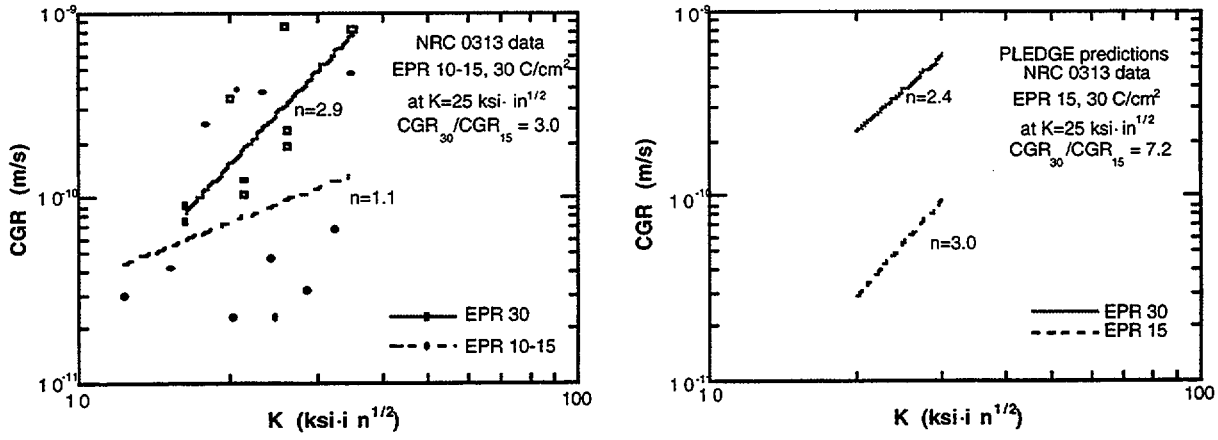

(a) (b)

Figure 53. (a) Effect of sensitization on CGR observed in cyclic load tests used for NRC disposition curve;[130] (b) PLEDGE prediction of change in CGR due to change in sensitization

Part of the reason that PLEDGE may overestimate the effect of sensitization might be found in the experimental models it uses to represent the material at the crack tip. In solution-annealed material, the crack tip is Fe-18Cr-8Ni, in weld-sensitized material it is Fe-8Cr-10Ni, and in furnace-sensitized material it is pure Fe.[120] The actual relation between the oxidation current densities measured on these materials and the dependency on EPR built into PLEDGE is part of the proprietary "black box," but such assumptions could well result in an overestimate of the effect of sensitization.

As noted from the examination of the databases, at high conductivities PLEDGE appears to predict a stronger dependence on conductivity than is observed. This is consistent with the results from a "controlled" experiment in which conductivity was systematically varied while keeping all other experimental parameters constant, as shown in Fig. 54. In application to operating reactors, conductivity as defined by PLEDGE should be a conservative representation of impurity effects. "Conductivity" is really used as a surrogate measure for harmful anions such as SO_4^{2-} and Cl^-; other anions may be much more benign. PLEDGE assumes that the conductivity is due to the "worst-case" impurity, i.e., sulfate.

The predicted dependence of CGR on ECP is shown in Figs. 55 and 56. In this case, the dependency is quite sensitive to the loading condition. Under R = 1 loading, the CGR essentially vanishes; under the R = 0.95 loading, the mechanically driven CGR places a floor on how low the rate can go and so the relative change is smaller. The reductions predicted by PLEDGE are difficult to verify experimentally because the CGRs so low that they are extremely difficult to measure. The much more modest reductions predicted by the BWRVIP model are probably skewed by unavailability and scatter in CGRs at such low levels. Many of the ANL tests in hydrogen water chemistries are not reported as CGRs, simply because they were so low that it would take an inordinate amount of time to obtain a valid CGR. However, Ruther and Kassner carried out a series of tests on a thermally aged cast SS,[141] which showed a high susceptibility to environmentally assisted cracking; these tests were continued until the CGRs could be measured with some confidence. Their measurements are shown in Fig. 55 and suggest that the BWRVIP model is very conservative at low ECPs, but that the PLEDGE model

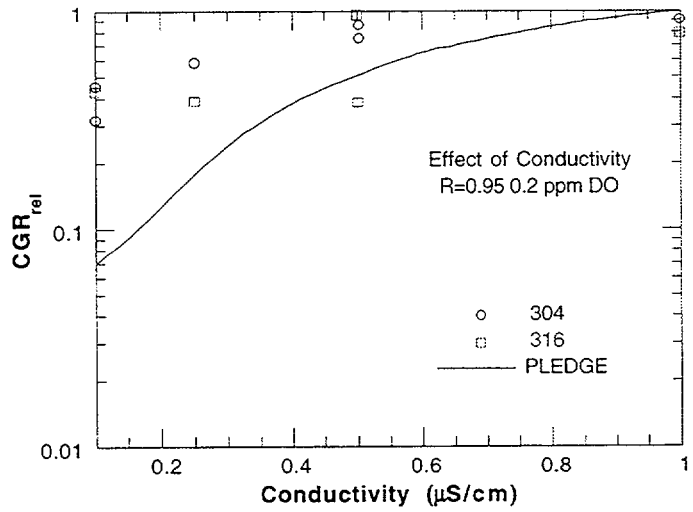

Figure 54. Predicted effect of variation in conductivity on CGR for R=0.95 loading. Data shown are from a controlled test in which conductivity was varied while all other variables were held constant

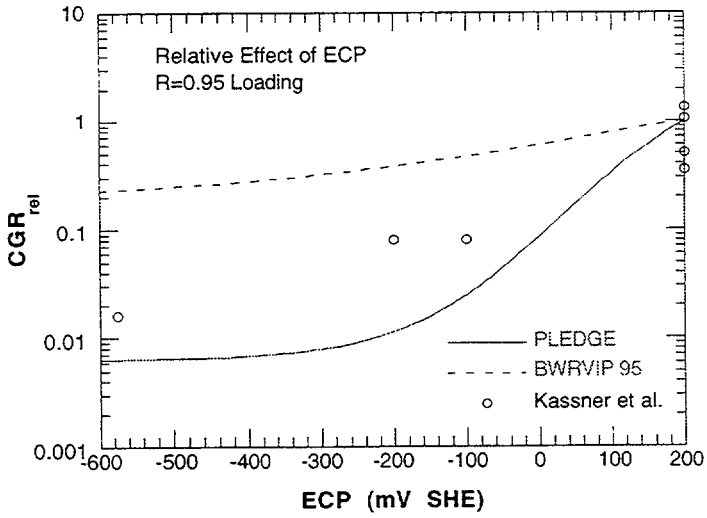

Figure 55. Predicted effect of variation in ECP on CGR for R=0.95 loading. Data shown are from a controlled test in which ECP was varied while all other variables were held constant.

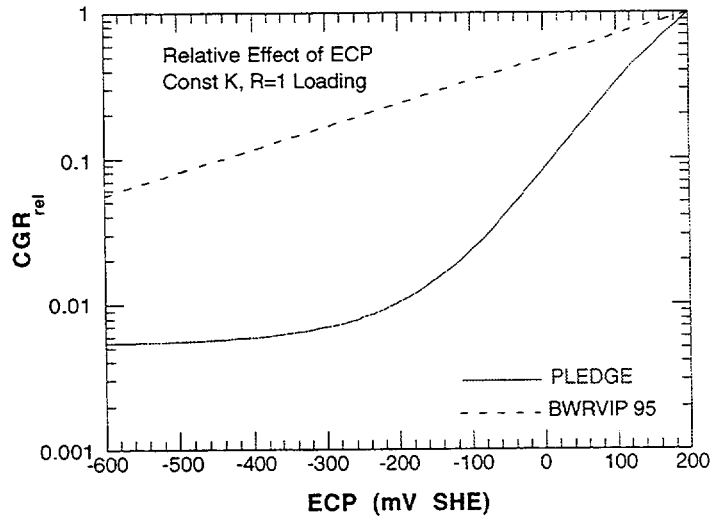

Figure 56. Predicted effect of variation in ECP on CGR for R=1 loading

predicts the overall trends reasonably well. These results, together with the results in Table 19 suggest that the PLEDGE model predicts the variation of the CGR with ECP fairly well overall, although it may overestimate somewhat the increases in CGR associated with increase in ECP above 140 mV.

6 Summary of Results

6.1 Environmental Effects on Fatigue S–N Behavior of Primary Pressure Boundary Materials

Both the design fatigue curve method and the fatigue life correction factor (F_{en}) method of evaluating fatigue lives are based on statistical models for estimating fatigue lives of carbon and low–alloy steels and austenitic SSs in LWR environments. Although estimates of fatigue lives based on these two methods may differ because of differences between the ASME mean curves used to develop the current design curves and the best–fit curves to the existing data used to develop the environmentally adjusted curves, either method provides an acceptable approach to account for environmental effects.

The environmentally adjusted design fatigue curves provide allowable cycles for fatigue crack initiation in LWR coolant environments. The new design curves maintain the margin of 20 on life. However, to be consistent with the current ASME Code curves, the margin on stress is 2 for carbon and low–alloy steels and 1.5 for austenitic SSs.

In the F_{en} method, environmental effects on life are estimated from the statistical models but the correction is applied to fatigue lives estimated from the current Code design curves. Therefore, fatigue life estimates based on the two methods may differ because of differences in the ASME mean curve and the best–fit curve to existing fatigue data. The current Code design curve for carbon steels is comparable to the statistical–model curve for LASs, whereas it is somewhat conservative at stress levels of <500 MPa when compared with the statistical–model curve for CSs. Consequently, usage factors based on the F_{en} method would be comparable to those based on the environmentally adjusted design fatigue curves for LASs and would be somewhat higher for CSs.

Figure 5 indicates that for austenitic SSs, the current Code design fatigue curve is nonconservative when compared with the statistical–model curve, i.e., it predicts longer fatigue lives than the best–fit curve to the existing S–N data. Consequently, usage factors that are based on the F_{en} method would be lower than those determined from the environmentally corrected design fatigue curves.

6.2 Irradiation–Assisted Stress Corrosion Cracking of Austenitic Stainless Steels

1. As fluence was increased from $\approx 0.3 \times 10^{21}$ n·cm^{-2} to $\approx 0.9 \times 10^{21}$ n·cm^{-2}, IGSCC fracture surfaces emerged in many alloys, usually in the middle of and surrounded by TGSCC fracture surfaces. This finding indicates that high susceptibility to TGSCC is a precursor to susceptibility to IGSCC at a higher fluence.

2. Alloy-to-alloy variations in susceptibility to TGSCC and IGSCC were significant at $\approx 0.9 \times 10^{21}$ n·cm^{-2}. Susceptibility to TGSCC and IGSCC was influenced by more than one alloying and impurity element in a complex manner.

3. Yield strength of the model alloys, measured in BWR-like water at 289°C, was nearly constant at ≈200 MPa in the unirradiated state and was more or less independent of Si concentration. However, as the alloys were irradiated to ≈0.3 x 10^{21} n·cm^{-2} and ≈0.9 x 10^{21} n·cm^{-2}, the degree of increase in yield strength was significantly lower for alloys that contain >0.9 wt.% Si than for alloys that contain <0.8 wt.% Si. This observation indicates that the nature of irradiation-induced hardening centers and the degree of irradiation hardening are significantly influenced by alloy Si content. Similar influence of C and N was not observed.

4. Among laboratory heats of Types 304 and 304L SS, alloys that contain <0.67 wt.% Si exhibited significant susceptibility to IGSCC, whereas heats with 0.8–1.5 wt.% Si exhibited negligible susceptibility to IGSCC. However, an alloy with ≈1.9 wt.% Si exhibited some degree of susceptibility to IGSCC. These observations indicate that an Si content between ≈0.8 and ≈1.5 wt.% is beneficial in delaying the onset of or suppressing susceptibility to IASCC.

6.3 Fracture Toughness J–R Test of Austenitic Stainless Steels Irradiated in the Halden Reactor

Fracture toughness J–R curve tests have been conducted on four heats of Type 304 stainless steel that were irradiated to fluence levels of ≈0.3 and 0.9 x 10^{21} n·cm^{-2} (E > 1 MeV) (≈0.45 and 1.35 dpa) at ≈288°C in an He environment in the Halden boiling heavy water reactor. The tests were performed on 1/4–T compact tension specimens in air at 288°C; crack extensions were determined by both DC potential and elastic unloading compliance techniques. Neutron irradiation at 288°C to 0.9 x 10^{21} n·cm^{-2} (E > 1 MeV) (1.35 dpa) decreased the fracture toughness of all of the steels. For these materials, minor differences in the chemical composition of the steels, e.g., differences in nickel content for Heats C16 and C19 or silicon content for heats L2 and L20, have little or no effect on the fracture toughness of irradiated steels. The commercial Heats C16 and C19 exhibited fracture toughness that is superior to the fracture toughness of laboratory Heats L20 and L2. For steels irradiated to 0.9 x 10^{21} n·cm^{-2} (E > 1 MeV) (1.35 dpa), the J_{IC} values are 299 and 304 kJ/m^2, respectively, for Heats C16 and C19, and 38 and 39 kJ/m^2, respectively, for Heats L2 and L20. The data from commercial heats fall within the scatter band for the data obtained at higher temperatures.

6.4 Environmentally Assisted Cracking of Low–Carbon Alloys 600 and 690 in Simulated LWR Water

To evaluate the resistance of Alloys 600 and 690 to EAC in LWR coolant environments, fracture mechanics CGR tests are being conducted in air and water environments on CT specimens of several heats of these alloys in annealed and in annealed and thermally treated conditions. During the current reporting period, existing fatigue crack growth data on Alloys 600 and 690 have been analyzed to establish the effects of temperature, load ratio, frequency, and stress intensity range ΔK on crack growth rates in air. Correlations have been developed for estimating the CGRs of Alloys 600 and 690 as a function of stress intensity range ΔK, load ratio R, and temperature. The results indicate that the CGRs of Alloys 600 and 690 in air are relatively insensitive to changes in frequency.

6.5 Assessment of Industry Crack-Growth Models

The basic physical description of stress corrosion cracking that underlies the PLEDGE model is consistent with the basic anodic dissolution model of SCC developed by Parkins and his colleagues for several decades. The detailed mathematical description of the model and the experimental data used to develop the correlations used in PLEDGE are proprietary. However, the acceptability of PLEDGE for modeling stress corrosion cracking behavior can be established by comparison with the extensive data on SCC in BWR environments available in the literature. Based on this comparison, it can be stated that PLEDGE provides conservative predictions of CGRs in unirradiated sensitized materials if an appropriate value is chosen for the EPR. For applications to unirradiated weldments, a value of 15 C/cm^2 appears appropriate and yields a moderate degree of conservatism. With this value for EPR, PLEDGE should give somewhat conservative predictions for IGSCC under constant and cyclic loads and should provide a conservative estimate for environmentally assisted fatigue, i.e., transgranular crack growth, that may occur under cyclic loading. For environmentally assisted fatigue in unsensitized materials, the choice of EPR = 0 C/cm^2 may not give conservative estimates in the low-conductivity water chemistries characteristic of current BWR operation. Some additional margin appears appropriate; this could be provided again by assuming EPR = 15 C/cm^2, although other approaches (e.g., an appropriate multiplier) could be used, but would have to be justified by comparison with appropriate data.

PLEDGE appears to overestimate the deleterious effect of impurity additions, and its predictions become more conservative for conductivities > 0.2 μS/cm. It also appears to overestimate the deleterious effect of sensitization as characterized by EPR, at least for EPR values > 20 C/cm^2. Because current BWRs generally operate with conductivities much lower than 0.2 $\mu S/cm^2$ and most weldments will have sensitization levels < 15 C/cm^2, these shortcomings of the model are of limited importance. However, it is important to recognize that comparing PLEDGE predictions with data for high conductivities or high EPR would give a misleading picture of the degree of conservatism in PLEDGE predictions. Thus, the implied conservatism in the values of the mean errors in Table 15 is misleading, and a more appropriate comparison with experimental data is provided by the results for the low-conductivity data given in Table 17.

The choice of an appropriate degree of conservatism in the development of a disposition curve is to some extent not a technical question. However, we believe that the use of a 95% confidence limit on the predictions is overly conservative. There is inevitable scatter in SCC measurements, and the focus should be on the main trends, not the scatter in the tails. The James and Jones approach of adopting a 95% confidence limit on the mean[139] has been adopted here as an appropriate method for comparing the model predictions with the experimental data.

References

1. C. E. Jaske and W. J. O'Donnell, *Fatigue Design Criteria for Pressure Vessel Alloys*, Trans. ASME J. Pressure Vessel Technol. **99**, 584–592 (1977).

2. O. K. Chopra, *Effects of LWR Coolant Environments on Fatigue Design Curves of Austenitic Stainless Steels*, NUREG/CR–5704, ANL–98/31 (1999).

3. S. Ranganath, J. N. Kass, and J. D. Heald, *Fatigue Behavior of Carbon Steel Components in High–Temperature Water Environments*, BWR Environmental Cracking Margins for Carbon Steel Piping, EPRI NP–2406, Electric Power Research Institute, Palo Alto, CA, Appendix 3 (1982).

4. M. Higuchi and K. Iida, *Fatigue Strength Correction Factors for Carbon and Low–Alloy Steels in Oxygen–Containing High–Temperature Water*, Nucl. Eng. Des. **129**, 293–306 (1991).

5. N. Nagata, S. Sato, and Y. Katada, *Low–Cycle Fatigue Behavior of Pressure Vessel Steels in High–Temperature Pressurized Water*, ISIJ Intl. **31** (1), 106–114 (1991).

6. W. A. Van Der Sluys, *Evaluation of the Available Data on the Effect of the Environment on the Low–Cycle Fatigue Properties in Light Water Reactor Environments*, in Proc. 6th Intl. Symp. on Environmental Degradation of Materials in Nuclear Power Systems – Water Reactors, R. E. Gold and E. P. Simonen, eds., The Metallurgical Society, Warrendale, PA, pp. 1–4 (1993).

7. H. Kanasaki, M. Hayashi, K. Iida, and Y. Asada, *Effects of Temperature Change on Fatigue Life of Carbon Steel in High–Temperature Water*, in Fatigue and Crack Growth: Environmental Effects, Modeling Studies, and Design Considerations, PVP Vol. 306, S. Yukawa, ed., American Society of Mechanical Engineers, New York, pp. 117–122 (1995).

8. G. Nakao, H. Kanasaki, M. Higuchi, K. Iida, and Y. Asada, *Effects of Temperature and Dissolved Oxygen Content on Fatigue Life of Carbon and Low–Alloy Steels in LWR Water Environment*, in Fatigue and Crack Growth: Environmental Effects, Modeling Studies, and Design Considerations, PVP Vol. 306, S. Yukawa, ed., American Society of Mechanical Engineers, New York, pp. 123–128 (1995).

9. M. Higuchi, K. Iida, and Y. Asada, *Effects of Strain Rate Change on Fatigue Life of Carbon Steel in High–Temperature Water*, in Effects of the Environment on the Initiation of Crack Growth, ASTM STP 1298, W. A. Van Der Sluys, R. S. Piascik, and R. Zawierucha, eds., American Society for Testing and Materials, Philadelphia, pp. 216–231 (1997).

10. O. K. Chopra and W. J. Shack, *Evaluation of Effects of LWR Coolant Environments on Fatigue Life of Carbon and Low–Alloy Steels*, in Effects of the Environment on the Initiation of Crack Growth, ASTM STP 1298, W. A. Van Der Sluys, R. S. Piascik, and R. Zawierucha, eds., American Society for Testing and Materials, Philadelphia, pp. 247–266 (1997).

11. O. K. Chopra and W. J. Shack, *Low-Cycle Fatigue of Piping and Pressure Vessel Steels in LWR Environments*, Nucl. Eng. Des. **184**, 49–76 (1998).

12. O. K. Chopra and W. J. Shack, *Effects of LWR Coolant Environments on Fatigue Design Curves of Carbon and Low-Alloy Steels*, NUREG/CR-6583, ANL-97/18 (March 1998).

13. O. K. Chopra and W. J. Shack, *Fatigue Crack Initiation in Carbon and Low-Alloy Steels in Light Water Reactor Environments – Mechanism and Prediction*, in Fatigue, Environmental Factors, and New Materials, PVP Vol. 374, H. S. Mehta, R. W. Swindeman, J. A. Todd, S. Yukawa, M. Zako, W. H. Bamford, M. Higuchi, E. Jones, H. Nickel, and S. Rahman, eds., American Society of Mechanical Engineers, New York, pp. 155–168 (1998).

14. O. K. Chopra and W. J. Shack, *Overview of Fatigue Crack Initiation in Carbon and Low-Alloy Steels in Light Water Reactor Environments*, J. Pressure Vessel Technol. **121**, 49–60 (1999).

15. M. Fujiwara, T. Endo, and H. Kanasaki, *Strain Rate Effects on the Low-Cycle Fatigue Strength of 304 Stainless Steel in High-Temperature Water Environment; Fatigue Life: Analysis and Prediction*, in Proc. Intl. Conf. and Exposition on Fatigue, Corrosion Cracking, Fracture Mechanics, and Failure Analysis, ASM, Metals Park, OH, pp. 309–313 (1986).

16. H. Mimaki, H. Kanasaki, I. Suzuki, M. Koyama, M. Akiyama, T. Okubo, and Y. Mishima, *Material Aging Research Program for PWR Plants*, in Aging Management Through Maintenance Management, PVP Vol. 332, I. T. Kisisel, ed., American Society of Mechanical Engineers, New York, pp. 97–105 (1996).

17. M. Higuchi and K. Iida, *Reduction in Low-Cycle Fatigue Life of Austenitic Stainless Steels in High-Temperature Water*, in Pressure Vessel and Piping Codes and Standards, PVP Vol. 353, D. P. Jones, B. R. Newton, W. J. O'Donnell, R. Vecchio, G. A. Antaki, D. Bhavani, N. G. Cofie, and G. L. Hollinger, eds., American Society of Mechanical Engineers, New York, pp. 79–86 (1997).

18. H. Kanasaki, R. Umehara, H. Mizuta, and T. Suyama, *Fatigue Lives of Stainless Steels in PWR Primary Water*, Trans. 14th Intl. Conf. on Structural Mechanics in Reactor Technology (SMiRT 14), Lyon, France, pp. 473–483 (1997).

19. H. Kanasaki, R. Umehara, H. Mizuta, and T. Suyama, *Effects of Strain Rate and Temperature Change on the Fatigue Life of Stainless Steel in PWR Primary Water*, Trans. 14th Intl. Conf. on Structural Mechanics in Reactor Technology (SMiRT 14), Lyon, France, pp. 485–493 (1997).

20. M. Hayashi, *Thermal Fatigue Strength of Type 304 Stainless Steel in Simulated BWR Environment*, Nucl. Eng. Des. **184**, 135–144 (1998).

21. M. Hayashi, K. Enomoto, T. Saito, and T. Miyagawa, *Development of Thermal Fatigue Testing with BWR Water Environment and Thermal Fatigue Strength of Austenitic Stainless Steels*, Nucl. Eng. Des. **184**, 113–122 (1998).

22. O. K. Chopra and D. J. Gavenda, *Effects of LWR Coolant Environments on Fatigue Lives of Austenitic Stainless Steels*, in Pressure Vessel and Piping Codes and Standards, PVP Vol. 353, D. P. Jones, B. R. Newton, W. J. O'Donnell, R. Vecchio, G. A. Antaki, D. Bhavani, N. G. Cofie, and G. L. Hollinger, eds., American Society of Mechanical Engineers, New York, pp. 87–97 (1997).

23. O. K. Chopra and D. J. Gavenda, *Effects of LWR Coolant Environments on Fatigue Lives of Austenitic Stainless Steels*, J. Pressure Vessel Technol. **120**, 116–121 (1998).

24. O. K. Chopra and J. L. Smith, *Estimation of Fatigue Strain–Life Curves for Austenitic Stainless Steels in Light Water Reactor Environments*, in Fatigue, Environmental Factors, and New Materials, PVP Vol. 374, H. S. Mehta, R. W. Swindeman, J. A. Todd, S. Yukawa, M. Zako, W. H. Bamford, M. Higuchi, E. Jones, H. Nickel, and S. Rahman, eds., American Society of Mechanical Engineers, New York, pp. 249–259 (1998).

25. S. Majumdar, O. K. Chopra, and W. J. Shack, *Interim Fatigue Design Curves for Carbon, Low–Alloy, and Austenitic Stainless Steels in LWR Environments*, NUREG/CR–5999, ANL–93/3 (1993).

26. J. Keisler, O. K. Chopra, and W. J. Shack, 1995, "Fatigue Strain–Life Behavior of Carbon and Low–Alloy Steels, Austenitic Stainless Steels, and Alloy 600 in LWR Environments," NUREG/CR–6335, ANL–95/15.

27. J. Keisler, O. K. Chopra, and W. J. Shack, 1996, *Fatigue Strain–Life Behavior of Carbon and Low–Alloy Steels, Austenitic Stainless Steels, and Alloy 600 in LWR Environments*, Nucl. Eng. Des. **167**, pp. 129–154.

28. A. G. Ware, D. K. Morton, and M. E. Nitzel, 1995, *Application of NUREG/CR–5999 Interim Design Curves to Selected Nuclear Power Plant Components*, NUREG/CR–6260, INEL–95/0045.

29. H. S. Mehta and S. R. Gosselin, 1996, *An Environmental Factor Approach to Account for Reactor Water Effects in Light Water Reactor Pressure Vessel and Piping Fatigue Evaluations, Fatigue and Fracture Volume 1*, PVP Vol. 323, H. S. Mehta, ed., American Society of Mechanical Engineers, New York, pp. 171–185.

30. H. S. Mehta and S. R. Gosselin, 1998, *Environmental Factor Approach to Account for Water Effects in Pressure Vessel and Piping Fatigue Evaluations*, Nucl. Eng. Des. **181**, pp. 175–197.

31. M. Higuchi, 1996, presented at Working Group Meeting on S–N Data Analysis, the Pressure Vessel Research Council, April, Orlando, FL.

32. K. J Miller, 1985, *Initiation and Growth Rates of Short Fatigue Cracks*, Fundamentals of Deformation and Fracture, Eshelby Memorial Symposium, Cambridge University Press, Cambridge, U.K., pp. 477–500.

33. K. Tokaji, T. Ogawa, and S. Osaka, 1988, *The Growth of Microstructurally Small Fatigue Cracks in a Ferrite–Pearlite Steel*, Fatigue Fract. Engng. Mater. Struct. **11**, pp. 311–342.

34. D. J. Gavenda, P. R. Luebbers, and O. K. Chopra, 1997, *Crack Initiation and Crack Growth Behavior of Carbon and Low-Alloy Steels*, Fatigue and Fracture 1, Vol. **350**, S. Rahman, K. K. Yoon, S. Bhandari, R. Warke, and J. M. Bloom, eds., American Society of Mechanical Engineers, New York, pp. 243–255.

35. K. Obrtlik, J. Polák, M. Hájek, and A. Vasek, 1997, *Short Fatigue Crack Behaviour in 316L Stainless Steel*, Intl. J. Fatigue **19**, pp. 471–475.

36. S. G. Sundara Raman, D. Argence, and A. Pineau, 1997, *High Temperature Short Fatigue Crack Behaviour in a Stainless Steel*, Fatigue Fract. Engng. Mater. Struct. **20**, pp. 1015–1031.

37. K. J. Miller, 1995, "Damage in Fatigue: A New Outlook," *International Pressure Vessels and Piping Codes and Standards: Volume 1 – Current Applications*, PVP Vol. 313–1, K. R. Rao and Y. Asada, eds., American Society of Mechanical Engineers, New York, pp. 191–192.

38. F. P. Ford, 1986, *Overview of Collaborative Research into the Mechanisms of Environmentally Controlled Cracking in the Low Alloy Pressure Vessel Steel/Water System*, Proc. 2nd Int. Atomic Energy Agency Specialists' Meeting on Subcritical Crack Growth, NUREG/CP-0067, MEA-2090, Vol. 2, pp. 3–71.

39. H. Hänninen, K. Törrönen, and W. H. Cullen, 1986, *Comparison of Proposed Cyclic Crack Growth Mechanisms of Low Alloy Steels in LWR Environments*, Proc. 2nd Int. Atomic Energy Agency Specialists' Meeting on Subcritical Crack Growth, NUREG/CP-0067, MEA-2090, Vol. 2, pp. 73–97.

40. J. L. Smith, and O. K. Chopra, 1999, *Crack Initiation in Smooth Fatigue Specimens of Austenitic Stainless Steel in Light Water Reactor Environments*, Operations, Applications, and Components – 1999, PVP Vol. 395, I. T. Kisisel, ed., American Society of Mechanical Engineers, New York, pp. 235–242.

41. Y. Katada, N. Nagata, and S. Sato, 1993, *Effect of Dissolved Oxygen Concentration on Fatigue Crack Growth Behavior of A533 B Steel in High-Temperature Water*, ISIJ Intl. **33** (8), pp. 877–883.

42. M. Higuchi, 1995, presented at Working Group Meeting on S–N Data Analysis, the Pressure Vessel Research Council, June, Milwaukee.

43. S. Yukawa, 1999, Meeting of the Steering Committee for Cyclic Life and Environmental Effects (CLEE), the Pressure Vessel Research Council, June, Columbus, OH.

44. H. S. Mehta, 1999, *An Update on the EPRI/GE Environmental Fatigue Evaluation Methodology and its Applications*, Probabilistic and Environmental Aspects of Fracture and Fatigues, PVP Vol. 386, S. Rahman, ed., American Society of Mechanical Engineers, New York, pp. 183–193.

45. V. Pasupathi and R. W. Klingensmith, *Investigation of Stainless Steel Clad Fuel Rod Failures and Fuel Performance in the Connecticut Yankee Reactor*, EPRI NP-2119, 1981, Electric Power Research Institute, Palo Alto, CA (1981).

46. F. Garzarolli, D. Alter, P. Dewes, and J. L. Nelson, *Deformability of Austenitic Stainless Steels and Ni-Base Alloys in the Core of a Boiling and Pressurized Water Reactor*, in Proc. 3rd Int. Symp. on Environmental Degradation of Materials in Nuclear Power Systems - Water Reactors, G. J. Theus and J. R. Weeks, eds., The Metallurgical Society, Warrendale, PA, pp. 657-664 (1993).

47. A. J. Jacobs, G. P. Wozadlo, K. Nakata, T. Yoshida, and I. Masaoka, *Radiation Effects on the Stress Corrosion and Other Selected Properties of Type-304 and Type-316 Stainless Steels*, in Proc. 3rd Int. Symp. on Environmental Degradation of Materials in Nuclear Power Systems – Water Reactors, G. J. Theus and J. R. Weeks, eds., The Metallurgical Society, Warrendale, PA, 1988, p. 673-680.

48. M. P. Manahan, R. Kohli, J. Santucci, and P. Sipushi, *A Phenomenological Investigation of In-Reactor Cracking of Type 304 Stainless Steel Control Rod Cladding*, Nucl. Eng. Design **113** (1989) 297-321.

49. R. Katsura, M. Kodama, and S. Nishimura, *DL-EPR Study of Neutron Irradiation in Type 304 Stainless Steel*, Corrosion **48** (1992) 384-390.

50. S. M. Bruemmer, L. A. Charlot, and E. P. Simpson, *Irradiation-Induced Chromium Depletion and Its Influence on Intergranular Stress Corrosion Cracking of Stainless Steels*, in Proc. 5th Int. Symp. on Environmental Degradation of Materials in Nuclear Power Systems – Water Reactors, D. Cubicciotti, E. P. Simonen, and R. Gold, eds., American Nuclear Society, La Grange Park, IL, 1992, pp. 821-826.

51. A. J. Jacobs, G. E. C. Bell, C. M. Shepherd, and G. P. Wozadlo, *High-Temperature Solution Annealing as an IASCC Mitigating Technique*, in Proc. 5th Int. Symp. on Environmental Degradation of Materials in Nuclear Power Systems – Water Reactors, D. Cubicciotti, E. P. Simonen, and R. Gold, eds., American Nuclear Society, La Grange Park, IL, 1992, pp. 917-934.

52. M. E. Indig, J. L. Nelson, and G. P. Wozadlo, *Investigation of Protection Potential against IASCC*, in Proc. 5th Int. Symp. on Environmental Degradation of Materials in Nuclear Power Systems – Water Reactors, D. Cubicciotti, E. P. Simonen, and R. Gold, eds., American Nuclear Society, La Grange Park, IL, 1992, p. 941-947.

53. M. Kodama, S. Nishimura, J. Morisawa, S. Shima, S. Suzuki, and M. Yamamoto, *Effects of Fluence and Dissolved Oxygen on IASCC in Austenitic Stainless Steels*, in Proc. 5th Int. Symp. on Environmental Degradation of Materials in Nuclear Power Systems – Water Reactors, D. Cubicciotti, E. P. Simonen, and R. Gold, eds., American Nuclear Society, La Grange Park, IL, 1992, p. 948-954.

54. H. M. Chung, W. E. Ruther, J. E. Sanecki, A. G. Hins, and T. F. Kassner, *Stress Corrosion Cracking Susceptibility of Irradiated Type 304 Stainless Steels*, in Effects of Radiation on Materials: 16th Int. Symp., ASTM STP 1175, A. S. Kumar, D. S. Gelles, R. K. Nanstad, and T. A. Little, eds., American Society for Testing and Materials, Philadelphia, 1993, pp. 851-869.

55. M. Kodama, K. Fukuya, and H. Kayano, *The Relationship of Grain Boundary Composition in Irradiated Type 304 SS to Neutron Fluence and IASCC*, in Effects of Radiation on Materials: 16th Int. Symp., ASTM STP 1175, A. S. Kumar, D. S. Gelles, R. K. Nanstad, and T. A. Little, eds., American Society for Testing and Materials, Philadelphia, 1993, pp. 889-901.

56. A. J. Jacobs, *Influence of Impurities and Alloying Elements on IASCC in Neutron Irradiated Austenitic Stainless Steels*, in Effects of Radiation on Materials: 16th Int. Symp., ASTM STP 1175, A. S. Kumar, D. S. Gelles, R. K. Nanstad, and T. A. Little, eds., American Society for Testing and Materials, Philadelphia, 1993, pp. 902-918.

57. R. D. Carter, D. L. Damcott, M. Atzmon, G. S. Was, S. M. Bruemmer, and E. A. Kenik, *Capabilities and Limitations of Analytical Methods Used to Measure Radiation Induced Grain Boundary Segregation*, in Proc. 6th Int. Symp. on Environmental Degradation of Materials in Nuclear Power Systems - Water Reactors, R. E. Gold and E. P. Simonen, eds., The Minerals, Metals, and Materials Society, Warrendale, PA, 1993, pp. 501-509.

58. H. M. Chung, W. E. Ruther, J. E. Sanecki, and T. F. Kassner, *Grain-Boundary Microchemistry and Intergranular Cracking of Irradiated Austenitic Stainless Steels*, in Proc. 6th Int. Symp. on Environmental Degradation of Materials in Nuclear Power Systems - Water Reactors, R. E. Gold and E. P. Simonen, eds., The Minerals, Metals, and Materials Society, Warrendale, PA, 1993, pp. 511-519.

59. S. M. Bruemmer, J. I. Cole, J. L. Brimhall, R. D. Carter, and G. S. Was, *Radiation Hardening Effects on Localized Deformation and Stress Corrosion Cracking of Stainless Steels*, in Proc. 6th Int. Symp. on Environmental Degradation of Materials in Nuclear Power Systems - Water Reactors, R. E. Gold and E. P. Simonen, eds., The Minerals, Metals, and Materials Society, Warrendale, PA, 1993, pp. 537-545.

60. K. Fukuya, S. Shima, K. Nakata, S. Kasahara, A. J. Jacobs, G. P. Wozadlo, S. Suzuki, and M. Kitamura, *Mechanical Properties and IASCC Susceptibility in Irradiated Stainless Steels*, in Proc. 6th Int. Symp. on Environmental Degradation of Materials in Nuclear Power Systems - Water Reactors, R. E. Gold and E. P. Simonen, eds., The Minerals, Metals, and Materials Society, Warrendale, PA, 1993, pp. 564-572.

61. J. L. Cookson, D. L. Damcott, G. W. Was, and P. L. Andresen, *The Role of Microchemical and Microstructural Effects in the IASCC of High-Purity Austenitic Stainless Steels*, in Proc. 6th Int. Symp. on Environmental Degradation of Materials in Nuclear Power Systems - Water Reactors, R. E. Gold and E. P. Simonen, eds., The Minerals, Metals, and Materials Society, Warrendale, PA, 1993, pp. 573-580.

62. K. Kodama, R. Katsura, J. Morisawa, S. Nishimura, S. Suzuki, K. Asano, K. Fukuya, and K. Nakata, *IASCC Susceptibility of Austenitic Stainless Steels Irradiated to High Neutron Fluence*, Proc. 6th Int. Symp. on Environmental Degradation of Materials in Nuclear Power Systems - Water Reactors, R. E. Gold and E. P. Simonen, eds., The Minerals, Metals, and Materials Society, Warrendale, PA, 1993, pp. 583-588.

63. A. J. Jacobs, G. P. Wozadlo, K. Nakata, S. Kasahara, T. Okada, S. Kawano, and S. Suzuki, *The Correlation of Grain Boundary Composition in Irradiated Stainless Steel with IASCC Resistance*, in Proc. 6th Int. Symp. on Environmental Degradation of Materials in Nuclear Power Systems - Water Reactors, R. E. Gold and E. P. Simonen, eds., The Minerals, Metals, and Materials Society, Warrendale, PA, 1993, pp. 597-606.

64. F. Garzarolli, P. Dewes, R. Hahn, and J. L. Nelson, *Deformability of High-Purity Stainless Steels and Ni-Base Alloys in the Core of a PWR*, in Proc. 6th Int. Symp. on Environmental Degradation of Materials in Nuclear Power Systems - Water Reactors, R. E. Gold and E. P. Simonen, eds., The Minerals, Metals, and Materials Society, Warrendale, PA, 1993, pp. 607-613.

65. S. Kasahara, K. Nakata, K. Fukuya, S. Shima, A. J. Jacobs, G. P. Wozadlo, and S. Suzuki, *The Effects of Minor Elements on IASCC Susceptibility in Austenitic Stainless Steels Irradiated with Neutrons*, in Proc. 6th Int. Symp. on Environmental Degradation of Materials in Nuclear Power Systems - Water Reactors, R. E. Gold and E. P. Simonen, eds., The Minerals, Metals, and Materials Society, Warrendale, PA, 1993, pp. 615-623.

66. M. Kodama, J. Morisawa, S. Nishimura, K. Asano, S. Shima, and K. Nakata, *Stress Corrosion Cracking and Intergranular Corrosion of Austenitic Stainless Steels Irradiated at 323 K*, J. Nucl. Mater., **1509** (1994) pp. 212–215.

67. T. Tsukada and Y. Miwa, *Stress Corrosion Cracking of Neutron Irradiated Stainless Steels*, in Proc. 7th Int. Symp. on Environmental Degradation of Materials in Nuclear Power Systems - Water Reactors, NACE International, Houston, 1995, pp. 1009–1018.

68. A. Jenssen and L. G. Ljungberg, *Irradiation Assisted Stress Corrosion Cracking - Postirradiation CERT Tests of Stainless Steels in a BWR Test Loop*, in Proc. 7th Int. Symp. on Environmental Degradation of Materials in Nuclear Power Systems - Water Reactors, NACE International, Houston, 1995, 1043–1052.

69. F. Garzarolli, P. Dewes, R. Hahn, and J. L. Nelson, *In-Reactor Testing of IASCC Resistant Stainless Steels*, in Proc. 7th Int. Symp. on Environmental Degradation of Materials in Nuclear Power Systems - Water Reactors, NACE International, Houston, 1995, 1055–1065.

70. H. M. Chung, W. E. Ruther, J. E. Sanecki, A. G. Hins, and T. F. Kassner, *Effects of Water Chemistry on Intergranular Cracking of Irradiated Austenitic Stainless Steels*, in Proc. 7th Int. Symp. on Environmental Degradation of Materials in Nuclear Power Systems - Water Reactors, NACE International, Houston, 1995, p. 1133-1143.

71. K. Hide, T. Onchi, M. Mayazumi, K. Dohi, and Y. Futamura, *Intergranular Cracking of Irradiated Thermally Sensitized Type 304 Stainless Steel in High-Temperature Water and Inert Gas*, Corrosion **51** (1995) 757-766.

72. H. M. Chung, W. E. Ruther, J. E. Sanecki, A. G. Hins, N. J. Zaluzec, and T. F. Kassner, *Irradiation-Assisted Stress Corrosion Cracking of Austenitic Stainless Steels: Recent Progress and New Approaches*, J. Nucl. Mater., **239** (1996) 61.

73. H. Kanasaki, T. Okubo, I. Satoh, M. Koyama, T. R. Mager, and R. G. Lott, *Fatigue and Stress Corrosion Cracking Behaviors of Irradiated Stainless Steels in PWR Primary Water*, in Proc. 5th Int. Conf. on Nuclear Engineering, May 26-30, 1997, Nice, France.

74. T. Tsukada, Y. Miwa, H. Nakajima, and T. Kondo, *Effects of Minor Elements on IASCC of Type 316 Model Stainless Steels*, in Proc. 8th Int. Symp. on Environmental Degradation of Materials in Nuclear Power Systems - Water Reactors, Aug. 10-14, 1997, Amelia Island, FL, S. M. Bruemmer, ed., American Nuclear Society, La Grange Park, IL, 1997, pp. 795-802.

75. T. Yonezawa, K. Fujimoto, H. Kanasaki, T. Iwamura, S. Nakada, K. Ajiki, and K. Sakai, *SCC Susceptibility of Irradiated Austenitic Stainless Steels for PWR*, in Proc. 8th Int. Symp. on Environmental Degradation of Materials in Nuclear Power Systems - Water Reactors, Aug. 10-14, 1997, Amelia Island, FL, S. M. Bruemmer, ed., American Nuclear Society, La Grange Park, IL, 1997, pp. 823-830.

76. M. Kodama, S. Nishimura, Y. Tanaka, S. Suzuki, K. Fukuya, S. Shima, K. Nakata, and T. Kato, *Mechanical Properties of Various Kinds of Irradiated Austenitic Stainless Steels*, in Proc. 8th Int. Symp. on Environmental Degradation of Materials in Nuclear Power Systems - Water Reactors, Aug. 10-14, 1997, Amelia Island, FL, S. M. Bruemmer, ed., American Nuclear Society, La Grange Park, IL, 1997, pp. 831-838.

77. H. M. Chung, J.-H. Park, W. E. Ruther, J. E. Sanecki, R. V. Strain, and N. J. Zaluzec, *Fabrication-Related Impurity Contamination and Stress Corrosion Cracking of Austenitic Stainless Steel Core-Internal Components*, in Proc. 8th Int. Symp. on Environmental Degradation of Materials in Nuclear Power Systems - Water Reactors, Aug. 10-14, 1997, Amelia Island, FL, S. M. Bruemmer, ed., American Nuclear Society, La Grange Park, IL, 1997, pp. 846-856.

78. J. M. Cookson, G. S. Was, and P. L. Andresen, *Oxide-Induced Initiation of Stress Corrosion Cracking in Irradiated Stainless Steels*, Corrosion **54** (1998) 299.

79. H. M. Chung, W. E. Ruther, and R. V. Strain, *Slow Strain Rate Tensile Testing of Model Austenitic Stainless Steels Irradiated in the Halden Reactor*, in Environmentally Assisted Cracking in Light Water Reactors, Semiannual Report, July-December 1998, NUREG/CR-4667, Vol. 27, ANL-99/11, pp. 28-38 (Oct. 1999).

80. H. M. Chung, W. E. Ruther, and R. V. Strain, *Slow Strain Rate Tensile Test of Model Austenitic Stainless Steels Irradiated in the Halden Reactor*, in Environmentally Assisted Cracking in Light Water Reactors, Semiannual Report, January-June 1999, NUREG/CR-4667, Vol. 28, ANL-00/7, pp. 14-17 (July 2000).

81. G. Taguchi, in Quality Engineering Using Robust Design, M. S. Phadke, ed., Prentice Hall, Englewood Cliffs, NJ, 1989.

82. S. M. Bruemmer et al., *Critical Issue Reviews for the Understanding and Evaluation of Irradiation-Assisted Stress Corrosion Cracking*, EPRI TR-107159, Electric Power Research Institute, Palo Alto, CA (1996).

83. M. L. Herrera, et al., *Evaluation of the Effects of Irradiation on the Fracture Toughness of BWR Internal Components*, in Proc. ASME/JSME 4th Intl. Conf. on Nucl. Eng. (ICONE–4) Vol. 5, A. S. Rao, R. M. Duffey, and D. Elias, eds., American Society of Mechanical Engineers, New York, pp. 245–251 (1996).

84. W. J. Mills, *Fracture Toughness of Type 304 and 316 Stainless Steels and their Welds*, Intl. Mater. Rev. **42**, 45–82 (1997).

85. P. J. Maziasz and C. J. McHargue, *Microstructural Evolution in Annealed Austenitic Steels during Neutron Irradiation*, Int. Met. Rev. **32**, 190 (1987).

86. P. J. Maziasz, *Overview of Microstructural Evolution in Neutron–Irradiated Austenitic Stainless Steels*, J. Nucl. Mater. **205**, 118–145 (1993).

87. F. A. Garner, *Evolution of Microstructures in Face–Centered Cubic Metals during Neutron Irradiation*, J. Nucl. Mater. **205**, 98–111 (1993).

88. J. Dufresne, B. Henry, and H. Larsson, *Fracture Toughness of Irradiated AISI 304 and 316L Stainless Steels*, in Effects of Radiation on Structural Materials, ASTM STP 683, J. A. Sprague and D. Kramer, eds., American Society for Testing and Materials, Philadelphia, pp. 511–528 (1979).

89. C. Picker, A. L. Stott, and H. Cocks, H., *Effects of Low–Dose Fast Neutron Irradiation on the Fracture Toughness of Type 316 Stainless Steel and Weld Metal*, in Proc. Specialists Meeting on Mechanical Properties of Fast Reactor Structural Materials, Chester, UK, Paper IWGFR 49/440–4 (1983).

90. F. H. Huang, *The Fracture Characterization of Highly Irradiated Type 316 Stainless Steel*, Int. J. Fracture **25**, 181–193 (1984).

91. J. Bernard and G. Verzeletti, *Elasto–Plastic Fracture Mechanics Characterization of Type 316H Irradiated Stainless Steel up to 1 dpa*, in Effects of Radiation on Materials: 12th Intl. Symp., ASTM STP 870, F. A. Garner and J. S. Perrin, eds., American Society for Testing and Materials, Philadelphia, pp. 619–641 (1985).

92. W. J. Mills, L. A. James, and L. D. Blackburn, 1985, *Results of Fracture Mechanics Tests on PNC SU 304 Plate*, Westinghouse Hanford Report HEDL–7544, Hanford Engineering Development Laboratory, Richland, WA.

93. W. J. Mills, *Fracture Toughness of Irradiated Stainless Steel Alloys*, Nucl. Technol. **82**, 290–303 (1988).

94. D. J. Michel and R. A. Gray, 1987, *Effects of Irradiation on the Fracture Toughness of FBR Structural Materials*, J. Nucl. Mater. **148**, 194–203 (1987).

95. P. Ould, P. Balladon, and Y. Meyzaud, *Bull. Cercle Etud. Metaux* **15**, 31.1–31.12 (1988).

96. E. V. Van Osch, M. G. Horsten, and M. I. De Vries, *Fracture Toughness of PWR Internals*, ECN Contribution to CEC Contract on PWR Internals–Part 2 (ETNU/CT/94/0136–F), ECN–I–97–010 (71747/NUC/EvO/mh/006274), Netherlands Energy Research Foundation ECN, Petten, the Netherlands (1997).

97. T. H. Hughes and E. E. Gruber, *Development of Hot–Cell J–R Test Facility*, in Environmentally Assisted Cracking in Light Water Reactors Semiannual Report July 1996–December 1996, NUREG/CR–4667, Vol. 23, ANL–97/10, pp. 42–52 (1997).

98. E. E. Gruber and O. K. Chopra, *Fracture Toughness J–R Test of Austenitic Stainless Steels Irradiated in Halden Reactor*, in Environmentally Assisted Cracking in Light Water Reactors Semiannual Report July 1998–December 1998, NUREG/CR–4667, Vol. 27, ANL–99/11, pp. 39–45 (Oct. 1999).

99. A. L. Hiser, *Fracture Toughness Chracterization of Nuclear Piping Steels*, NUREG/CR–5118, MEA–2325, Materials Engineering Associates, Inc., Lanham, MD (1989).

100. G. M. Wilkowski, et al., *Degraded Piping Program – Phase II, Semiannual Report*, NUREG/CR–4082, Vol. 2 (1985).

101. Mills, W. J., 1988b, *Heat–to–Heat Variations in the Fracture Toughness of Austenitic Stainless Steels*, Eng. Fracture Mech. **30**, pp. 469–492.

102. M. G. Vassilaros, R. A. Hays, and J. P. Gudas, *Investigation of the Ductile Fracture Properties of Type 304 Stainless Steel Plate, Welds, and 4–Inch Pipe*, in Proc. 12th Water Reactor Safety Information Meeting, NUREG/CP–0058, Vol. 4, U.S. Nuclear Regulatory Commission, pp. 176–189 (1985).

103. G. Kharshafdjian and A. H. Park, *PVRC Alloy 600 Fatigue Growth Rate Module*, CD-ROM File DADN600.XLS (Sept. 1999).

104. W. E. Ruther, W. K. Soppet, and T. F. Kassner, *Corrosion Fatigue of Alloys 600 and 690 in Simulated LWR Water*, NUREG/CR–6383, ANL–95/37 (April 1996).

105. W. E. Ruther, W. K. Soppet, and T. F. Kassner, *Environmentally Assisted Cracking of Alloys 600 and 690 in Simulated LWR Water*, in Environmentally Assisted Cracking in Light Water Reactors, Semiannual Report, July 1997–December 1997, NUREG/CR–4667 Vol. 25, ANL–98/18, pp. 42–75 (Sept. 1998).

106. W. E. Ruther, W. K. Soppet, T. F. Kassner, and W. J. Shack, *Environmentally Assisted Cracking of Alloys 600 and 690 in Simulated LWR Water*, in Environmentally Assisted Cracking in Light Water Reactors, Semiannual Report, January 1998–June 1998, NUREG/CR–4667 Vol. 26, ANL–98/18, pp. 25–32 (March 1999).

107. W. E. Ruther, W. K. Soppet, T. F. Kassner, and W. J. Shack, *Environmentally Assisted Cracking of Alloys 600 and 690 in Simulated LWR Water*, in Environmentally Assisted Cracking in Light Water Reactors, Semiannual Report, July 1998–December 1998, NUREG/CR–4667 Vol. 27, ANL–99/11, pp. 45–54 (Oct. 1999).

108. L. A. James, *Fatigue Crack Propagation Behavior of Inconel 600,* Int. J. Pres. Vessels and Piping, Vol. **5**, pp. 241–259 (1977).

109. R. G. Ballinger, R. M. Latanision, W. C. Moshier, and R. M. Pelloux, *The Effects of Heat Treatment and Environment on Corrosion Fatigue, Volume 2: Alloy 600,* EPRI TR-102436 (May 1993).

110. C. Amzallag, G. Baudry, and J. L. Bernard, *Effects of PWR Environment on the Fatigue Crack Growth of Different Stainless Steels and Inconel Type Alloy,* Proc. IAEA-Specialists Meeting on Subcritical Crack Growth, NUREG/CP–0044, Vol. 1, pp. 263–294 (1983).

111. H. Nagano, K. Tokimasa, K. Tanaka, and H. Tsuge, *Evaluation of SCC Resistance of Alloy 600 in High Temperature Pressurized Water Environments by the High Stress Ratio Cyclic Crack Growth Tests,* ISIJ Intl., **28**, p. 338 (1988).

112. G. S. Was and R. G. Ballinger, *Hydrogen Induced Cracking under Cyclic Loading of Nickel Base Alloys Used for PWR Steam Generator Tubing,* Third Semi-Annual Progress Report, NP4613, Research Project 1166-3, EPRI (Jan. 1980).

113. L. A. James and D. P. Jones, *Fatigue Crack Growth Rates for Austenitic Stainless Steel in Air,* in Predictive Capabilities in Environmentally Assisted Cracking, PVP Vol. 99, The American Society of Mechanical Engineers, New York, pp. 363–414 (1985).

114. W. H. Bamford, P. K. Liaw, and E. D. Eason, *A Review of Corrosion Fatigue Crack Growth Behavior for Pressure Vessel Steels in Light Water Environments,* in Fatigue, Degradation, and Fracture – 1990 –, W. H. Bamford, et al., eds., PVP Vol. 195, MPC Vol. 30, The American Society of Mechanical Engineers, pp. 1–12 (1990).

115. E. K. Walker, *The Effect of Stress Ratio during Crack Propagation and Fatigue for 2024–T3 and 7075–T6,* in The Effects of Environments and Complex Load History on Fatigue Life, STP 462, American Society for Testing and Materials, Philadelphia, pp. 1–14 (1970).

116. E. K. Walker, *An Effective Strain Concept for Crack Propagation and Fatigue Life with Specific Applications to Biaxial Stress Fatigue,* in Proc. Air Force Conference on Fatigue and Fracture of Aircraft Structures and Materials, H. A. Wood, et al., eds., Report AAFFDL–TR–70–144, Air Force Flight Dynamics Laboratory, pp. 25–233 (Sept. 1970).

117. J. L. Bernard and G. S. Slama, *Fatigue Crack Growth in Air Environment at 300°C for Stainless Steels,* Nucl. Technol., **59** (1), 136–147 (1982).

118. P. Rabbe and H. P. Lieurade, *Etude a l'Aide de la Mecanique de la Rupture de la Vitesse Fissuration en Fatigue d'une Gamme Etendue d'Aciers,* Memoires Scientificiques Revue Metallurgie, **69** (9), 606–621 (1972).

119. F. P. Ford, *Quantitative Prediction of Environmentally Assisted Cracking,* Corrosion, **52**, pp. 375–395 (1997).

120. F. P. Ford, D. F. Taylor, P. L. Andresen, and R. Ballinger, *Corrosion-Assisted Cracking of Stainless and Low-alloy Steels,* EPRI NP-5064, Electric Power Research Institute, Palo Alto, CA (Feb. 1987).

121. T. Shoji, *Quantitative Prediction of Environmentally Assisted Cracking Based on Crack Tip Strain Rate*, Proc. Conf. on Predictive Capabilities in Environmentally–Assisted Cracking, R. Rungta, ed., PVP Vol. 99, American Society of Mechanical Engineers, New York, pp. 127-142 (1985).

122. T. Shoji, S. Suzuki, and R. G. Ballinger, *Theoretical Prediction of SCC Growth Behavior-Threshold and Plateau Growth Rate*, Proceedings of the Seventh International Symposium on Environmental Degradation of Materials in Nuclear Power Systems—Water Reactors, NACE International, Houston (1996).

123. P. S. Maiya and W. J. Shack, *Stress Corrosion Cracking Susceptibility of AISI 316 NG and 316 Stainless Steel in an Impurity Environment*, Corrosion, **41**, pp. 630-634 (1985).

124. D. D. Macdonald and M. Urquidi-Macdonald, *An Advanced Coupled Environment Fracture Model for Prediction of Crack Growth Rate*, Parkins Symposium on Fundamental Aspects of Stress Corrosion Cracking, S. M. Bruemmer et al., eds., pp. 443-455 (1991).

125. A. Turnbull and M. Psaila-Dombrowski, *A Review of Electrochemistry of Relevance to Environmentally–Assisted Cracking in Light Water Reactors*, Corrosion Science, **33**, pp1925-1966 (1992).

126. D.D. Macdonald, P.-C. Lu, M. Urquidi-Macdonald, T.-K. Yeh, *Theoretical Estimation of Crack Growth Rates in Type 304 Stainless Steel in Boiling-Water Reactor Coolant Environments*, Corrosion, **52**, p 768-785 (Oct. 1996).

127. G.R. Engelhardt, D.D. Macdonald, M. Urquidi-Macdonald, *Development of Fast Algorithms for Estimating Stress Corrosion Crack Growth Rate*, Corrosion Science, **41**, pp. 2267-2302 (1999).

128. *BWR Vessels and Internals Project, Evaluation of Crack Growth in BWR Stainless Steel RPV Internals* (BWRVIP-14), EPRI TR–105873, Electric Power Research Institute, Palo Alto (1996).

129. T. Kawakubo, M. Hishida, K. Amano, and M. Katsuta, *Crack Growth Behavior of Type 304 Stainless Steel in Oxygenated 290°C Pure Water under Low Frequency Cyclic Loading*, Corrosion **36**, 638-647 (1980).

130. W. S. Hazelton, *Technical Report on Material Selection and Processing Guidelines for BWR Coolant Pressure Boundary Piping*, NUREG-0313, Rev. 2 (1986).

131. L. G. Ljungberg, D. Cubicciotti, and M. Trolle, *The Effect of Sulfate on Environmental Cracking in Boiling Water Reactors under Constant Load or Fatigue*, Corrosion **46**, 641–652 (1990).

132. L. G. Ljungberg, D. Cubicciotti, and M. Trolle, *Effect of Water Impurities in BWRs on Environmental Crack Growth under Realistic Load Conditions*, Proc. 4th Int. Symp. Environmental Degradation of Materials in Nuclear Power Systems—Water Reactors, National Association of Corrosion Engineers, Houston, pp. 4–59 to 4–74 (1990).

133. L. G. Ljungberg, D. Cubicciotti, and M. Trolle, *Effect of Water Impurities in BWRs on Environmental Crack Growth in Type 304 Stainless Steel*, NUREG/CP–0112 Vol. 2, ANL–90/22 Vol. 2, pp. 57–64 (Aug. 1990).

134. J. Alexander et al., *Alternative Alloys for BWR Pipe Applications*, EPRI NP–2671–LD, pp. 5–17 to 5–32, Electric Power Research Institute, Palo Alto, CA (Oct. 1982).

135. C. W. Jewett and A. E. Pickett, *The Benefit of Hydrogen Addition to the Boiling Water Reactor Environment on Stress Corrosion Crack Initiation and Growth in Type 304 Stainless Steel*, J.. Eng. Mater. Technol. **108**, 10–19 (1986).

136. P. L. Andresen, *Effects of Stress Intensity, R Value, and Environmental Impurities in 288°C Water on Crack Growth Rate in Type 304 SS CT Specimens*, Corrosion **88**, Paper No. 11, St. Louis, MO (March 1988).

137. P. L. Andresen, *IGSCC Crack Propagation Rate Measurement in BWR Environments*, SKI Report 98:27, Swedish Nuclear Power Inspectorate, Stockholm (1998).

138 W. E. Ruther, W. K. Soppet, G. Ayrault, and T. F. Kassner, "*Effect of Sulfuric Acid, Oxygen, and Hydrogen in High Temperature Water on Stress Corrosion Cracking of AISI 304 Stainless Steel*," Corrosion, **40**, pp 518–527 (1984)

139. L. A. James and D. P. Jones, *Fatigue Crack Growth Correlation for Austenitic Stainless Steels in Air*, Proc. Conf. on Predictive Capabilities in Environmentally–Assisted Cracking, R. Rungta, ed., PVP Vol. 99, American Society of Mechanical Engineers, New York, pp. 363–414 (1985).

140. J. D. Gilman, R. Rungta, P. Hinds, and H. Mindlin, *Corrosion-fatigue Crack-growth Rates in Austenitic Stainless Steels in Light Water Reactor Environments*, Int. Journal of Pressures Vessels and Piping, **31**, pp. 55-68 (1988).

141. W. E. Ruther and T. F. Kassner, in *Environmentally Assisted Cracking in Light Water Reactors, Semiannual Report*, April–September 1993, NUREG/CR–4667 Vol. 17, ANL–94/16, pp. 22–34 (June 1994).

142. P. L. Andresen, F. P. Ford, S. M. Murphy, and J. M. Perks, *State of Knowledge of Radiation Effects on Environmental Cracking in Light Water Reactor Core Materials*, Proc. of the 4th International Conference on Environmental Degradation of Materials in Nuclear Power Systems, NACE International, Houston (1990).

NRC FORM 335 (2–89) NRCM 1102, 3201, 3202

U. S. NUCLEAR REGULATORY COMMISSION

BIBLIOGRAPHIC DATA SHEET

(See instructions on the reverse)

1. REPORT NUMBER *(Assigned by NRC. Add Vol., Supp., Rev., and Addendum Numbers, if any.)*

NUREG/CR–4667, Vol. 29
ANL–00/23

2. TITLE AND SUBTITLE

Environmentally Assisted Cracking in Light Water Reactors.
Semiannual Report July 1999—December 1999

3. DATE REPORT PUBLISHED

MONTH	YEAR
November	2000

4. FIN OR GRANT NUMBER

W6610

5. AUTHOR(S)

O. K. Chopra, H. M. Chung, E. E. Gruber, W. E. Ruther,
W. J. Shack, J. L. Smith, W. K. Soppet, and R. V. Strain

6. TYPE OF REPORT

Technical; Semiannual

7. PERIOD COVERED *(Inclusive Dates)*

July 1999—December 1999

8. PERFORMING ORGANIZATION – NAME AND ADDRESS *(If NRC, provide Division, Office or Region, U.S. Nuclear Regulatory Commission, and mailing address; if contractor, provide name and mailing address.)*

Argonne National Laboratory
9700 South Cass Avenue
Argonne, IL 60439

9. SPONSORING ORGANIZATION – NAME AND ADDRESS *(If NRC, type "Same as above": if contractor, provide NRC Division, Office or Region, U.S. Nuclear Regulatory Commission, and mailing address.)*

Division of Engineering Technology
Office of Nuclear Regulatory Research
U.S. Nuclear Regulatory Commission
Washington, DC 20555–0001

10. SUPPLEMENTARY NOTES

M. B. McNeil, NRC Project Manager

11. ABSTRACT (200 words or less)

This report summarizes work performed by Argonne National Laboratory on fatigue and environmentally assisted cracking (EAC) in light water reactors (LWRs) from July 1999 to December 1999. Topics that have been investigated include (a) environmental effects on fatigue S–N behavior of primary pressure boundary materials, (b) irradiation–assisted stress corrosion cracking (IASCC) of austenitic stainless steels (SSs), (c) EAC of Alloys 600 and 690, and (d) assessment of industry crack-growth models. The fatigue strain-vs.–life data that are available on the effects of various material, loading, and environmental parameters on the fatigue lives of carbon and low–alloy steels and austenitic SSs are summarized. Effects of reactor coolant environment on the mechanism of fatigue crack initiation are discussed. Two methods for incorporating the effects of LWR coolant environments into the ASME Code fatigue evaluations are presented. Slow-strain-rate tensile tests and posttest fractographic analyses were conducted on several model SS alloys irradiated to $\approx 0.9 \times 10^{21}$ n·cm^{-2} (E > 1 MeV) in He at 289°C in the Halden reactor. The results have been used to determine the influence of alloying and impurity elements on the susceptibility of these steels to IASCC. Fracture toughness J–R curve tests were also conducted on two heats of Type 304 SS that were irradiated to ≈ 0.3 and 0.9×10^{21} n·cm^{-2} in the Halden reactor. Crack–growth–rate tests have been conducted on compact–tension specimens of Alloy 690 under cyclic loading to evaluate the enhancement of crack growth rates of these alloys in LWR environments. The existing fatigue crack growth data on Alloys 600 and 690 have been analyzed to establish the effects of temperature, load ratio, frequency, and stress intensity range ΔK on crack growth rates in air. Predictions of the PLEDGE code for environmentally assisted cracking in stainless steels have been compared with experimental data collected by the BWRVIP, developed at ANL, provided by P. L. Andresen of GE, used to develop the original USNRC disposition curve, and gathered from other sources in the literature.

12. KEY WORDS/DESCRIPTORS *(List words or phrases that will assist researchers in locating this report.)*

Corrosion Fatigue
Crack Growth
Irradiation–Assisted Stress Corrosion Cracking
Radiation–Induced Segregation
Stress Corrosion Cracking
Carbon and Low–Alloy Steels
Types 304, 304L, 316, and 316NG Stainless Steel
Alloys 600 and 690

13. AVAILABILITY STATEMENT

Unlimited

14. SECURITY CLASSIFICATION

(This Page)

Unclassified

(This Report)

Unclassified

15. NUMBER OF PAGES

16. PRICE

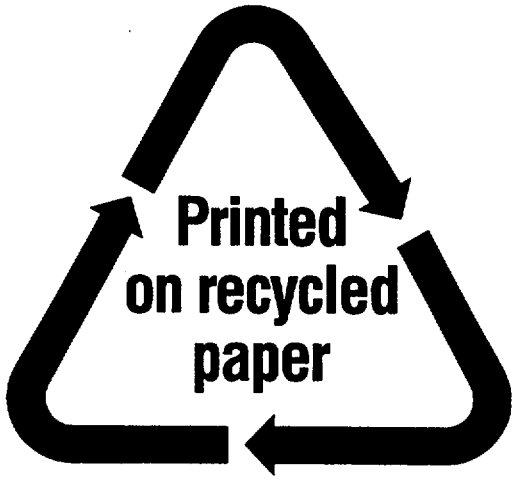

Federal Recycling Program

UNITED STATES
NUCLEAR REGULATORY COMMISSION
WASHINGTON, D.C. 20555-0001